Xiangjiang Liu

Nanoparticles and Surface-Enhanced Optical Effects for Chemical and Biological Sensing

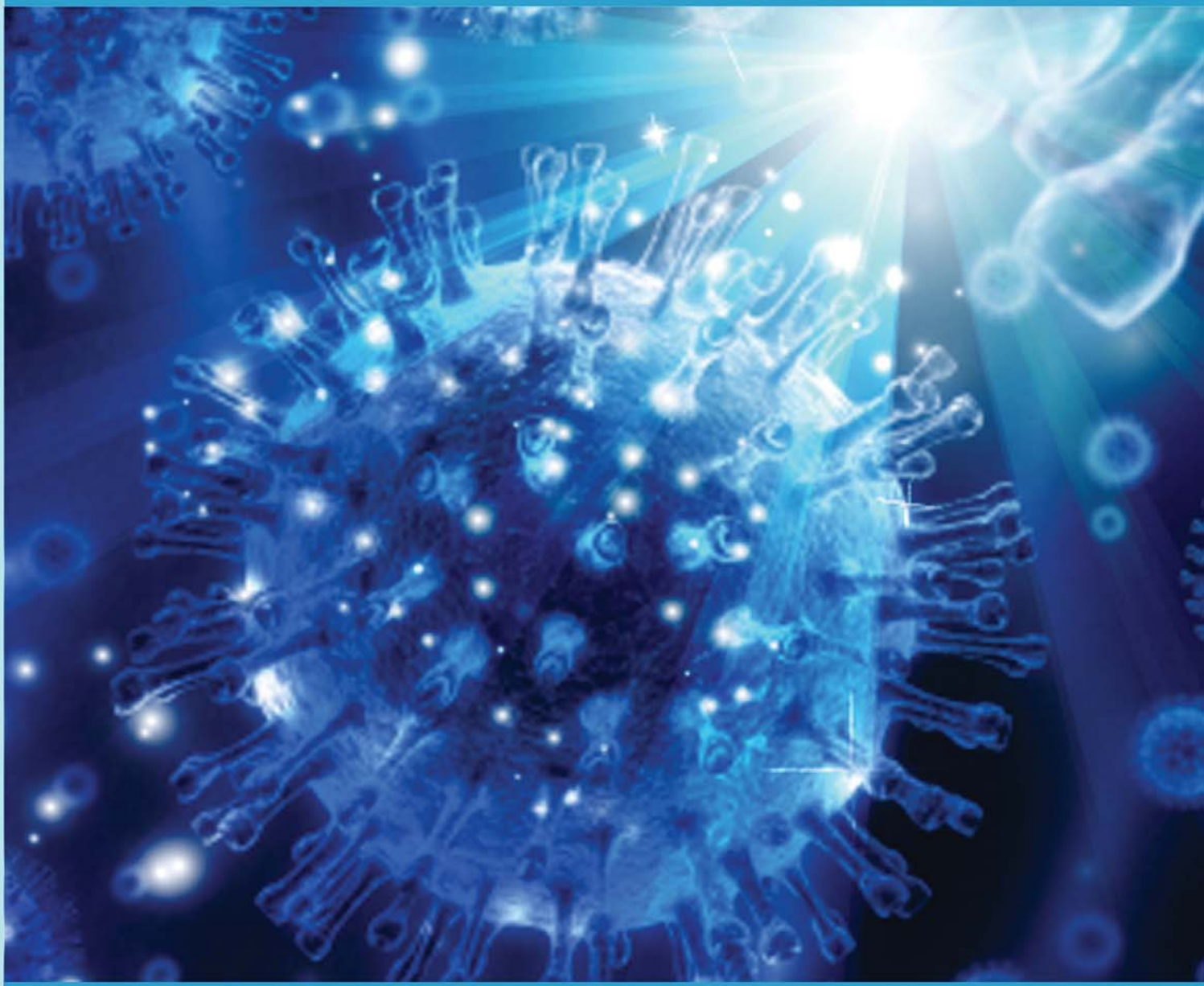

Xiangjiang Liu Nanoparticles and Surface-Enhanced Optical Effects for Chemical and Biological Sensing

TECHNISCHE UNIVERSITÄT MÜNCHEN

Institut für Wasserchemie und Chemische Balneologie
Lehrstuhl für Analytische Chemie

Nanoparticles and Surface-Enhanced Optical Effects for Chemical and Biological Sensing

Xiangjiang Liu

Vollständiger Abdruck der von der Fakultät für Chemie der Technischen Universität München zur Erlangung des akademischen Grads eines

Doktors der Naturwissenschaften (Dr. rer. nat.)

genehmigten Dissertation.

Vorsitzender: Univ.-Prof. Dr. M. Schuster

Prüfer der Dissertation:
1. Univ.-Prof. Dr. R. Nießner
2. apl. Prof. Dr. U. Bösl-von Grafenstein

Die Dissertation wurde am 23.11.2011 bei der Technischen Universität München eingereicht und durch die Fakultät für Chemie am 09.01.2012 angenommen

ACKNOWLEDEMENT

This thesis is based on research conducted between September 2008 and September 2011 at the Institut für Wasserchemie und Chemische Balneologie der Technischen Universität München. A number of persons have contributed to the completion of this thesis, and deserve to be thanked.

First and foremost I thank Prof. Dr. Reinhard Nießner for the possibility to prepare this work under his auspices. He provided many exciting new ideas to me, and helped me to find the bridge between those ideas and real-world applications by his acute foresight.

I wish to express my deepest gratitude to Prof. Dr. Christoph Haisch, who opened the door of photoacoustic technology for me and created an opportunity to carry out the research. In addition, he has given me invaluable encouragement and guidance throughout the project.

I would also like extending my sincere thanks to Dr. Martín G. González and Prof. Dr. Dietmar Knopp, who gave me a lot of enthusiastic and effective help. Also to be thanked are Sebastian Wiesemann and Christine Sternkopf for technical support and experimental help.

Equally, I thank all other colleagues in the institute for the inspiring atmosphere, countless scientific and non-scientific help. In particular, I would like to mention the following persons, Christoph Berger, Dr. Clemens Helmbrecht, Dr. Xaver Y. Z. Karsunke, Maria Knauer, Lu Pei, Johannes Schmid, Kathrin Schwarzmeier and Klaus Wutz.

I also want to thank my family, in particular my parents, for all their unconditional support and confidence throughout my scientific career. My best thanks give to Cao Jingxin for her patience and understanding with me.

Very special thanks to Prof. Ruqin Yu at Hunan University, whose great enthusiasm for science and rigorous working attitude always inspire me in my scientific research career.

PUBLICATIONS

Parts of this thesis have been published in following scientific journals:

Liu, X. J.; González G. M.; Niessner, R.; Haisch, C., Strong size-dependent photoacoustic effect on gold nanoparticles: a sensitive tool for protein detection. *Anal. Methods*, **2011**, DOI: 10.1039/c1ay05497j.

Liu, X. J.; Knauer, M.; Ivleva, P. N.; Niessner, R.; Haisch, C., Synthesis of Core−Shell Surface-Enhanced Raman Tags for Bioimaging, *Anal. Chem.*, **2010**, *82*, 441-446.

González G. M.; **Liu, X. J.**; Niessner, R.; Haisch, C., Lead ion detection in turbid media by pulsed photoacoustic spectrometry based on dissolution of gold nanoparticles, *Sensors and Actuators B: Chemical*, **2010**, 150, 770-773.

González G. M.; **Liu, X. J.**; Niessner, R.; Haisch, C., Strong size-dependent photoacoustic effect on gold nanoparticles by laser-induced nanobubbles, *Appl. Phys. Lett.* **2010**, 96, 174104.

Knauer, M.; Ivleva, P. N.; **Liu, X. J.**; Niessner, R.; Haisch, C., Surface-Enhanced Raman Scattering-Based Label-Free Microarray Readout for the Detection of Microorganisms, *Anal. Chem.*, **2010**, *82*, 2766-2772.

ABSTRACT

Gold nanoparticles (GNPs) have attracted much interest in the field of chemical and biological sensing, due to their unique size- and shape-dependent optical properties. In the first part of this thesis, a new size-dependent photoacoustic (PA) effect of GNPs is described. We found that the PA signal produced by laser-induced nanobubble on GNPs strongly depends on GNPs size. Based on this new effect, variations of size of GNPs, due to nanoparticle aggregation and dissolving, can be detected. Hence, the potential of this new PA effect in the field of chemical and biological sensing is investigated. Three possible applications are demonstrated and tested, and the results are compared with conventional diagnostic methods respect to the sensitivity and selectivity.

The second part of this thesis is mainly concerned with another optical effect of GNPs: surface-enhanced Raman scattering (SERS). SERS holds vast potential in biological and chemical sensing. In this section, we attempted to directly monitoring antigen-antibody binding by SERS. Many label-free SERS detection schemes have been demonstrated and tested. But all these attempts yielded unsatisfied results. Hence, we switched to an indirect way, which was based on labeled SERS nanoparticle probes. In the following chapter, a rapid and straightforward way for the synthesis of core-shell SERS tags is described, and then SERS tags are functionalized with anti-*Salmonella* antibody as a model to present a potential application of tags in biological sensing.

Contents

I. Theoretical Background

CHAPTER 1 Gold Nanoparticles

Contents

1.1 Historic Introduction

The past decades have witnessed tremendous advances in nanoscience and nanotechnology. Gold nanoparticles (GNPs) have emerged as an important research subject in this field. Although this development in nanoscience and nanotechnology took place recently, gold is actually one of the most ancient research themes in science. The first extraction of gold dates to the 5th millennium B.C. near the area of Varna (Bulgaria), and the first record of "soluble" gold (gold colloids) can be found in Egypt and China around the 5th or 4th century B.C [1]. The first application of this "soluble" gold was to produce ruby glass or for coloring ceramics, which are still continuing now. One of the most famous examples is the Lycurgus cup that appears green in reflected light and ruby red in transmitted light, due to the presence of gold colloids (Figure 1.1). In Middle Ages, people also discovered the medical uses of the "soluble" gold [2]. Once it was believed that the "soluble" gold could treat heart and venereal problems, dysentery, epilepsy, and tumors, and could be used for diagnosis of syphilis, although these uses have been proven to be not completely reliable later [3-5].

During the17th to 19th century, the knowledge about the "soluble" gold was gradually accumulating. In a book published in 1676 [6], a German chemist Johann Kunckel first wrote down "gold must be present in such a degree of communition that it is not visible to the human eye". This idea was generally accepted in the next century. In a French dictionary [7], as part of the explanation of the word "soluble" gold, it was written down

that "drinkable gold contained gold in its elementary form but under extreme sub-division suspended in a liquid". And the term "colloid" (from the French, *collé*) was introduced by Graham in 1861 [8].

Figure 1.1 Images of the Lycurgus Cup (courtesy of the British Museum). The glass appears green in reflected light (left) and red in transmitted light (right), due to the presence of gold colloids.

Various methods for the preparation of gold colloids have been reported and reviewed since the late 19th century [5, 9-13], including a famous work made by Faraday in 1857 [14]. Colloidal gold can be obtained by reduction of chloroaurate ($AuCl_4^-$) in aqueous solution using phosphorus in CS_2 (a two-phase system). He also investigated the optical properties of thin films consisting of dried colloidal gold and observed some reversible color changes of the films upon response to mechanical compression.

Nowadays, GNPs have been studied intensively in both fundamental and applied aspects. Their unusual optical properties, size dependent electrochemistry and high chemical stability have made GNPs an appropriate model system for investigating a wide range of phenomena, such as the behavior of the individual particle, size-related electronic, magnetic, and optical properties (quantum size effect) [15-27]. They are also present in many fascinating applied aspects like biolabeling, catalysis, DNA melting and assays etc. [28-37]. GNPs play an important role in these fields as well as in the bottom-up approach of nanotechnology, and they will become elemental materials and building block in the 21st century [1].

1.2 Synthesis Methods

Many approaches for preparing GNPs have been developed since the late 19th century [5, 9-13, 38]. In this section, some of the most important methods that are intensively used in this thesis are discussed briefly.

1.2.1 Citrate Reduction

Probably the most popular method for preparing gold nanospheres is using citrate reduction of tetrachloroauric acid ($HAuCl_4$) in water. The method was pioneered by J. Turkevich et al. in 1951 and refined by G. Frens in the 1970s [10-11]. In general, the solution of sodium citrate is added to the hot gold solution and heated for an additional thirty minutes. The reactions involved in the reduction are portrayed in Figure 1.2. The addition of sodium citrate to $HAuCl_4$ results in the oxidation of the former to sodium acetate dicarboxylate (SADC) and the reduction of the latter to AuCl. The citrate also serves as a buffer that encourages the crystal growth of the nanoparticles. This nucleation and crystallization process accelerates at high temperatures and the formation of GNPs can be noticed as a color change of the solution.

This method is very often used even now. The diameter of GNPs obtained by this method is around 10 ~ 20 nm. Larger particles (between 16 ~ 147 nm) can be produced via a modification of the ratio between the reducing/stabilizing agents (the sodium citrate to gold ratio) [11]. However, for particles larger than 30 nm prepared by this method, deviations from a spherical shape were observed, as well as a large polydispersity in diameter of GNPs. The other problem involved is the poor reproducibility of the synthesis. It is difficult to prepare large particles with the same (average) diameter obtained from two syntheses, which were carried out under identical conditions.

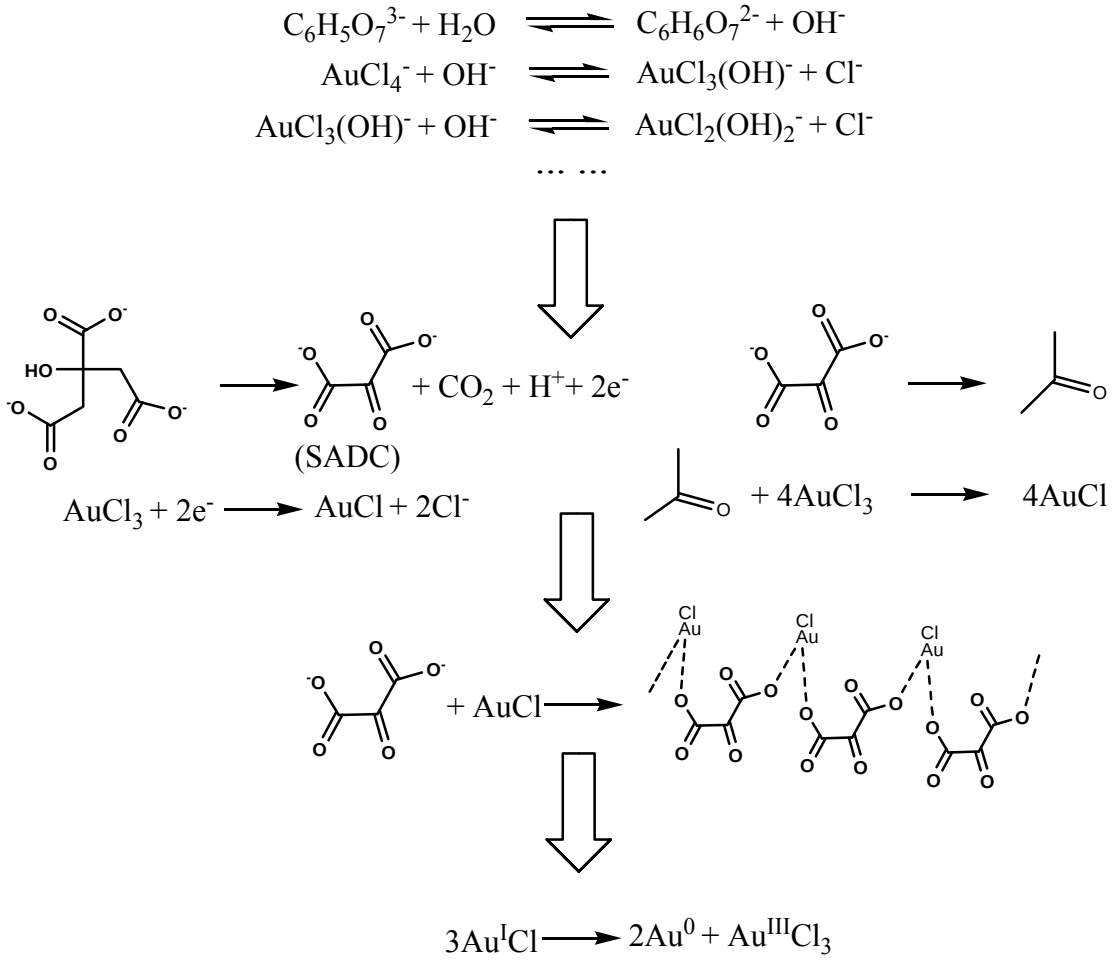

Figure 1.2 Reactions involved during the nucleation and crystal growth of gold nanoparticles.

1.2.2 Seeding Growth

Since the synthesis of large colloidal gold nanoparticles (i.e. with diameters between 40 ~ 120 nm) by citrate reduction method yields unsatisfactory results, another method, called the seeding-growth [39], has been developed and becomes extremely popular now. In a typical procedure, small gold nanoparticles (d_p < 10 nm) are first prepared as "seeds", and the seeds are grown to larger sizes by addition of a boiling solution of $HAuCl_4$ and citrate. The sizes of GNPs can be controlled by varying the ratio of seed to metal salt [40-42]. Large gold nanoparticles prepared via this approach yield more reproducible and predictable results than citrate reduction. Recent studies show that this procedure is capable of controlling the size distribution in a narrow range (10 - 15 % in the range 5 - 40 nm) [40-42].

Furthermore, a step-by-step particle enlargement is more effective than the above mentioned one-step seeding method, due to the prevention of secondary nucleation [43]. Figure 1.3 shows a step-by-step particle enlargement method [39, 44]. NH_2OH is capable of reducing Au^{3+} to bulk metal, and the reaction is dramatically accelerated by Au surfaces [45]. As a result, all the reduction of Au^{3+} takes place on the surface of colloidal gold, and no new particle nucleation is generated in suspension. Hence, all added Au^{3+} goes into enlarging the particles, and the resulting GNPs can be used as seeds again for further enlargement.

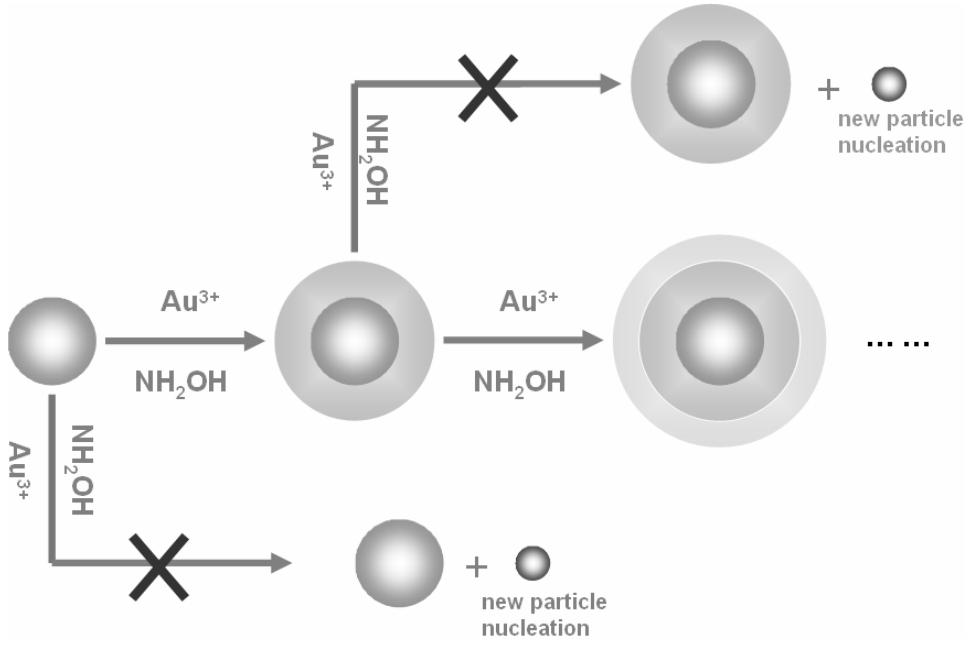

Figure 1.3 Scheme of step-by-step particle enlargement method. No new particle nucleation creates during the enlargement.

1. 3 Optical Properties of GNPs

Physicists predicted that nanoparticles would display electronic structures reflecting its electronic band structure, due to quantum-mechanical rules [46]. The resulting physical properties are neither those of bulk metal nor those of molecular compounds, but they strongly depend on the interparticle distance of the nanoparticles as well as the nature of organic ligands protecting the nanoparticles [47].

These unique size- and shape-dependent optical properties have attracted enormous interest, including large optical field enhancement resulting in the strong scattering and absorption of light [24, 28, 48-67]. These unique properties are mainly related to the collective excitation of the conduction band electrons known as the surface plasmon resonance (SPR).

1.3.1 Surface Plasmon Band

In case of noble metals, as the size is reduced to several tens of nanometers scale, a new very strong absorption emerges as the result of collective oscillation of electrons gas on the surface of nanoparticles, driven by the electromagnetic field of incoming light. This oscillation absorbs the light of a particular frequency. The deep-red color of GNPs in water reflects the broad surface plasmon band in the visible region around 520 nm. The strong absorption band is the so-called surface plasmon band (SPB).

The nature of the surface plasmon band was described in a publication by Mie in 1908 [68]. According to Mie theory, the total cross section of the SP absorption and scattering is the result of the cooperative effect of all electric and magnetic oscillations. The surface plasmon resonances of spherical particles were described quantitatively by solving Maxwell's equations with the appropriate boundary conditions [1]. Mie theory attributes this plasmon band to the dipole oscillations of the free electrons in the conduction band occupying the energy states immediately above the Fermi energy level [69]. Many optical behaviors of GNPs reported recently show a good accordance with the prediction of Mie theory [69-75].

A main influence of SPB is the size and shape of GNPs. The SPB is absent for GNPs less than 2 nm, as well as bulk gold. The size of GNPs also affects the absorption maximum and the bandwidth of SPB. For GNPs with average diameters of 9, 15, 22, 48, and 99 nm in aqueous phase, the maximum absorption of SPB was observed at 517, 520, 521, 533, and 575 nm, respectively [1]. Another proof also can be seen in Figure 1.4 that gold nanoparticles of different sizes yield different colors. Furthermore, the SPB

bandwidth increase with increasing size in the extrinsic region (larger than 25 nm), and decreasing with increasing size in the intrinsic size region (smaller than 25 nm) [1]. Besides, the absorption maximum and bandwidth of SPB are also influenced by the particle shape. A corresponding proof can be found in Figure 1.5, gold nanorods with different aspect ratios show significant difference in SPB.

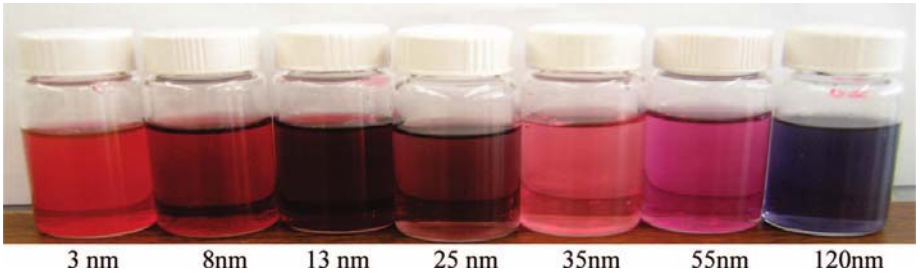

Figure 1.4 Photograph showing gold nanoparticles of different sizes. Reprinted from ref. [76].

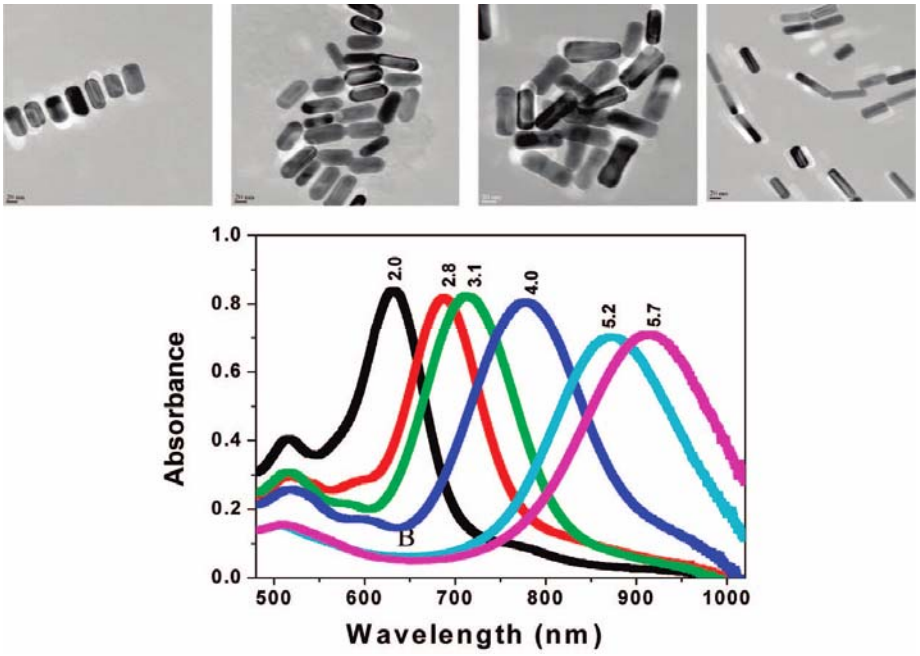

Figure 1.5 (A)TEM image of gold nanorods of average aspect ratios (σ) ≈ 2.0, 2.8, 4.0, and 5.2. (B) Extinction profile of Au nanorods with aspect ratios varying from 2.0 to 5.7. Reprinted from ref. [77].

The inter-particle distance is another major influence of SRB. For instance, the SPB is shifted to higher wavelengths with decreasing distance between elliptical particles [1]. Furthermore, as predicted by Mie theory [78-84], the change of refractive index of the solvent induces a shift of the SPB. For example, as the solvent refractive index shifts from 1.33 to 1.55, SPB of GNPs with average diameter 5.2 nm reveals 8-nm shift. Because all GNPs need to be stabilized by ligands or polymer, these stabilizers often alter the refractive index and thus cause a shift of SPB. Another parameter is the core charge. Excess electronic charge causes shifts to higher energy, whereas electron deficiency causes shifts to lower energy [78-84].

Because the position and shape of SPB are sensitive to many parameters, applications of the SPB in the fields of chemical and biological sensing are widely known [85]. These contents will be discussed at the end of this chapter.

1.3.2 Surface-Enhanced Effect

A giant enhancement of the optical responses is created on metallic nanostructure, such as metal nanoparticles and rough thin films consisting of nanoparticles. This enhancement is associated with the generation of strong electromagnetic fields at the surfaces of the nanostructures. Compared to a flat metal surface, the fundamental electric field at the nanostructures is $10^3 \sim 10^6$ times stronger [86-91]. Hence, many weak optical effects are significantly enhanced in the strong electromagnetic fields [18, 52, 59-60, 64-65, 67, 85-87].

1.3.2.1 Surface-enhanced Raman Scattering

One of these weak optical effects is the Raman scattering. Raman scattering is the inelastic scattering of light, which was first experimentally observed by Raman and Krishnan in 1923 [92]. As reported in their paper, Raman scattering was characterized as “feeble” effect, for example, the cross sections of Raman scattering are typically 14 orders of magnitude smaller than those of fluorescence. Thus, the Raman signal is several orders of magnitude weaker than the fluorescence emission in most cases [93].

However, the magnitude of the Raman scattering signal can be greatly enhanced when the analyte is placed on or near a roughened noble-metal substrate. This effect was first observed by Fleischman et al. in 1974 [94], and then discovered by Jeanmarie and Van Duyne [95], and Albrecht and Creighton in 1977 [96]. Later, large enhancements ($10^6 \sim 10^{12}$) were also observed from organic dyes on colloidal dispersion [89, 97-101]. Strong electromagnetic fields generated on surfaces of substrates or nanoparticles is closely related to this enhancing scattering effect. Hence, this enhancement effect is named surface-enhanced Raman scattering (SERS), in order to emphasize the key role of the noble metal surface in this phenomenon [93].

The exact mechanism of SERS enhancement remains unclear. It is generally accepted that two mechanisms cooperating with each other are responsible for the large enhancement of SERS: chemical enhancement and electromagnetic enhancement.

In a chemical mechanism, a charge-transfer state is created between the metal and analyte [102]. This state provides a pathway for resonant excitation and increases the probability of a Raman transition. It is believed that this mechanism contributes an average enhancement factor of 10^2. It should be noted here, that the molecule must be directly adsorbed to the roughened surface to experience the chemical enhancement.

In electromagnetic enhancement, the large enhancement of SERS is the consequence of the large electromagnetic field generated on the surface of metallic nanostructure. The size and shape of nanoparticles or the geometrical structure of the metal film plays an important role in this mechanism, since these characteristics determine the resonance frequency of the conduction electrons in the nanostructure [95]. When incident electromagnetic radiation with the same frequency excites the nanostructure, the incoming electric field drives the conducting electrons into collective oscillation. As a result, the nanostructure selectively absorbs and scatters of the resonant electromagnetic radiation, and a large electromagnetic field at the surface of the nanostructure is generated. The electromagnetic enhancement contributes an enhancement factor of over 10^6 [103].

It should be mentioned here, that enhancement effects from both mechanisms are highly localized and decayed rapidly with increasing distance between the analyte and the nanostructure surface. As mentioned above, once the analyte is separated from the surface, the chemical enhancement effect disappears. On the other hand, the analyte should be confined within the large electromagnetic fields on the surface to experience the electromagnetic enhancement [104]. But these electromagnetic fields decay dramatically with increase of distance to the surface. Van Duyne et al. have proved that the SERS intensity decreases by a factor of 10 when the distance increases to 2.8 nm [105-106]. Further studies also showed, when the distance increase to 20 nm, the SERS intensity dropped to one hundredth of the initial intensity [107]. With further increase of the distance, the intensity exhibited a linear drop on a double log scale. This feature makes SERS a truly surface-sensitive technique [104].

1.3.2.2 Nonlinear Optics

Nonlinear Optics (NLO) studies the interaction of applied electromagnetic fields and corresponding new electromagnetic fields generated in various materials, which altered in frequency, phase, or other physical properties [47]. Hence，the surface enhanced effect on metallic nanostructure is particularly important for many NLO processes, since the generally weak NLO effects can be significantly enhanced via the strong electromagnetic fields at the metallic surface [59-60, 85-87]. Several publications demonstrated that Second-Harmonic Generation (SHG) can be greatly enhanced (~10^4) for molecules absorbed on roughened metal surfaces [89, 97-101].

Recently, many publications have demonstrated the applications of the size and shape dependent NLO properties of nanomaterials in biological and chemical sensing [76-77, 91, 108-115]. NLO based sensing has exhibited some specific advantages, compared to other conventional and nanomaterial based techniques [47].

1.4 Nanoparticles in Chemical and Biological Monitoring

Intense research has been fueled into the field of molecular diagnostics by the need for practical, robust, and highly sensitive and selective detection agents that can address the deficiencies of conventional technologies [28]. In the last decade, the field has witnessed a new trend using of nanomaterials in assays for ions, DNA/RNA, protein, bacteria and biologically relevant small molecules [28, 48-54, 57, 116]. In certain cases, nanomaterials have exhibited significant advantages over conventional diagnostic systems with regard to assay sensitivity, selectivity, or are practicability. Some of them are capable of sensing at the single-molecule level in living cells, or are able to be used for the parallel detection of multiple signals, or enabling a diversity of simultaneous detections [28, 48-54, 57, 116].

Not all the nanomaterials suit for molecular diagnostics. Only certain nanomaterials are attractive due to their small size (1 - 100 nm), correspondingly large surface-to-volume ratio, chemically tailorable properties, unusual target binding properties, or overall structural robustness [28]. Since gold nanoparticles occasionally satisfy the above four requirements, and due to their low toxicity, scientists have shown great interest in using gold nanosystems for molecular diagnostics [28, 48-54, 57, 116]. Due to the surface plasmon band, gold nanoparticles also provide outstanding optical properties that can be used with a variety of techniques for labeling, imaging, sensing, and diagnostics. A lot of optical techniques can be applied in the gold nanosystem, such as SPB, SERS, NLO, or nanoparticle based fluorescence energy transfer (NSET). We will focus on some of the techniques that are closely related to this thesis.

1.4.1 Aggregation-based Colorimetric Detection

The SPB is a widely used sensing tool in the field of chemical and biological sensing. A common sensing mechanism is based on the aggregation of receptor-conjugated GNPs in the presence of the target molecule. When GNPs begin to aggregate, they form pairs of nanoparticles and the interaction of dipoles of two adjacent nanoparticles, causing a

red-shift of SPB. Thus a new peak emerges in their SPB spectrum. In a fully aggregated suspension, the red-shifted peak dominates the spectrum, which can be easily observed by naked eyes or a UV/Vis spectrometer. Based on the above mechanism, a simple homogeneous colorimetric immunoassay was firstly developed by Leuvering et al. [117]. Antibody-conjugated GNPs form aggregates after mixing with the antigen. Later, this mechanism was adopted by Mirkin et al. for DNA detection (Figure 1.6) [118-121]. Other applications included detection of protein-ligand interactions [122-123], immunological recognitions [124-125], and metal ion-ligand complexation [126-129].

The main problem of these aggregation-based colorimetric methods is their limited sensitivity. A UV/Vis spectrometer can detect aggregation only if the aggregation level is high enough to cause a color change. In order to enhance the sensitivity, many signal amplification strategies have been proposed [130]. However, these improvements often involve complicated multi-step procedures that are not only time consuming, but also significantly restricted in the reproducibility of the results.

Besides SPB, light scattering is another optical property of GNPs that attract great interest in biomolecular detection [114, 124, 131-136]. The light-scattering cross section of a GNP with a diameter of 60 nm is 200 - 300 times stronger than that of a polystyrene bead of the same size, and 4 - 5 orders of magnitude stronger than that of a strong fluorescent dye, e.g., fluorescein [131-132]. Recently, a technique called Dynamic Light Scattering (DLS) has been introduced for monitoring GNPs aggregation [137-139]. DLS is a technique used to determine the size distribution of small particles in suspension or polymers in solution [140]. Hence, the aggregation of receptor-conjugated GNPs in the presence of the target molecule was measured by DLS, and the subsequent increase of particle size was correlated to the target concentration. DLS has achieved a much higher sensitivity than UV/Vis absorbance spectrometers [137-138].

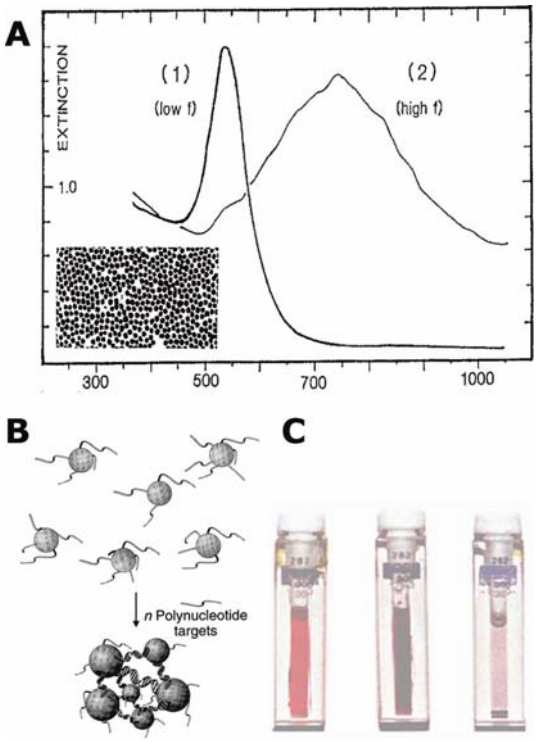

Figure 1.6 (A) Optical spectra of (1) a sparse GNPs film and (2) a dense Au nanoparticle film (inset shows TEM image of the film). (B) Schematic representation of oligonucleotide aggregates following hybridization with oligonucleotide molecules. (C) Suspensions of (left) a dispersed colloid, (middle) a linked colloid, and (right) linked, fully aggregated nanoparticles [120]. Reprinted from refs. [119, 121].

Furthermore, based on NLO properties of GNPs, a new tool called Hyper-Rayleigh scattering (HRS) was also applied in the assay. HRS technique was used to determine the first hyperpolarizabilities of chromophores [110, 113-114, 141]. It has been confirmed that the first hyperpolarizability of GNPs is much higher than that of the best available molecular chromophores, and it is highly sensitive to colloid aggregation [97], which indicates that HRS is an effective tool for aggregation detection. Aggregation of GNPs leads to tremendous enhancement of HRS intensity. Several works have demonstrated that the HRS technique is 1 - 2 orders of magnitude more sensitive than the usual the colorimetric assay based on UV/Vis absorption [76-77, 91, 108-115].

Based on the above discussion, we noticed that the improvement of the sensitivity of this aggregation-based assay is accompanied with the adoption of a more sensitive aggregation detection tool. This thesis is inspired by this observation.

1.4.2 SERS-based Sensing

Despite a rough understanding of the enhancing mechanism, SERS has been fully investigated its potentials in molecule sensing. The interests of SERS-based sensing are mainly devoted into two aspects [142]. The first is the so-called single-molecule detection. Based on the enormous enhancements (10^{12}) in hot spots, a level of single-molecule detection can be achieved. The other interest is the creation of an ultrasensitive SERS-based sensing platform for molecular identification, especially as a sensor for chemical and biological molecules.

The SERS sensing mechanisms can be generally divided into two types: either directly detecting the fingerprint spectra of a target molecule, or indirectly detecting it by a molecular label [93]. Both approaches offer the possibility for multicomponent or multiplexed detection of low-concentration analytes. In the direct way, target molecules are detected directly via SERS. One example of this type is a glucose sensor, proposed by Van Duyne and co-workers [143]. A hydrophilic partition layer was modified on the SERS substrate (roughened silver surface), in order to facilitate the preconcentration of glucose within the region of enhanced electromagnetic field of the substrate (Figure 1.7). Glucose was detected and quantified based on its SERS signal. Similar approach was also applied to detect other analytes [144] [65, 145-146]. In these approaches, no labeling procedure was involved. Therefore, the direct SERS detection is also mentioned as label-free SERS detection.

Instead of direct way, the target can also be indirectly detected based on the signal of a SERS label. In this approach, SERS-active molecules bound to the target molecules have been prepared and utilized. For instance, Mirkin et al. used ssDNA conjugated GNPs as SERS label to detect target DNA [147], as shown in Figure 1.8. SERS signal of the label revealed the identity of the target ssDNA, and is used as the basis for quantification. Other analytes were also be detected via similar approaches [148]. But this type of SERS label is comparably not stable, due to the direct exposure of the label surface to the outside environment. An improved method is to cover the particle surface

by a layer of silica or polymer, after the preparation of the label (so-called core-shell SERS tags) [149-151]. This content we will discuss in CHAPTER 9 in detail.

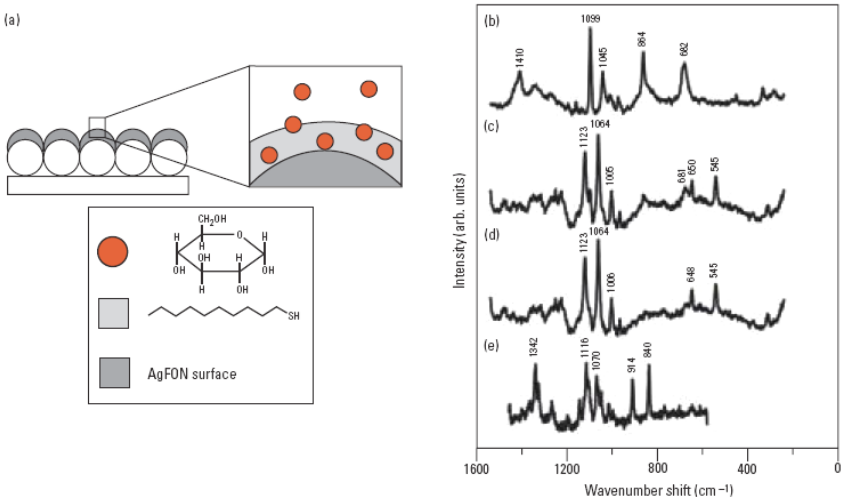

Figure 1.7 Prototype of an implantable glucose sensor. (a) Schematic illustration the use of a partition layer for detecting glucose. SERS spectra of (b) a 1-decanethiol monolayer on a silver film over a nanosphere substrate. Reprinted from refs. [143].

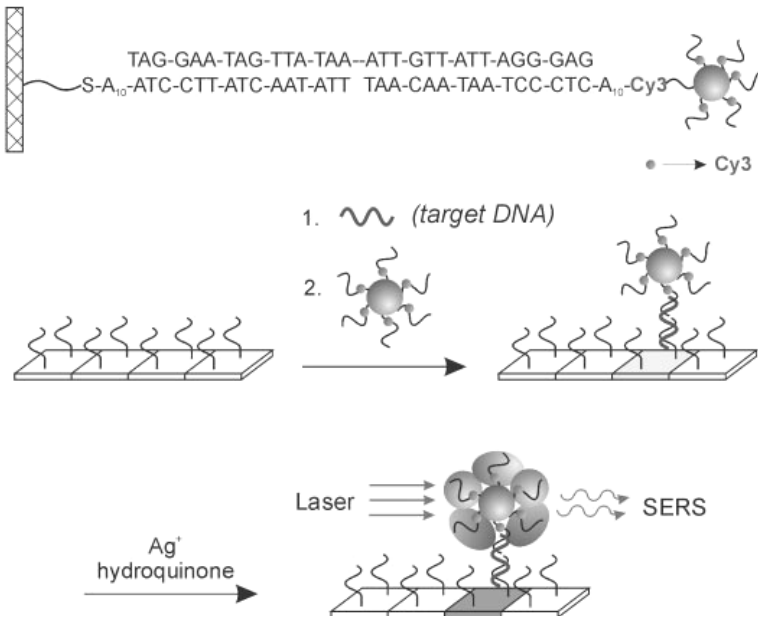

Figure 1.8 Multiplexed detection of oligonucleotide targets based on SERS labels. After the substrate has been exposed to target DNA, it was treated with the SERS label and silver enhancement solution for SERS readout. Reprinted from refs. [147].

CHAPTER 2

The Photoacoustic Effect

Contents

2.1 Historic Introduction of the PA Effect

The Photoacoustic (PA) effect consists of the generation of acoustic signals by the absorption of electromagnetic energy (particularly of light) in matter. When the matter is excited by pulsed or modulated light, the energy absorbed by the matter causes a local heating and expansion, thus a detectable acoustic signal is produced in the surrounding medium. In the view of energy transformation, the PA effect is the transformation of absorbed light energy into thermal energy of the matter.

The discovery of the PA effect dates back to 1880 in Alexander Graham Bell's search for a means of wireless communication [152]. He succeeded in transmitting sound with a device he called "photophone" (Figure 2.1). The sound signal was carried by a beam of sunlight that was reflected by a vocally modulated mirror. The signal could be recovered by an ordinary telephone receiver equipped with a selenium cell illuminated by the sunlight beam.

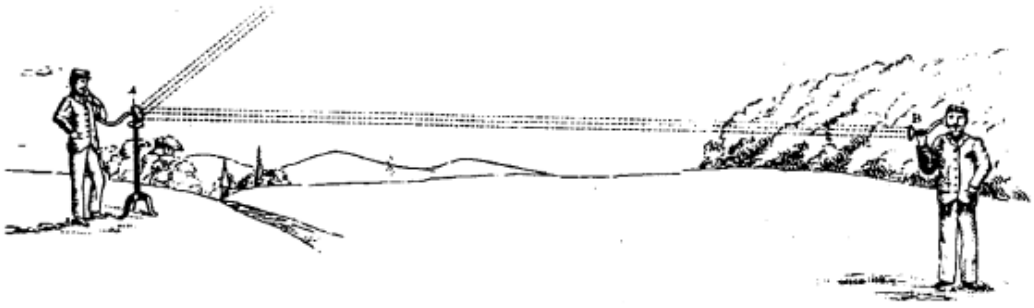

Figure 2.1 The photophone (from Lüscher 1984, reproduced from Bell, 1880).

While working with the photophone, Bell also observed that solid samples could emit sound when exposed to a rapidly-interrupted sunlight beam by a rotating slotted disk, and the resulting sound signal was related to the composition of the sample. Hence, he developed a device called "spectrophone" [153], which worked essentially same as an ordinary spectroscope. Instead of an eyepiece, the spectrophone was equipped with a hearing tube as the detector. Therefore, samples could be analyzed by the corresponding sound signal when excited by the light source. As mentioned by Bell, "the ear cannot of course compete with the eye for accuracy" when examining the visible spectrum [153]. But the "spectrophone" offers an advantage in the capability of measuring spectra in the invisible range that were previously undetectable. Using the "spectrophone", Bell discovered that samples exposed to rapidly-interrupted invisible light (ultraviolet, infrared) could also produce sound.

Further experiments from John Tyndall and Wilhelm Roentgen proved that liquids and gases shared the same effect with solid phase samples [154-155]. Tyndall also made a discovery that the amplitude of the resulting sound signal was directly proportional to the intensity of the incident light. Yet these initial discoveries were semi-quantitative due to the fact that accurate means for measuring sound intensity did not exist at that moment. This limitation as well as lack of intense light sources brought the development of PA effect to a standstill for over half century.

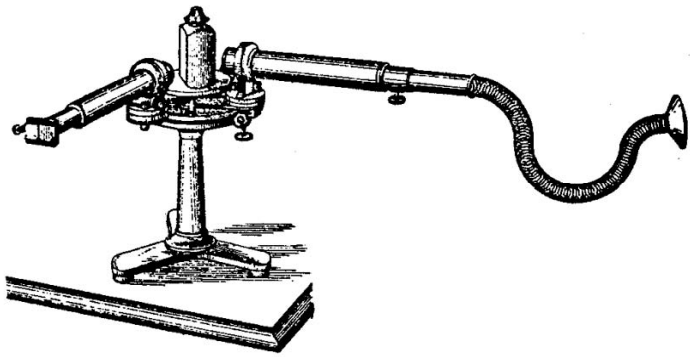

Figure 2.2 The spectrophone (From Lüscher 1984, reproduced from Bell, 1880).

The Important step leading to the renaissance of the PA effect for analytical purposes was the invention of the laser in 1960. Lasers provide high intensity light sources that greatly enhance the sound amplitude and sensitivity of PA spectroscopy (PAS). Furthermore, the renaissance gained great momentum in the development of highly sensitive sound detectors, such as condenser microphones and piezoelectric transducers. In all PA experiments with modulated excitation, microphones replaced the hearing tubes in Bell's first experiments to detect acoustic signals in the audible range [156-159]. On the other hand, ultrasound in the range up to 100 MHz can be detected by piezoelectric transducers [160]. A recent development in this field is the use of optical interferometer as alternative PA signal detector [161-162].

Owing to these developments, Rosencwaig and Gersho published the first comprehensive theoretical description of the PA effect in solids after its discovery: the so-called RG theory [156-159]. Since then, PAS has crossed the boundary to become an analytical tool in the strict sense, which has been used to investigate a variety of chemical and physical phenomena.

Although the first practical application of the PA effect occurred in gas analysis [163], liquids and solids were soon investigated by PAS [164-166]. PAS is also a non-destructive detection tool, which fulfils the requirements of material science. Thus, PAS has been used to characterize thin films, semiconductors, ceramics and magnetic materials [167-169]. In the medical field, PAS was used to examine tissue [170-171], and for depth-resolved and tomographic measurements [172-179]. In environmental analysis, PAS was used for quantification of pesticides, pollutants, aerosols and heavy metal ions [180-188]. In addition, PAS also plays a role in the field of quality control [189-190].

2.2 The Mechanisms of PA Generation in Liquid

Since this thesis is devoted to liquid systems, we will focus on discussing the PA theory in the liquid phase. As shown in Figure 2.3, many mechanisms are capable of generating acoustic signals in liquids, which can be generally divided into three categories: optical absorption followed by thermal de-excitation (thermal expansion and liquid boiling), optical absorption by non-thermal de-excitation (photochemical processes and breakdown), and by non-absorption excitation (electrostriction and radiation pressure).

In terms of liquid analysis, thermal expansion is of particular importance. Firstly, compared to boiling, dielectric breakdown and the photochemical process, the risk of damaging the sample in the thermal expansion is comparably small. Compared to radiation pressure and electrostriction, thermal expansion can generate larger PA signals. In most cases, the thermal expansion process exhibits a straightforward relationship between the signal amplitude and the optical absorption, which offers a great advantage in the signal processing. In this section, we will discuss this mechanism in detail.

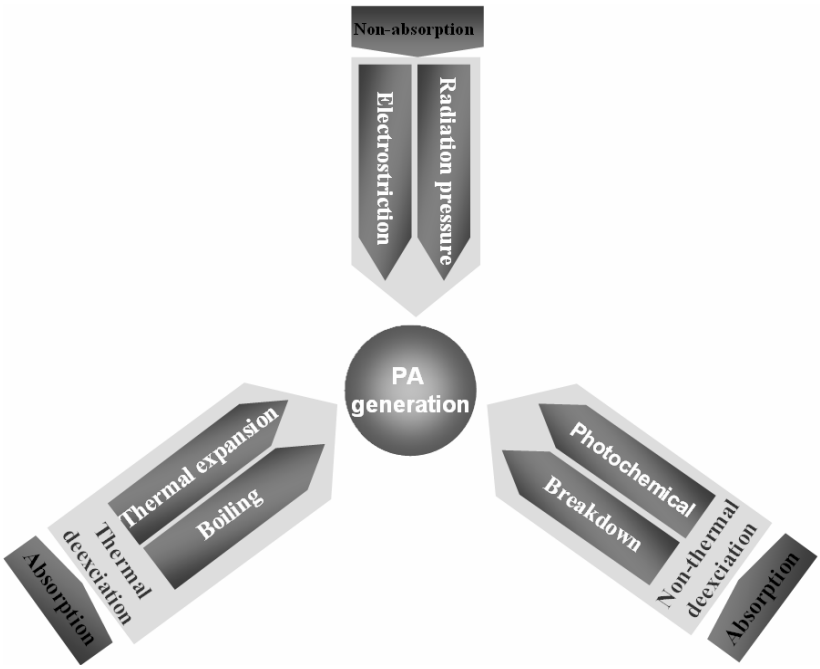

Figure 2.3 Mechanisms for generation of acoustic signal in liquid: boiling [191-194], breakdown [195-196], photochemical process [197], electrostriction [198-199] , radiation pressure and thermal expansion.

2.2.1 Thermal Expansion

Actually, all modulated or pulsed energy beams are capable of generating an acoustic signal, such as electromagnetic radiation, X-rays, electrons, protons, ions and other particles. The most common way of PA generation is using pulsed or modulated light. It is widely applied in material characterization and medical diagnosis.

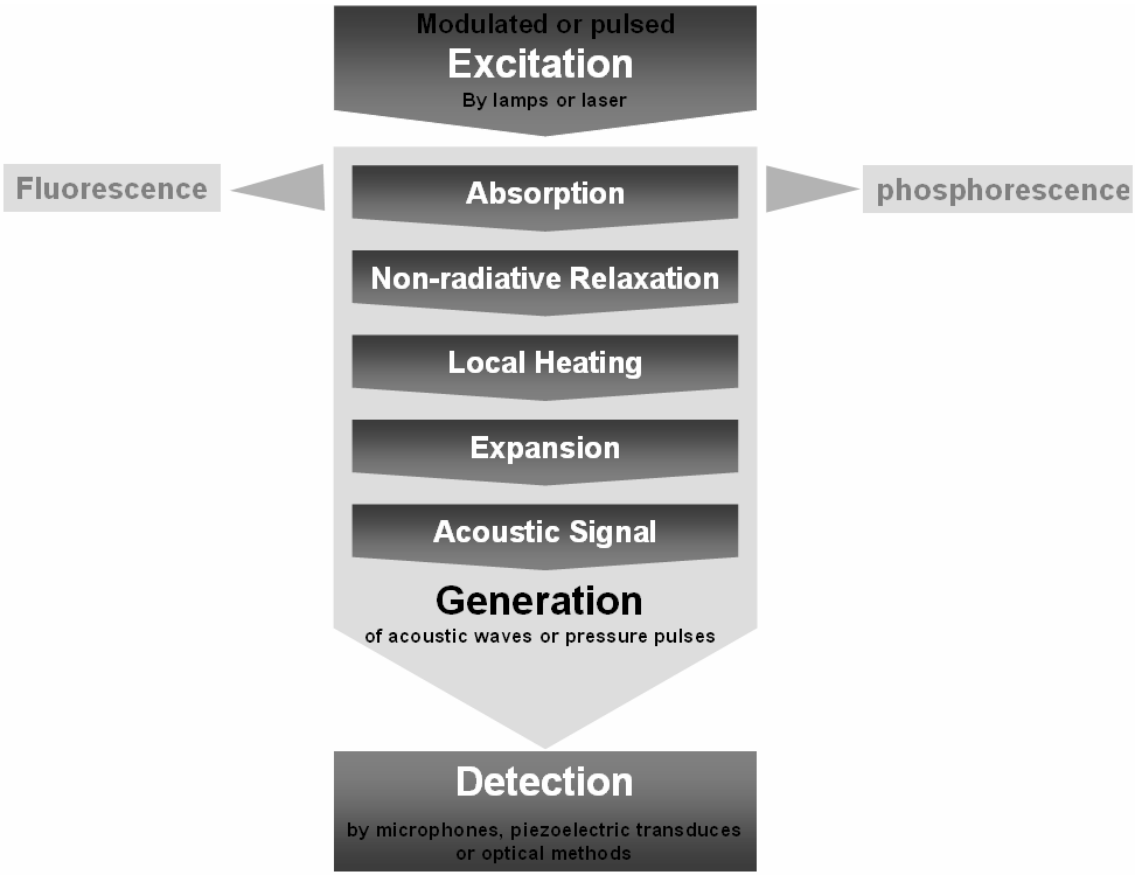

Figure 2.4 Fundamental processes of PA generation.

The processes involved in the PA generation are described in Figure 2.4. The light energy absorbed by the sample excites some electrons of the molecules in the illuminated volume to higher energy levels. These excited electrons will subsequently relax to lower levels through a combination of radiation (fluorescence, phosphorescence) and non-radiation pathways. Ultimately, the non-radiation relaxation will generate heat and thermal expansion in the illuminated region. As a result, an acoustic signal is generated and propagated away from the illuminated region, which can be detected with a suitable sensor.

It should be noted here, PA detection is specific to the non-radiation relaxation. In other words, the radiant relaxation, fluorescence and phosphorescence etc., will not generate the PA signals, since in these processes no heat is produced inside the sample. Thus, PA spectroscopy can be used as a complement of fluorescence spectroscopy.

2.3 Qualitative PA Theory in Liquid

Based on the thermodynamic principles, the relationship between the resulting PA amplitude and other parameters can be deduced. Although the deduction is semi-quantifitative, the results are in good agreement with the experimental results.

The absorption of light in a medium can be described by Lambert Beer's Law [200-201]:

$$A = \log(\frac{I_0}{I}) = \varepsilon cd \tag{2.1}$$

I_0 is the intensity of the excitation beam, I is the intensity after transmitting through a sample of thickness d, and ε is the extinction coefficient and c is the concentration of the absorbing substance. The common logarithm of I_0/I is called absorbance or extinction A. But in the field of PA spectroscopy, it is more common to use the absorption coefficient μ_a (natural logarithm of I_0/I) to describe the absorption [200-201]:

$$\mu_a = ln10\frac{1}{d}A \approx 2.3\frac{1}{d}A \tag{2.2}$$

The optical penetration depth δ is defined as the reciprocal of the absorption coefficient [200-201]:

$$\delta = \frac{1}{\mu_a} \tag{2.3}$$

The energy E_t transmitted through the sample can be characterized by the optical absorption coefficient μ_a and the path length d, which is given by,

$$E_t = E_0 e^{-\mu_a d} \tag{2.4}$$

E_0 denotes the laser pulse energy of the incident light beam. Because of the energy balance $E_0 = E_t + E_a$, the energy E_a absorbed inside the sample can be obtained through

[166]:

$$E_a = E_0(1-e^{-\mu_a d}) \tag{2.5}$$

Normally, the non-radiation relaxation processes dominate radiation relaxation. Hence, the fluorescence and phosphorescence can be neglected in most cases. Therefore, we can assume all of the absorbed energy E_a is converted into thermal energy E_{th} to heat the liquid [166]:

$$E_a = E_{th} \tag{2.6}$$

The resulting temperature rise ΔT in the illuminated region can be described as [166]:

$$\Delta T = \frac{E_{th}}{C_p \rho V} = \frac{E_a}{C_p \rho V} \tag{2.7}$$

where V is the illuminated volume, C_P and ρ are the heat capacity and density of the liquid, respectively. The resulting volume expansion ΔV can be calculated from following equation [190],

$$\Delta V = V_0 \beta \Delta T \tag{2.8}$$

Here, β is the thermal expansion coefficient, V_0 is the originally illuminated volume, which can be calculated from the irradiated surface area F_s and sample thickness d (if the optical penetration depth $\delta < d$, the illuminated volume $V_0 = \pi R b^2 \delta$)

$$V_0 = F_s d = \pi R_b^{\,2} d \tag{2.9}$$

If the laser pulse is short enough, the heat exchange from the illuminated volume to the outside can be neglected during the laser pulse duration. The volume expansion ΔV eventually leads to the formation of a pressure wave that propagates with the speed c_0. The sound pressure Δp can be described by [202],

$$\Delta p = c_0^{\,2} \rho \Delta T \tag{2.10}$$

Replacing ΔT by eq. 2.7 and V_0 by eq. 2.9,

$$\Delta p = \frac{1}{F_s d} \frac{\beta c_0^{\,2}}{C_p} E_0(1-e^{-\mu_a d}) \tag{2.11}$$

For $\mu_a d << 1$, eq. 2.5 can be approximated by a Taylor series, and the quadratic and the higher terms can be neglected. In this case, E_a can be described by a linear function [166]:

$$E_a = E_0 \mu_a d \tag{2.12}$$

Accordingly, eq. 2.11 can be simplified to,

$$\Delta p = \frac{1}{F_s} \frac{\beta c_0^{\,2}}{C_p} E_0 \mu_a \tag{2.13}$$

Using the same setup for detection, F_s can be regarded as a constant. Hence, the expression can be simplified to [164-166].

$$\Delta p \propto \frac{\beta c_0^{\,2}}{C_p} E_0 \mu_a \tag{2.14}$$

The amplitude of the resulting PA wave depends on the absorption coefficient μ_a, the thermal expansion coefficient β, the heat capacity C_p of the sample, the sound speed c_0 in the sample, and the excited energy E_0. Hence, for quantitative analysis of the absorption coefficient μ_a, the other factors must remain constant during the measurement.

2.4 Frequency and Shapes of the Acoustic Waves

Knowing the shape and the frequency of acoustic wave facilitates the design of the acoustic detector and effective reception of the acoustic signal.

2.4.1 Frequency

Acoustic signals consist of a wide frequency range, which can generally be divided into four categories according to the human auditory system [203], as shown in Table 2.1.

Table 2.1 Classification of sound wave.

	Infrasound	**Audible sound**	**Ultrasound**	**Hypersonic**
Frequency	< 20 Hz	20 Hz - 20 KHz	2 KHz - 1 GHz	> 1 GHz

2.4.2 Shapes

In this section, we will discuss PA sources with a regular geometrical shape, such as cylindrical, plate and spherical models. The absorption coefficient μ_a of the liquid, the penetration depth δ, the beam diameter D, and the sample thickness d are important in this process. In Table 2.2, the conditions to produce them are summarized.

Plane wave: if the absorption coefficient μ_a of a liquid is large enough that the optical penetration depth δ becomes much smaller than the beam diameter D and the sample thickness d, a plane acoustic wave will form, as shown in Figure 2.5 (left).

Cylindrical wave*:* when absorption coefficient μ_a is small enough that the penetration depth δ becomes much larger than the beam diameter D and the sample thickness d, the PA source can be regarded as cylindrical in shape, as shown in Figure 2.5 (middle).

Spherical wave: if the absorption coefficient μ_a is large enough and the optical penetration depth δ is near to the beam diameter D, the shape of the resulting acoustic wave will be hemispherical, as shown in Figure 2.5 (right).

Table 2.2 Shapes of acoustic waves *vs.* Laser parameters (absorption coefficient of the liquid μ_a, penetration depth δ, beam diameter D, and sample thickness d).

Shape of the wave	Plane	Cylindrical	Spherical
	$\mu_a \approx \infty$	$\mu_a \approx 0$	$\mu_a \approx \infty$
	$\delta \approx 0$	$\delta = \infty$	$\delta \approx 0$
	$\delta << D$	$\delta >> D$	$\delta \approx D$
	$\delta << d$	$\delta >> d$	$D \approx 0$

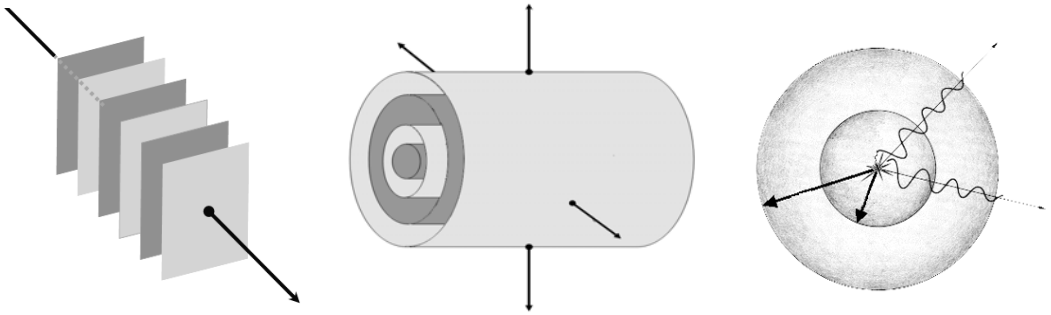

Figure 2.5 Shapes of the acoustic waves: plane wave (left), cylindrical wave (middle), spherical wave (right).

2.5 Propagation of Acoustic Waves

The interaction of acoustic wave with matter is of great importance both in the detection and the interpretation of the PA signals. Hence, some important characteristics of acoustic waves and their possible interactions with matter are summarized in this section.

The acoustic wave is a mechanical wave that is an oscillation of pressure propagating through the medium. The propagation speed is given by the sound speed $c_{0,}$ which depends on the property of the medium it is passing through. It is also influenced by temperature. The sound pressure p is the local pressure deviation from the equilibrium pressure caused by the acoustic wave. The SI unit for sound pressure p is Pascal (Pa). The sound intensity I is the average rate of sound energy transmitted through a unit area (normalized to the propagation direction), which can be described by [204],

$$I = \frac{1}{2} c_0 \kappa p^2 \tag{2.15}$$

where k is the compressibility of the medium.

Sound pressure level L_p is a logarithmic function of the effective sound pressure relative to a reference value. It is measured in decibels (dB) above a standard reference level [204]:

$$L_p = 10 \lg \frac{p_{rms}^{\ 2}}{p_{ref}^{\ 2}} \tag{2.16}$$

where p_{rms} is the sound pressure being measured and p_{ref} is the reference sound pressure.

An important material-dependent parameter is the characteristic acoustic impedance or the impedance Z. The acoustic impedance is defined as the ratio of sound pressure p to particle velocity v in the respective medium, or from sound speed c_0 and density ρ of the medium[203-204]:

$$Z = \frac{p}{v} = c_0 \rho \tag{2.17}$$

2.5.1 Reflection and Transmission

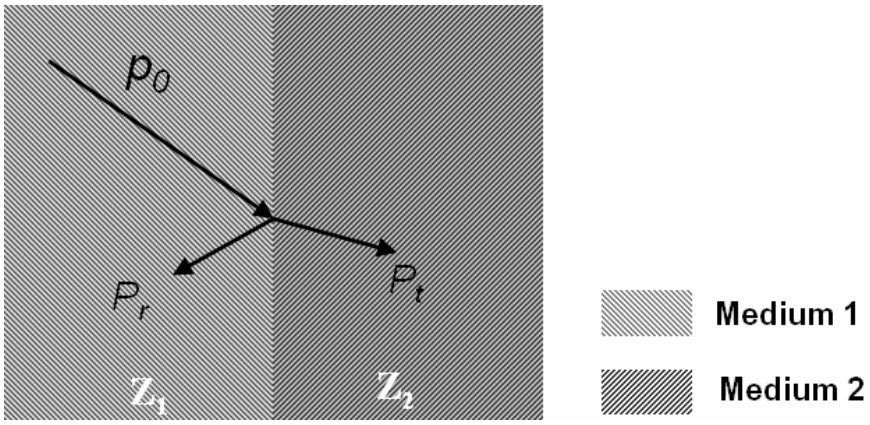

Figure 2.6 Schematic view of the reflection and transmission of the acoustic wave

An acoustic wave propagating through the media boundary can be partially reflected and transmitted, depending on the acoustic impedances of the media. Neglecting the absorption and scattering of the sound at the boundary, the original sound intensity I_0 splits into the reflection I_r and the transmission I_t [204]:

$$I_0 = I_r + I_t \tag{2.18}$$

Accordingly, reflection I_r and transmission I_t are,

$$I_r = \left(\frac{Z_2 - Z_1}{Z_2 + Z_1} \right)^2 I_0 \tag{2.19}$$

$$I_t = \frac{4 Z_2 Z_1}{(Z_2 + Z_1)^2} I_0 \tag{2.20}$$

Here, Z_1 and Z_2 are the acoustic impedances in the corresponding media.

The reflection P_r and the transmission P_t sound pressure can be estimated by [204],

$$p_r = \frac{Z_2 - Z_1}{Z_2 + Z_1} p_0 \tag{2.21}$$

$$p_t = \frac{2 Z_2}{Z_2 + Z_1} p_0 \tag{2.22}$$

Hence, the reflectance and the transmittance factor r_{12} and t_{12} are defined as [204]:

$$r_{12} = \frac{Z_2 - Z_1}{Z_2 + Z_1} \tag{2.23}$$

$$t_{12} = \frac{2Z_2}{Z_2 + Z_1} \tag{2.24}$$

2.5.2 Attenuation

Both the absorption and scattering can lead to the attenuation of an acoustic wave. In a homogeneous and static liquid, the attenuation is mainly caused by acoustic absorption due to the viscosity and heat conduction of the medium. Usually, an attenuation coefficient α_{ac} is adopted to sum attenuation caused both by absorption and scattering. The sound intensity I at the distance d from its source can be calculated by the following equation [204],

$$I = I_0 e^{-\alpha_{ac} d} \tag{2.25}$$

where I_0 is the initial sound intensity. For most liquids, the attenuation coefficient α_{ac} is a material-dependent quantity, which is inversely proportional to the square of sound frequency v_{ac} and proportional to the distance d [204]:

$$\alpha_{ac} = \frac{d}{v_{ac}^{\ 2}} \tag{2.26}$$

The attenuation coefficient of water is 24 × 10^{-15} dB·s^2·m^{-1}. The acoustic attenuation coefficients for most bio-tissues and liquids are summarized in ref. [205].

CHAPTER 3

Photoacoustic Spectroscopy

Contents

Although the layout of PA spectroscopy varies from case to case, a PAS contains at least four essential components: (1) a light source used to generate the PA signal; (2) a cell containing the sample; (3) a means to detect the acoustic signal; (4) a signal processing device. The basic arrangement of the above four components is shown in Figure 3.1. The periodic radiation excites the sample in the cell and generates an acoustic signal. The signal is collected by an appropriate acoustic detector and is processed to provide valuable information for different purposes. In the following section, a more detailed discussion about these components is given.

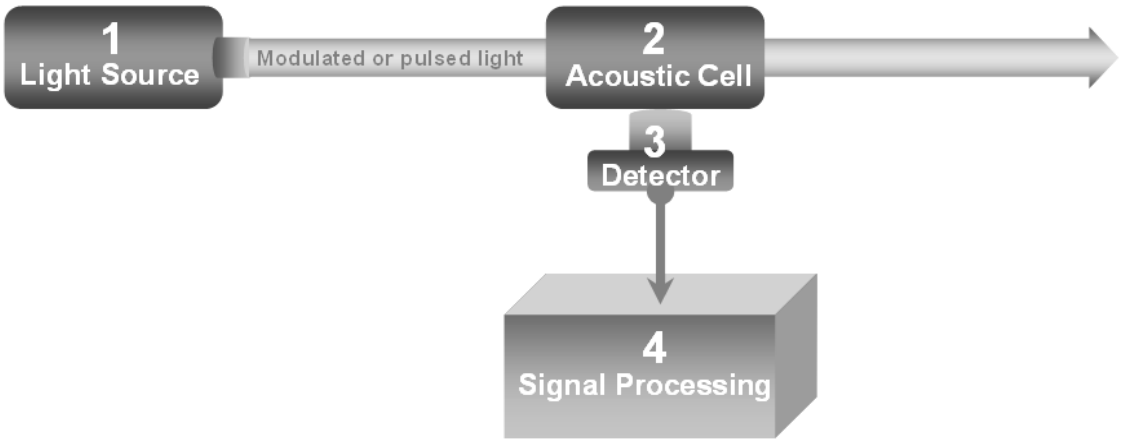

Figure 3.1 Essential components of a PA spectroscopy

3.1 Light Sources

Both modulated and pulsed light sources are capable of generating PA signals [166, 197, 206]. But the resulting physical effects are substantially different. As results, the corresponding acoustic cells, detectors as well as signal processing methods applied in these two excitation schemes are different.

3.1.1 Modulated Excitation

In the case of modulated excitation, the heat generated from the point of absorption diffuses into the surrounding medium [207]. Periodic heating caused by modulated light leads to generation of a "thermal wave" propagating in the medium. However, in the strict sense, the "thermal wave" is not an exact wave for the absence of negative half-wave. The temperature at the point of absorption can not fall below the initial starting level. But this term is commonly used.

An efficient and inexpensive way is to use a mechanical chopper that periodically blocks a continuous-wave source, resulting a periodically fluctuation of the light intensity in the shape either a square or a sine wave. The modulation frequencies obtained by mechanical chopping range from a few Hz up to several kHz. The resulting acoustic signals are usually in audible range and thus can be detected by a microphone.

Usually, the classic combination of lamp and monochromator serves as the continuous-wave source, which offers the possibility of continuous tunability from the infrared to the vacuum ultraviolet. But this combination suffers from a limitation of a relative large bandwidth.

3.1.2 Pulsed Excitation

Pulsed lasers with their monochromatic and intensive light are widely employed for PA generation. For quantitative and spatially resolved PA measurements, the excitation source has to fulfill the conditions of thermal confinement and stress confinement. Thermal confinement ensures that heat conduction to the outside of illuminated volume

is negligible during the laser pulse excitation. Stress confinement ensures the laser pulse is shorter than the stress relaxation time (for the theory see e.g. [193, 208]). Typical pulse duration fulfilling these requirements is below 100 ns. Hence, short laser pulses with duration of a few nanoseconds are usually utilized for PA generation. The short laser pulses excite the medium and generate a wide-band thermo-elastic pressure wave propagating outside of the illuminated volume, which can be detected by an appropriate detector.

Pulsed lasers provide many advantages over modulated sources, despite the limited tuning range and the high cost. For one thing, pulsed lasers provide higher power pulses and create a stronger PA signal than modulated sources. In addition, the resulting pressure wave is in ultrasonic range. Hence, the signal is easy to separate from low frequency background noise. Further, generally speaking, the delay time of signal between the excitation and the detection of the pressure wave corresponds to the distance between the illuminated region and the detector. Hence, the noise produced outside the illuminated region or by the light scattering, can be distinguished from the signal.

3.2 Acoustic Cells

Most common acoustic cells used in modulated excitation for gas phase analysis adopt a simple cylindrical symmetry. The excitation source is a small diameter light beam that excites the cell along the cylinder axis. The resulting acoustic wave propagates radially outward perpendicular to the exciting beam. Usually, the illumination period for modulated source is long enough that the propagation of the acoustic wave during this period exceeds the volume of the sample. Hence, the boundary conditions of the sample have to be considered in the design of acoustic cell. The eigenmodes of the acoustic cell are important factors. This fact can be used for signal amplification by acoustic cell resonance [209-210]. The amplification factor Q can be as large as 1000. Accordingly, due to their great influence in the signal enhancement, cell resonances must be considered in an acoustic cell design in this case.

Acoustic cells used in pulsed laser PA spectroscopy are different from those used in modulated excitation. Most acoustic cells used in pulsed laser PAS operate in a non-resonant mode, since the low repetition rate of the lasers. The other factor that must be considered is to minimize extraneous signals generated by pulsed laser, due to large photon fluxes.

3.3 PA Detectors

The choice of a PA detector for a specific application should give full consideration of many factors, such as detection style, sensitivity, response time, bandwidth, impedance matching, noise, size and ruggedness etc. [211]. A microphone is widely used as detector in gas phase analysis. But it does not couple very well to PA signals produced in condensed samples. An alternative PA detector is the piezoelectric transducer.

3.3.1 Piezoelectric Transducers

Piezoelectric transducers offer good acoustic impedance match to condensed samples and are capable of detecting much higher acoustic frequencies [165, 212-213]. In this section, we mainly discuss the characters of the piezoelectric transducer.

The piezoelectric effect was first discovered in natural crystals with a certain type of asymmetry in the lattice. Any pressure variation causes distortions in the crystal structure, followed by a redistribution of charged elements in the lattice. Accordingly，a voltage emerges on the surface of the crystal.

The voltage response to a plane pressure wave increases linearly to the thickness of the piezoelectric element, and also depends on the piezoelectric constants of the materials. But, once the thickness exceeds the acoustic wavelength, a further increase will not increase the output voltage. However, the response voltage to a non-plane pressure wave is complicated, since the pressure distribution is not constant for the entire surface. Thus, in this case, the cross-sectional area of a piezoelectric transducer should be considered.

The commonly used piezoelectric materials include three types: single crystals (lithium niobate, quartz), polycrystalline ceramics (lead zirconate-titanate, barium titanate, lead metaniobate) and polymers (PVDF, Teflon and Mylar) [214]. The parameters of three widely used piezoelectric materials are listed in the following table.

Table 3.1 Properties of commonly used piezoelectric materials [214].

		$LiNbO_3$ (z-cut)	PZT-5A	PVDF
Piezoelectric constant	d_{33} (10^{-12} C/N)	6	374	-39 ~ -44
	g_{33} (Vm/N)	0.023	0.025	- 0.32
Mechanical Q factor		100	75	5 ~10
Density (g/cm^3)		4.64	7.7	1.78
Sound velocity (m/s)		7316	4500	2260
Acoustic impudence (10^6 $kg/(m^2s)$)		33	35	4
Work temperature (^oC)		< 1100	< 300	< 60
Advantages		wideband rugged	high sensitivity inexpensive	wideband inexpensive
Disadvantages		expensive	narrowband ringing	non-rugged

3.3.2 Optical Detection

The acoustic signal in a liquid can also be indirectly detected by optical methods. One of the detection schemes is based on sensing the change of the refractive index of the sample. Since the refractive index varies as a function of density and temperature. Periodic heating of the sample leads to a change of the refractive index. Furthermore, the propagation of the resulting pressure wave also generates a density shift along its path. Hence, a technique called probe beam deflection or thermal lens has been developed to detect PA signals [197, 215-219]. The change of the refractive index is sensed by a probe beam that is sent through the sample with the pump beam. Thus,

refractive index variations in the sample are manifested as variations of light intensity of the probe beam. Two examples are given in following figures: transmitted [215] and reflected [218-219] probe-beam detection method.

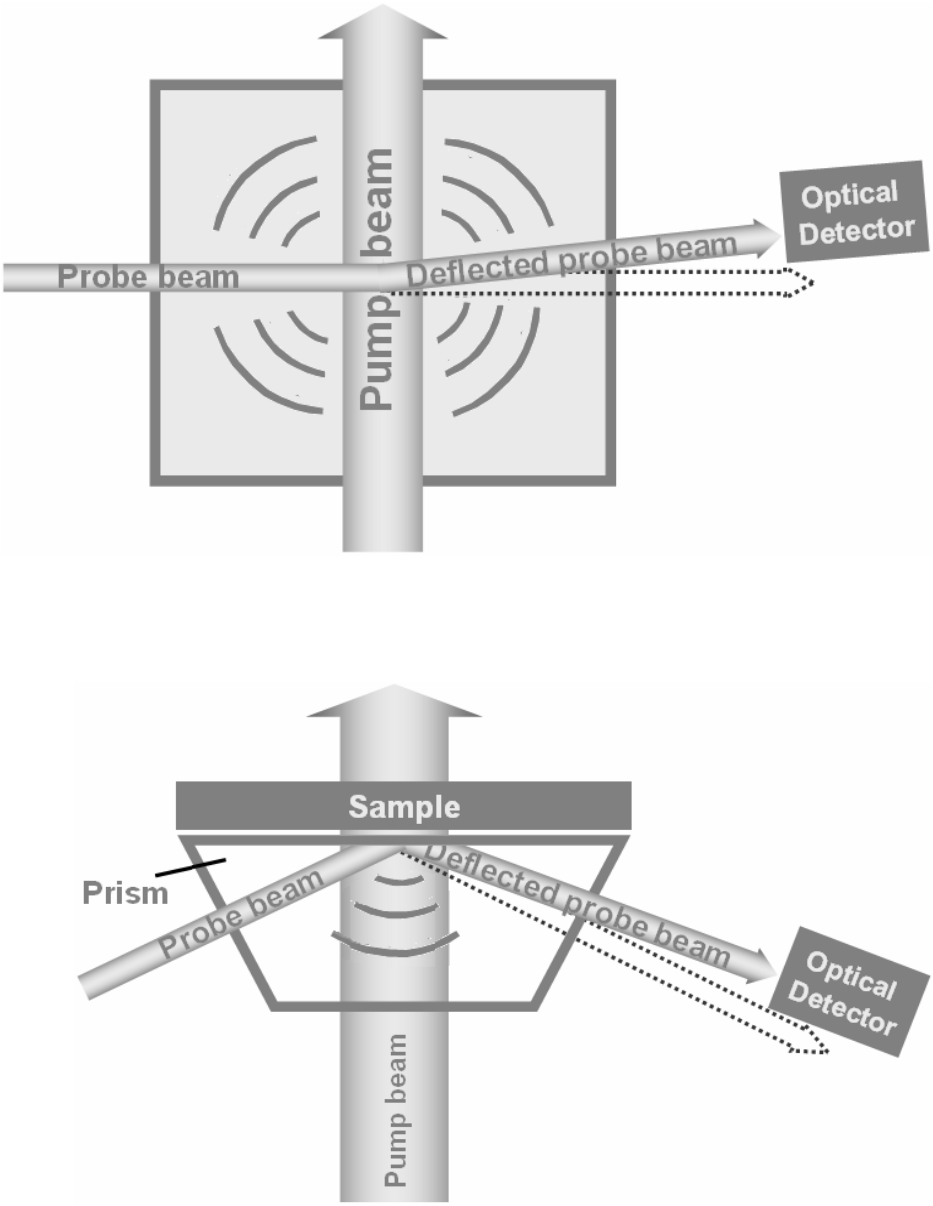

Figure 3.2 Transmitted (top) and reflected (down) probe-beam deflection technique.

3.4 PA Signal Processing

Signal processing in pulsed laser PA experiments often involves three steps: amplification, filtering, and signal averaging [211]. In order to prepare the PA signal for averaging, amplifiers should be very low-noise and broad-banded (~ MHz) devices. After the amplification, a filtering procedure may be performed, which depends on the specific information needed. For example, a high-Q filter is used to select the dominant frequency component in a complex PA signal. A band-pass filter is for eliminating the noise (especially f^{1} noise). Sometimes, in order to ensure the accuracy of a time evolution PA signal, no filtering process is performed. In the next step, the PA signal can be averaged by a boxcar integrator, a waveform educator, a transient recorder or a lock-in averager.

II Research Work

PART A

Strong Size-Dependent PA Effect and its Applications

CHAPTER 4

Strong Size-Dependent PA Effect on GNPs

Contents

4.1 Laser-Induced Nanobubble on GNPs

Metal nanoparticles (NPs) with strong surface plasmon resonance absorption, tunable in the visible and near-infrared spectral ranges, can be used for PA detection [220-221]. Laser interactions with NPs in aqueous media have been extensively studied to develop biosensors, medical imaging, and therapeutic applications [222-223]. It is well known that the PA signal from a homogeneous liquid is directly proportional to its absorbance and to the laser fluence [224]. However, the situation is different for the PA signal of a weakly absorbing liquid containing strongly absorbing nanoparticles. At low laser fluence, the PA signal results from the thermoacoustic response of both the host liquid and the NPs [120], which is a situation similar to homogeneous liquids. Once a certain laser fluence threshold (F_c) is reached [225], the temperature of the NP exceeds the boiling point of the host liquid, and a vapor layer is formed on the surface of the NP. This phenomenon is called laser-induced nanobubble (LINB). The resulting vapor layer expands rapidly, and generates an intense PA signal, as plotted in Figure 4.1. This phenomenon has been widely used for increasing sensitivity of PA diagnosis [226], or anti-tumor therapy, e.g., by selective photothermolysis [227].

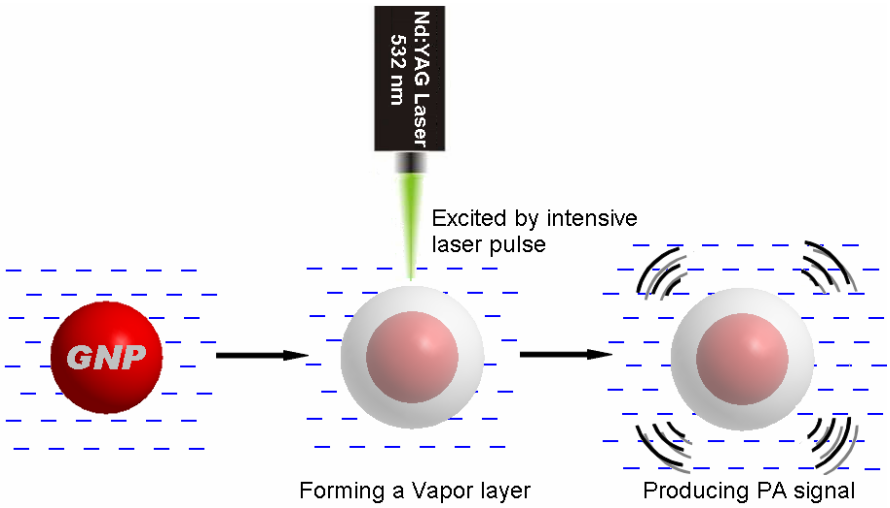

Figure 4.1 Schematic illustration of laser-induced nanobubble on GNP.

The amplitude of PA signal from LINB is no longer proportional to the absorbance of the NPs suspension. A proof for this assumption can be found in the following experiment. Gold colloids with different sizes were diluted to obtain the same absorbance (0.226 cm^{-1}) at the laser wavelength of 532 nm (see Figure 4.2a), and tested by our PA setup. As mentioned above, the PA signal of a homogeneous liquid is directly proportional to its absorbance. Hence, homogeneous liquids with equal absorbance will generate identical PA signal intensity. However, the corresponding PA amplitudes from the above mentioned gold colloids exhibit a size-dependent feature (Figure 4.2b). This fact proves the difference of PA behavior between GNPs and homogeneous liquids.

In the above experiment, the absorbance of diluted GNPs was determined by UV/Vis spectrometry. It should be mentioned here, the UV/Vis measurements reveal extinction values rather than absorbencies. But, due to the small size of the GNPs, scattering light only accounts very small part in extinction and thus can be neglected here.

It should be noted here, details of experiments are described in the Experimental Section at the end of this thesis, including experimental setup, materials and nanoparticles synthesis. The protocol of above experiment can be seen in the List of Experiments in this section (see Ex.1).

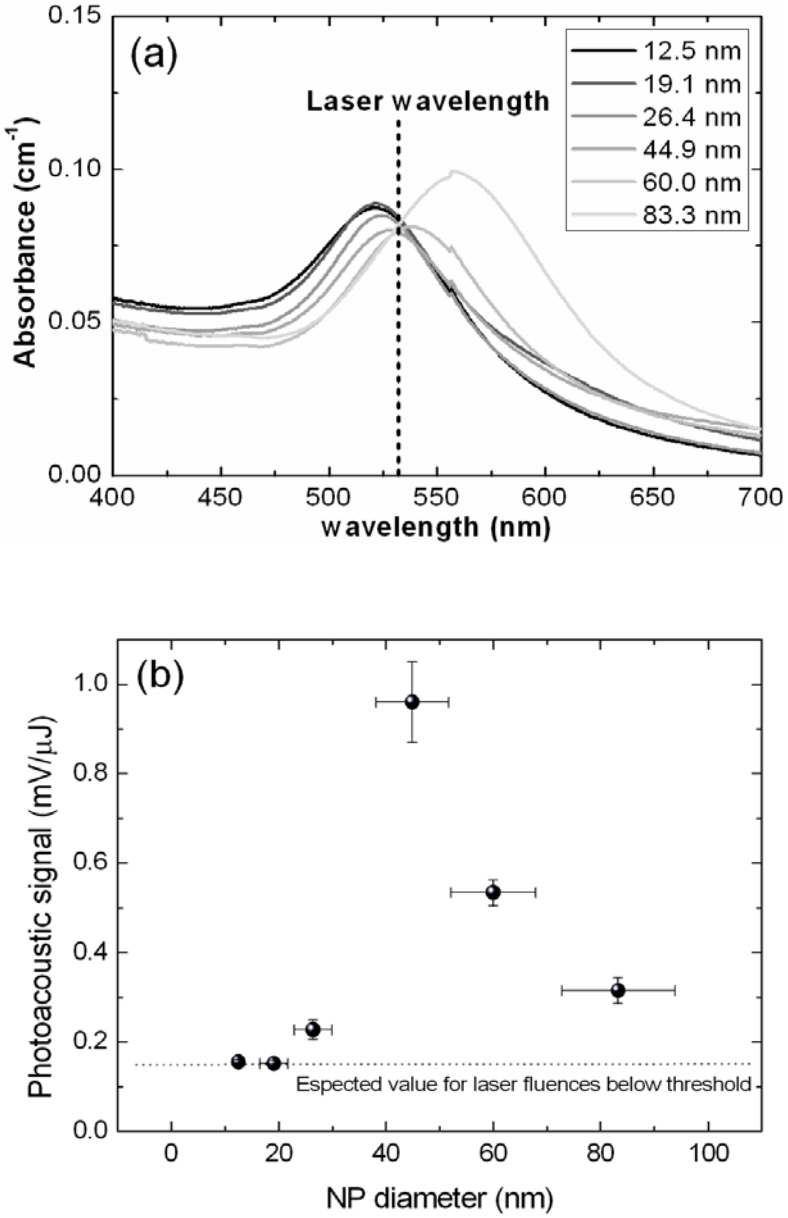

Figure 4.2 (a) Gold colloids with different sizes were diluted to obtain the same absorbance at 532 nm and (b) their PA signal amplitude.

4.2 Strong Size-Dependent PA Effect on GNPs

Several theoretical studies have been performed to investigate and model laser-induced nanobubble generation on nanoparticles [120, 224, 228-230]. A recent publication describes the formation of nanobubbles around a superheated nanoparticle [225], an expression for the resulting PA signal as a function of the laser pulse energy was given.

We introduce a new general equation to explain the observed PA effect generated by LINB in colloidal gold. To obtain the equation, a simulation based on the widely known Rayleigh–Plesset cavitation model was developed (see Simulation in the Experiment Section) [231]. It should be mentioned here, the discussion in this thesis is limited to a fluence regime well below the plasma breakdown threshold, which is experimentally investigated by several authors [232-234].

Assuming that all the excess light energy absorbed by the particle during the laser pulse is spent to heat water at the critical temperature, the initial radius $R_{b,0}$ of the bubble can be estimated as

$$R_{b,0} = \left\{ \frac{3}{4\pi\rho_{cw}} \left[\frac{(F - F_c)\sigma_{abs}}{E_{cw}} \right] + \frac{D_{np}{}^3}{8} \right\}^{1/3} \tag{4.1}$$

where D_{np} is the diameter of a spherical NP, ρ_{cw} is the critical density of water, σ_{abs} is the NP absorption cross section, F is the fluence of the laser, E_{cw} is the internal energy of water at the critical point, and F_c is the threshold fluence for bubble generation [225]. After the initiation of the boiling, the dynamics of the bubble are governed by the Rayleigh–Plesset equation [235-237]:

$$\frac{P_b(t) - P_A}{\rho_w} = R_b(t)\frac{d^2R_b(t)}{dt^2} + \frac{3}{2}\left[\frac{dR_b(t)}{dt}\right]^2 + \frac{4\upsilon_w}{R_b(t)}\frac{dR_b(t)}{dt} + \frac{2\gamma_w}{\rho_w R_b(t)} \tag{4.2}$$

where $p_b(t)$ is the pressure inside the bubble, ρ_w is the water density, p_A is the atmospheric pressure, υ_w and γ_w are the kinematic viscosity and the surface tension of water, respectively. The term containing the surface tension gives a positive contribution to the $p_b(t) - p_A$ term on the left side of the equation, whereas the viscosity acts as a friction force to bubble motion and is responsible for damping the oscillations [238]. The acoustic pressure generated by the dynamic motion of the bubble and the pressure exerted by the gas on the liquid can be considered directly proportional to the second time derivate of the bubble volume $V(b)$ [225, 237]:

$$p_{ac}(t) \propto \frac{d^2V_b}{dt^2} = \frac{d^2}{dt^2}\left[\frac{4}{3}\pi\left(R_b{}^3 - \frac{D^3{}_{np}}{8}\right)\right] = 8\pi\left[R_b\left(\frac{dR_b}{dt}\right)^2 + 2R^2{}_b\frac{d^2R_b}{dt^2}\right] \tag{4.3}$$

The simulation program was developed based on the Eq. 4.1 ~ 4.3. The temperature and the pressure inside the initial bubble are those at the critical point of water (T_{cw}, p_{cw}). The acoustic pressure responses (p_{ac}) for various gold nanoparticles GNP sizes (10 nm ~ 100 nm) were studied at different laser fluences ($10F_c$ ~ $100F_c$). The results of the simulation are shown in the following figure.

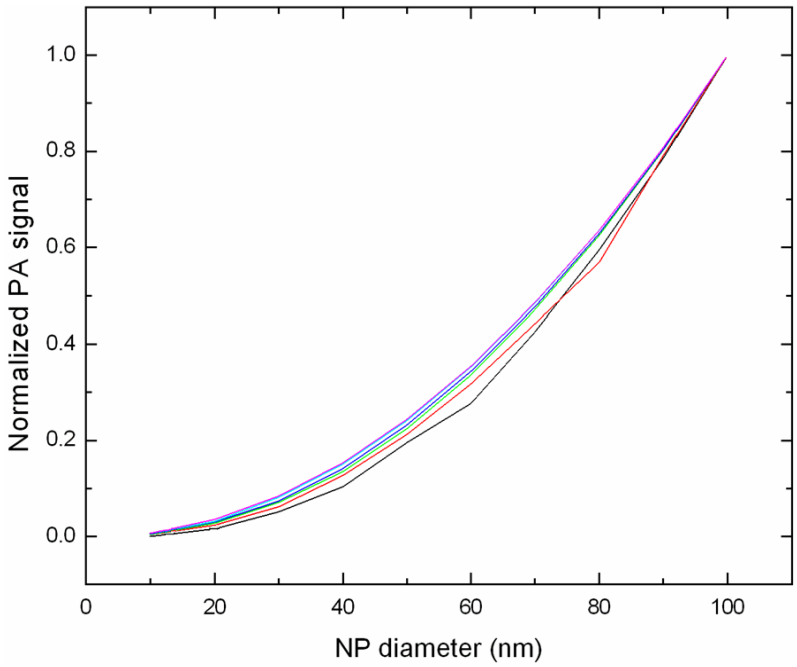

Figure 4.3 Simulation of PA amplitudes of GNPs under different laser fluences ($10F_c$ ~ $100F_c$).

The result obtained from the simulation reveals the following relationship between the PA signal of single GNP and its diameter:

$$p_{ac} \propto D_{np}^3$$

Thus, we propose the following approximated equation for the PA response (*PA-LINB*) generated by LINB in GNPs suspensions:

$$PA-LINB = C \cdot \kappa \cdot F \cdot N_{np} \cdot D_{np}{}^3 \qquad (4.4)$$

where C is a constant that depends on the experimental setup, κ accounts for the dielectric properties of the GNP, N_{np} is the number concentration of GNPs in the host liquid, and D_{np} is the GNP diameter.

4.3 Proofs of the Theory

In order to verify the accuracy of Eq. 4.4 on real samples, GNPs of different average sizes were prepared (see Experimental Section) [44, 239-240]. The GNP sizes were verified by TEM collected by a JEOL JEM 2010 instrument (at least 200 particles were measured), as shown in Figure 4.4. Additionally, the theoretical threshold fluences F^t_c are shown in the Table 4.1.

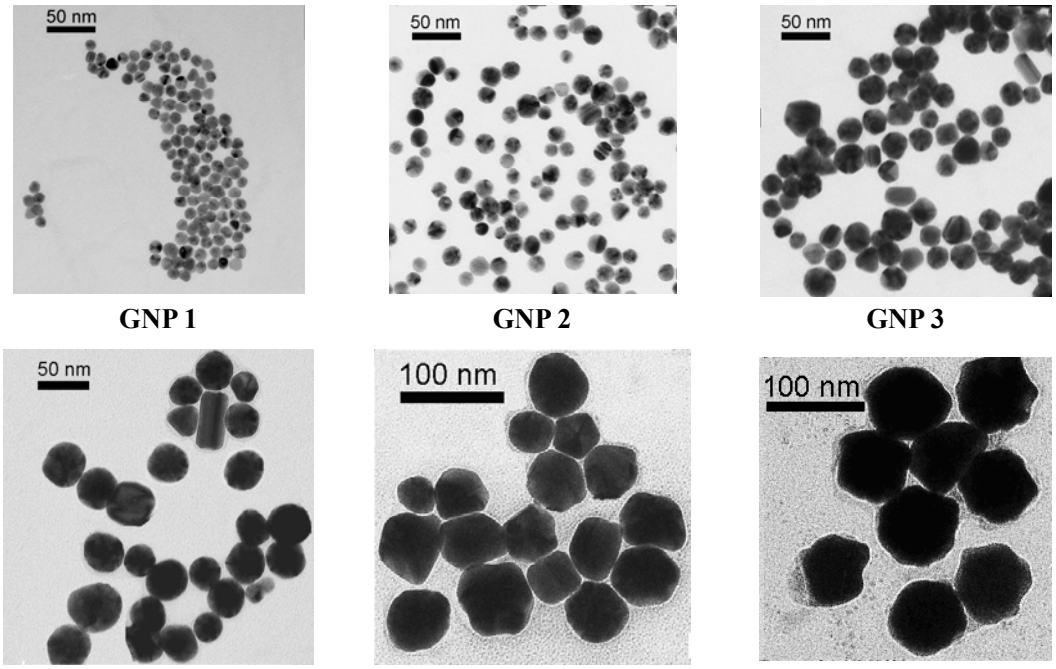

Figure 4.4 TEM images of GNPs.

Table 4.1 Detailed information about the GNPs used in this thesis. The absorption peaks and their intensities were obtained by means of a UV/Vis spectroscopy. F^tc: theoretical laser fluence threshold.

	GNP 1	GNP 2	GNP 3	GNP 4	GNP 5	GNP 6
λ_{max} (nm)	518.0	526.0	522.5	525.5	537.0	560.0
Diameter (nm)	12.5 ± 1.0	19.1 ± 2.6	26.4 ± 3.5	44.9 ± 6.8	60.0 ± 7.9	83.3 ± 10.5
Number concentration (particles /mL)	1.5×10^{13}	1.5×10^{12}	6.0×10^{12}	1.5×10^{11}	3.0×10^{10}	1.2×10^{10}
F^t_c (J/cm^2)	0.45	0.20	0.11	0.04	0.026	0.019

4.3.1 Dependence of PA-LINB on the Laser Fluence

The PA responses of gold colloids (GNP 1) as a function of laser fluence is shown in Figure 4.5 (see Ex. 2). A laser fluence threshold for LINB formation about 0.5 J/cm^2 can be observed. Below 0.5 J/cm^2, the signal increases gradually with the fluence and is attributed to thermoelastic expansion of the particles, i.e., conventional PA effect in the sub-bubble generation regime. Above the threshold, there is a sharp increase in the PA signal amplitude. The fluence for the onset of this strong acoustic signal (threshold for LINB formation) is similar to the value obtained in our simulations (see Table 4.1), and the value reported by other authors [225].

As predicted by the Eq. 4.4, the resulted PA-LINB amplitude should show a linear relationship to laser fluence above the threshold, when the diameter and the particle concentration of colloidal gold are constant,

$$PA - LINB \propto F \tag{4.5}$$

Such a linear relationship can be observed in Figure 4.5, for laser fluence ranges between F_c and $100F_c$. In other words, the experimental results show good accordance with the Eq. 4.4.

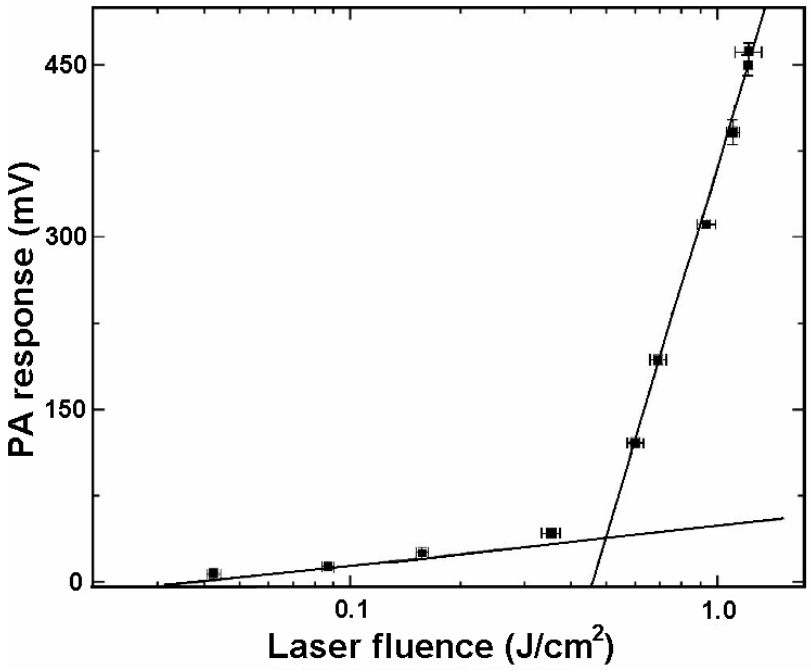

Figure 4.5 PA-LINB as a function of laser fluences for GNP 1 (12.5 nm)

It should be noted here, there is a possibility that GNPs break into smaller particles, if the laser fluence F is over $100F_c$. We observed a decrease in PA signal when GNPs (26 nm) were constantly illuminated by intensive laser pulses. After comparing UV/Vis spectra of GNPs before and after the laser irradiation, we concluded that the observed PA decrease is due to a breakdown of GNPs (data not shown). This effect has already been reported for colloidal silver [241] and gold colloids [242]. The reasons for this phenomenon are discussed by McGrath et al. [243].

4.3.2 Correlation between the PA-LINB and Particle Concentration

According to Eq. 4.4, *PA-LINB* should show a linear relationship to the concentration of GNPs, if all other parameters are constants.

$$PA - LINB \propto N_{np} \tag{2.4}$$

The PA responses of gold colloids with various particle concentrations were measured (see Ex. 3). The results are shown in Figure 4.6. A linear correlation between the PA signal and the concentration of GNPs is observed. Hence, the approximation of the equation shows a good correlation with the experimental results.

It is worth mentioning that GNPs with an average diameter of 83.3 nm show a measurement error larger than the other particle sizes. This effect was also observed in highly diluted samples (below 10^9 particles/ml). Within this range of concentrations, the sample is highly inhomogeneous in the volume excited by the laser, resulting in a large pulse to pulse variation in the PA signal. The simulation carried out here, predicts that the time of bubble cavitation is proportional to the NP size at a fixed energy laser (see Simulation in Experimental Section). These time differences are measurable by our PA detector. Hence, two bubbles generated from NPs with different sizes in such micro-inhomogeneous sample will produce phase-shifted PA signals, causing interferences and signal broadening.

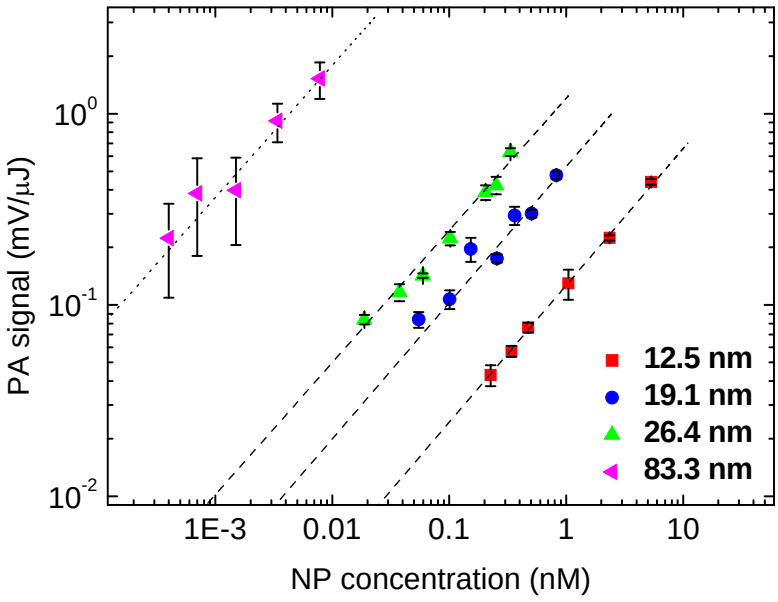

Figure 4.6 PA-LINB vs. NP concentration for different GNP sizes.

4.3.3 PA-LINB and the Size of GNPs

In Figure 4.7 the PA responses of six GNPs with different sizes (normalized to GNP concentration) are shown. In the same figure, the normalized simulation results are also plotted (see Ex. 4). A good correlation between the measured and simulated data could be demonstrated.

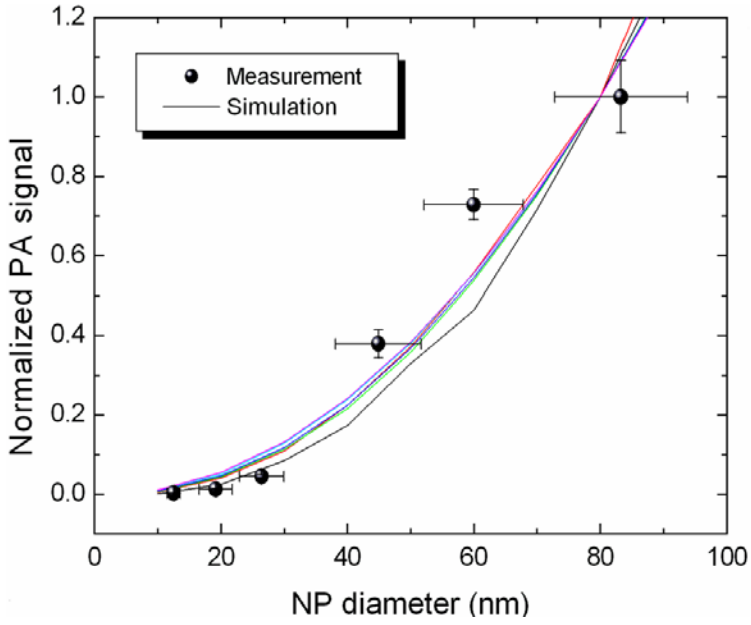

Figure 4.7 Normalized PA response vs. GNP sizes. Dots: measured values; Line: Normalized simulations (laser fluences $10F_c \sim 100F_c$).

4.4 Summary

The studies presented in this chapter show the Eq. 4.4 gives a good approximation to describe the PA signal generated from LINB on spherical GNPs (10 nm < D_{np} < 80 nm, $10F_c < F < 100F_c$).

One interesting feature of these phenomena is that the *PA-LINB* is sensitive to the size of GNP. Hence, in the following chapters, we will investigate the applications of *PA-LINB* in chemical and biological sensing, based on monitoring the variation of GNP sizes by *PA-LINB*.

CHAPTER 5

Strong Size-Dependent PA Effect Monitoring Leaching of GNPs for Pb^{2+} Detection

Contents

In this chapter, based on the strong size-dependent PA effect, a new way to detect Pb^{2+} in aqueous solution is described. Due to the fact that Pb^{2+} ions can accelerate the leaching of GNPs in the presence of thiosulfate ($S_2O_3^{2-}$) and 2-mercaptoethanol (2-ME) [244-245], monitoring the decreasing GNPs size allows the quantification of the Pb^{2+} ions in the sample. As described in previous chapter, the amplitude of PA-LINB strongly depends on size of GNP. Hence, the quantification of Pb^{2+} ions can be achieved by monitoring the change of PA-LINB of GNPs.

5.1 Monitoring Toxic Metal Ions

Lead is one of the most widely used heavy metals and has a large number of industrial applications, e.g., battery manufacturing, radiation shield alloys, etc. Lead in paint and gasoline accounts for most of the content present in environment and causes serious pollution and human health problems. It is known that lead enters the human body by ingestion and inhalation, and it is associated with damage to the kidney, the liver and the gastrointestinal tract, as well as with neurological degeneration and decreased hemoglobin production [246]. The maximum contamination level for lead in drinking water is defined by the U.S. Environmental Protection Agency to be 75 nM [247].

Several methods for lead analysis have been developed. The commonly used methods are atomic absorption spectrometry, atomic emission spectrometry [248], and inductively coupled plasma/mass spectrometry (ICP/MS) [249]. These techniques are sensitive, accurate and allow discrimination among other metal ions. However, they are time-consuming, expensive, and/or require complex sample pretreatment and sophisticated equipment. Other methods for the detection of Pb^{2+}, using chromophores [250], aptamers [251], oligonucleotides [252], polymers [253], antibodies [254], or functionalized nanoparticles [255] were also established. However, many of them possess limited practical use for different causes such as poor aqueous solubility, high costs, complicated processing or poor sensitivity and selectivity.

5.2 Pb^{2+} Detection based on Strong Size-Dependent PA Effect

Recently, based on leaching of GNPs probe, a colorimetric method has been developed for the detection of Pb^{2+} in aqueous solution [256]. When the GNPs reacted with $S_2O_3^{2-}$ ions in solution, $Au(S_2O_3)_2^{3-}$ complexes (see following equation) were formed immediately on the GNP surfaces. After adding Pb^{2+} ions and 2-mercaptoethanol (2-ME), the GNPs rapidly dissolved to form Au^{+}-2-ME complexes in solution [244-245]. As a result, the SPR absorption of GNPs decreased dramatically and the corresponding change can be detected by a UV/Vis spectroscopy, allowing quantification of Pb^{2+}. This chemical process is depicted in Figure 5.1

$$4Au^{0} + O_2 + 2H_2O + 8S_2O_3^{2-} \rightarrow 4Au^{I}(S_2O_3)_2^{3-} + 4OH^{-} \qquad 5.1$$

As shown by the authors [256], this approach is highly sensitive as well as selective, and avoids the need for sophisticated equipment. Furthermore, this method is also suitable for real-world samples, and the cross-sensitivity to many other metal ions is at least 1000 times lower than the system's reaction on lead ions.

Here, we present a modification of the method. Instead of UV/Vis spectrometer, the leaching of GNPs is monitored by *PA-LINB*. According to the strong size-dependent PA effect, the decreasing of GNP diameter will lead to the corresponding PA-LINB decrease, which allows quantification of the Pb^{2+} ions in the aqueous solution. Figure 5.2 outlines the sensing mechanism employed in this chapter.

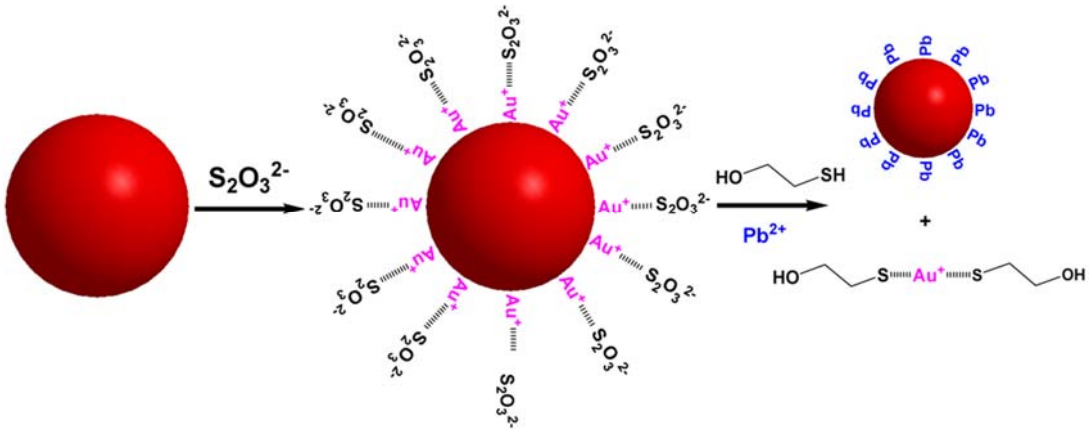

Figure 5.1 Cartoon representation of the leaching of GNP.

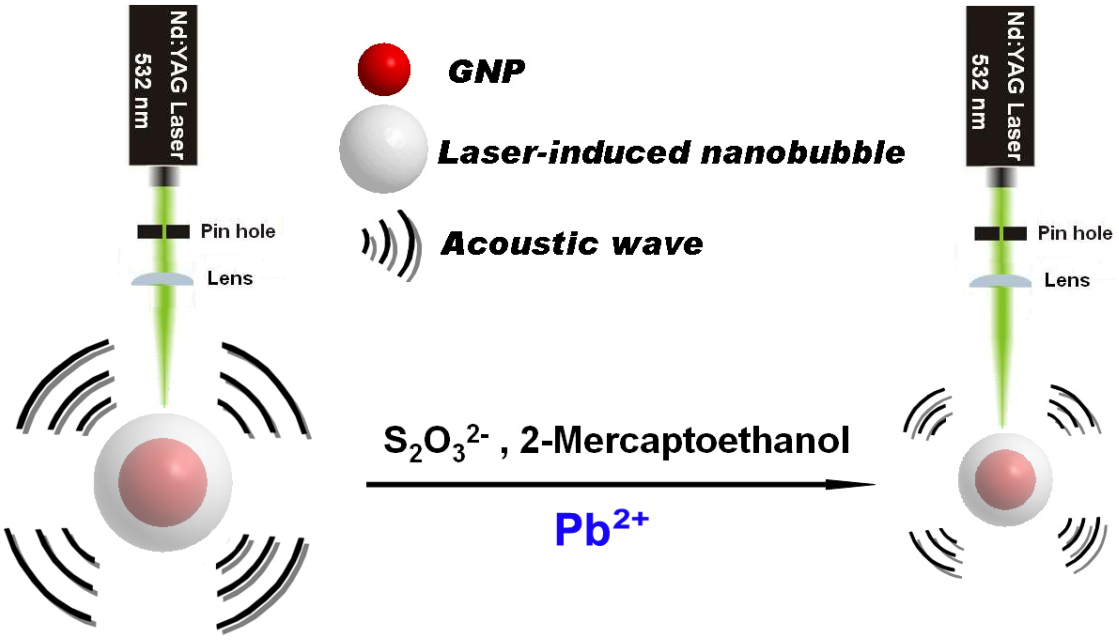

Figure 5.2 Schematic illustration of Pb^{2+}-triggered GNP leaching causing the amplitude of PA-LINB decreasing.

5.3 Feasibility

In order to test the feasibility of the *PA-LINB* in detecting the size variation of GNPs, three samples, containing different concentration of Pb^{2+}, were measured by the PA system (see Ex. 5). Both the PA signals before (S_0) and after (S) leaching was measured. The corresponding sizes of GNPs before (D_0) and after (D) leaching were verified by TEM images (Figure 5.3). According to Eq. 4.4, assuming the number concentration of GNPs and other parameter remain constant, the ratio of S/S_0 can be estimated by

$$\frac{S}{S_0} = \frac{D^3}{D_0^{\,3}} \tag{5.1}$$

Hence, S/S_0 and D^3/D_0^3 were calculated and compared in Table 5.1. We found that the S/S_0 showed good accordance with the estimated values of D^3/D_0^3. This fact can be seen as another proof of the Eq. 4.4. On the other hand, it also proved that the *PA-LINB* is capable of sensing the size variation of GNP in this case.

Figure 5.4 shows evolution of the *PA-LINB* (normalized to the value before leaching) over the time after the addition of Pb^{2+} (see Ex. 6). The *PA-LINB* decreased significantly when the leaching process starts and then gradually saturated until the action reaches equilibrium. For comparison, the corresponding UV/Vis spectra of the GNPs were also collected under the same conditions. In the same figure an evolution of extinction values at 520 nm normalized to the value before leaching is also shown. A similar phenomenon was observed that extinction at 520 nm also decreased significantly after the addition of Pb^{2+}.

As it can be seen in Figure 5.4, the *PA-LINB* technique generally offers a good time resolution, since the response can be analyzed from pulse to pulse. However, it has to be stated that the temporal resolution of this specific lead detection scheme is limited by the kinetics of the leaching process, which is in the range of an hour.

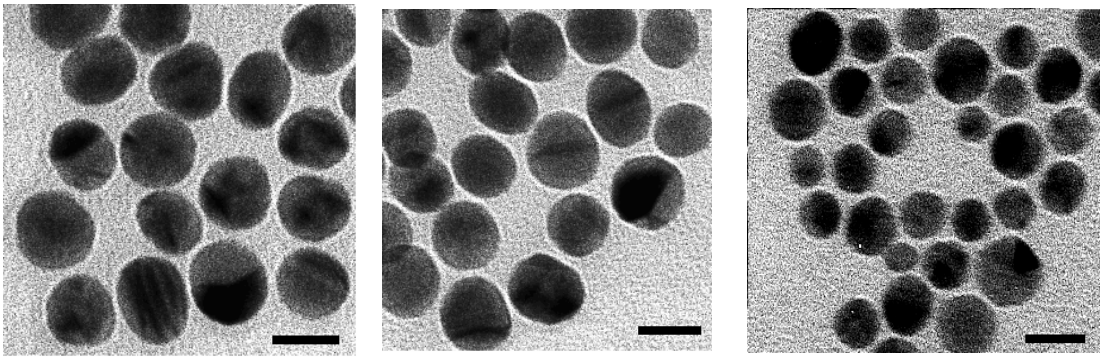

[Pb^{2+}] = 0 nM [Pb^{2+}] = 100 nM [Pb^{2+}] = 250 nM

Figure 5.3 TEM images of GNPs mixed with various Pb^{2+} (0, 100, 250 nM) in the presence of thiosulfate ($S_2O_3^{2-}$) and 2-mercaptoethanol (scale bar: 10 nm).

Table 5.1 Comparison between the PA response and the GNP diameter change resulting from leaching. The NP sizes were verified by TEM.

[Pb^{2+}]v (nM)	***PA-LINB* (V/J)**	***S*/*S*^{0}**	**NP diameter (nm)**	**Estimated *S*/*S*^{0} (*D*^{3}/*D*$_0^3$)**
0	539 ± 12	1.00	11.35 ± 0.97	1.00
100	405 ± 19	0.75	10.46 ± 1.07	0.78
250	238 ± 11	0.44	8.55 ± 1.38	0.43

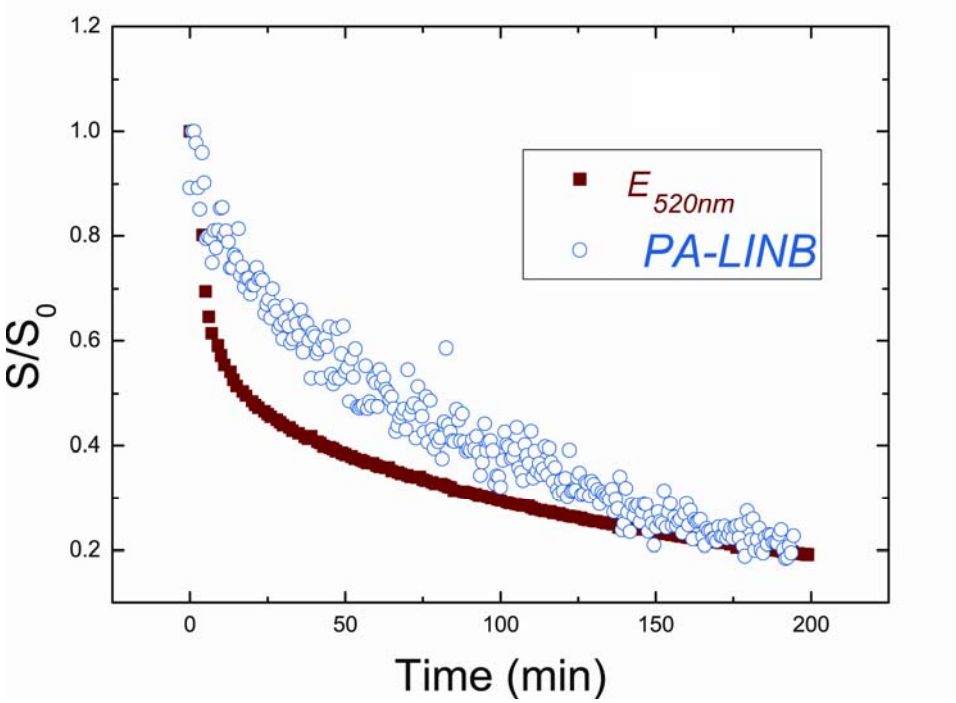

Figure 5.4 Time-dependent evolution of the *PA-LINB*, and the extinction at 532 nm ($E_{532\,nm}$) after addition of Pb^{2+}.

5.4 The Optimum Size for the Assay

In order to determine the optimum GNP size for this assay, five GNPs with different average sizes were used to perform the assay (see Ex. 7) [44, 239-240]. After the reaction between the GNPs and $S_2O_3^{2-}$, the lead ions and 2-ME were added, maintaining a constant ratio between the Pb^{2+} concentration and the total GNP surface. After 3 h, the PA responses were measured. Hence, the relative change of the signal Λ was calculated,

$$\Lambda = \frac{(S_0 - S)}{S_0} \qquad 5.2$$

Λ can be seen as an indicator for the sensitivity of the assay. As shown in Figure 5.4, Λ is inversely proportional to the GNP diameter as expected. According to the Eq. 4.4, the relative change of signal Λ is proportional to relative diameter change D/D_0. Clearly, for smaller particles, the relative size change D/D_0 is larger than for large particles to the same amount of Pb^{2+}, which makes the detection more sensitive. Hence, we chose the smaller GNPs (11 nm) for the assay. On the other hand, the background signal S_0 also depends on the GNP concentration. In order to increase Λ, the GNP concentration used in the assay should be as low as possible.

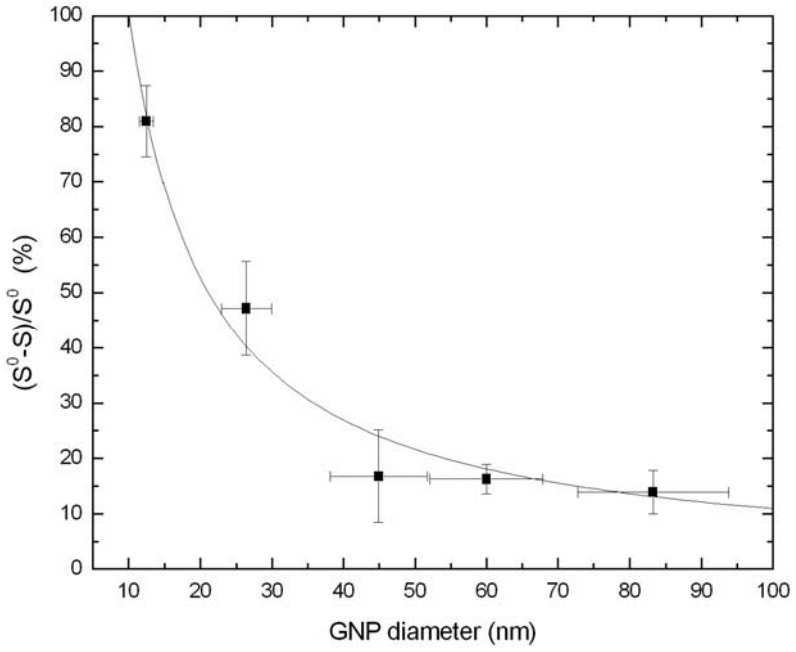

Figure 5.4 Responses of Λ to different GNP of diameters.

5.5 Sensitivity

Using 1.25 nM of GNP (11 nm), containing 1 mM of 2-ME, a linear relationship between Λ and the Pb^2 concentration from 1 nM to 2.5 μM was observed (Figure 5.5). The details of this experiment can be seen in Ex. 8. The limit of detection (S/N ratio = 3) was 0.5 nM. We repeated the procedure in the same way, measuring the extinction values at 520 nm with a UV/Vis spectrometer (colorimetric method). An approximate homologous sensitivity was obtained.

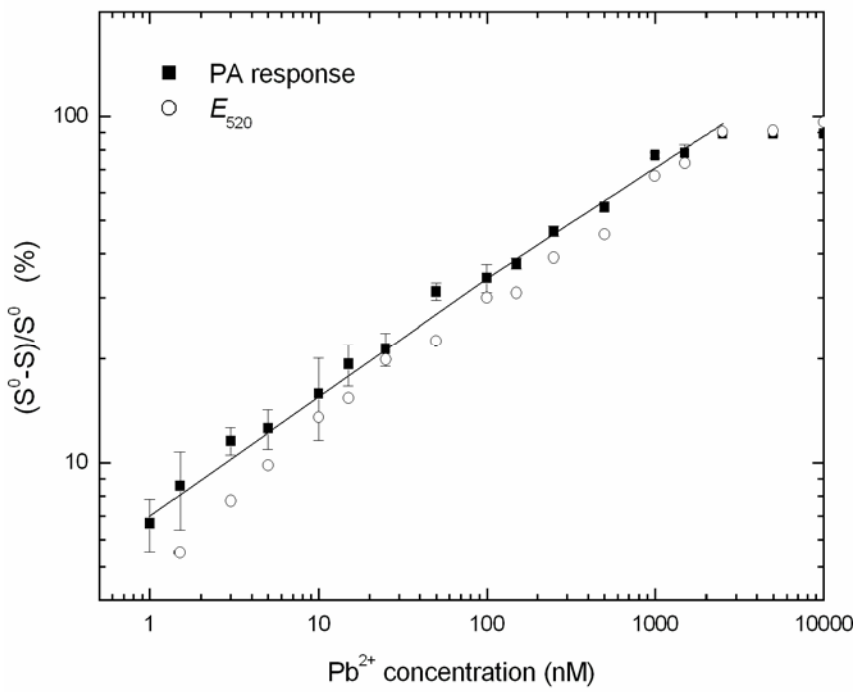

Figure 5.5 Responses of Λ to various Pb^{2+} concentrations (0 - 10 μM). Squares: PA responses; Dots: UV/Vis responses ($E_{520\,nm}$).

5.6 Assays in Scattering Medium

In a scattering medium, the spatial distribution of the light is different from the one observed in a non-scattering medium. The transmitted fraction of light is reduced even if no absorption takes place. In consequence, transmission based absorption measurements have a systematic error in scattering media. However, the influence of scattering light to PA measurement is relatively small.

In order to demonstrate this advantage of the PA over the colorimetric method, the scattering coefficient of samples containing lead ions was using spherical silica particles (diameter 500 nm). Figure 5.6 shows the measurements of the *PA-LINB* and the extinction values at 520 nm in this scattering medium. As expected, the results corroborate that the *PA-LINB* technique is widely insensitive to light scattering, whilst the conventional method presents an error larger than 100%. The details of this experiment can be seen in Ex. 9. Apart from the applicability for measurements in scattering media, we have no reason to assume that the performance of the PA-based approach is different from the classical UV/vis-based approach as described in ref. [256], regarding selectivity and reaction to environmental conditions like temperature and pH.

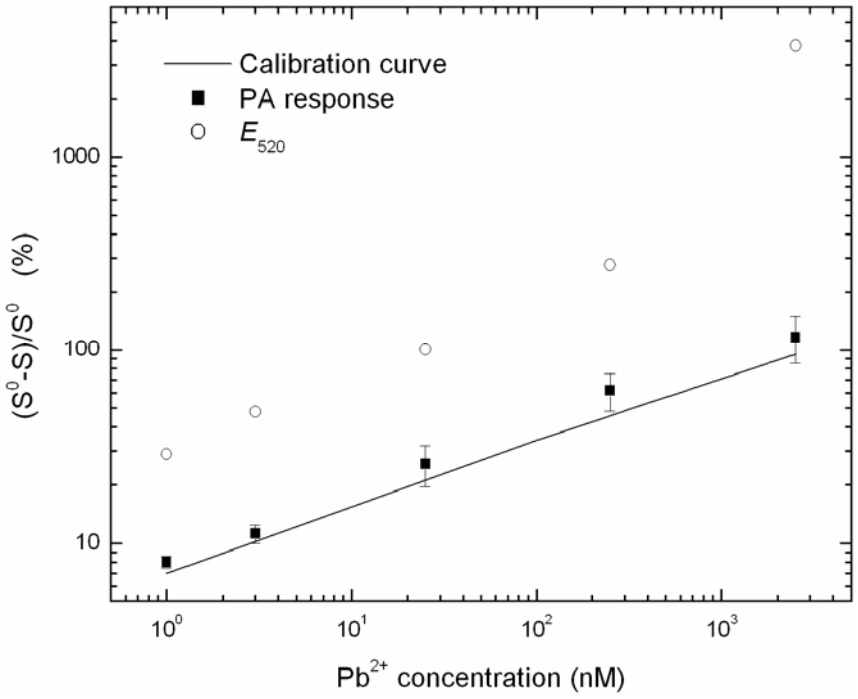

Figure 5.6 Detection of Pb^{2+} in a highly scattering medium (0.05 g/L of 500 nm silica in water). Squares: PA responses; dots: UV/Vis responses ($E_{520\,nm}$); solid line: calibration curve as shown in Figure 5.5 (in non-scattering medium).

5.7 Summary

In this chapter, we demonstrate that *PA-LINB* is a useful tool to monitor the decrease of GNPs, and a new assay to detect Pb^{2+} in aqueous phase based on leaching of GNP has been developed. This assay is highly sensitive and suitable for the application in scattering media.

On the other hand, the experimental results showed good accordance with prediction developed from Eq. 4.4. This fact proved the theory of strong size-dependent PA effect. Moreover, it also proved our primary assumption that *PA-LINB* can be used for sensing GNPs size.

CHAPTER 6

Strong Size-Dependent PA Effect for GNPs Aggregation Monitoring

Contents

As mentioned in CHAPTER 1, by switching to a more sensitive aggregation detecting tool, the sensitivity of the aggregation-based colorimetric assay can be improved 1 - 2 order [76-77, 91, 108-115, 137-139]. In this chapter, we present a new tool to detect GNPs aggregation based on the strong size-dependent PA effect.

6.1 Introduction

The demand for rapid, low-cost, and sensitive analytical methods in the field of molecular recognition is ever increasing. Currently, fluorophore label-based detection methods are dominating the market. Nanomaterials such as quantum dots, carbon nanotubes, silicon nanowires, and metallic nanoparticles, are proposed as alternative signaling probes for the detection [28]. Among them, gold nanoparticles (GNPs) have attracted enormous attention due to their unique size- and distance-dependent optical properties.

A common sensing mechanism is based on aggregation of receptor-conjugated GNPs in the presence of the target molecule, which leads to a color change of the GNPs suspension. This phenomenon can be detected by naked eyes or an UV/Vis absorption spectrometer. The technique has been applied for different purposes such as duplex DNA formation [119-120], protein-ligand interactions [122-123], immunological recognitions [124-125], and metal ion-ligand complexation [126-129]. The main

problem of these aggregation-based colorimetric methods is their limited sensitivity. An UV/Vis spectrometer can detect aggregation only if the aggregation level is high enough to cause a color change [138]. In order to enhance the sensitivity, many signal amplification strategies have been proposed [130].

However, these improvements often involve complicated multi-step procedures that are not only time consuming, but also can reduce the reproducibility of the results significantly. As a new tool for monitoring GNPs aggregation, dynamic light scattering has been introduced recently [137-139]. This technique has achieved a much higher sensitivity than UV/Vis absorbance spectrometry.

In this chapter, based on the strong size-dependent photoacoustic (PA) effect on GNPs, a new tool to monitor GNPs aggregation is demonstrated. Since the *PA-LINB* signal strongly depends on the GNP size [257] and GNPs aggregation can be understood as a particle size changing process, it can be hypothesized that the aggregation can cause a significant change of the *PA-LINB* signal amplitude. To demonstrate the feasibility of this approach, we present here the realization of the concept by target-triggered aggregation of GNPs for protein detection.

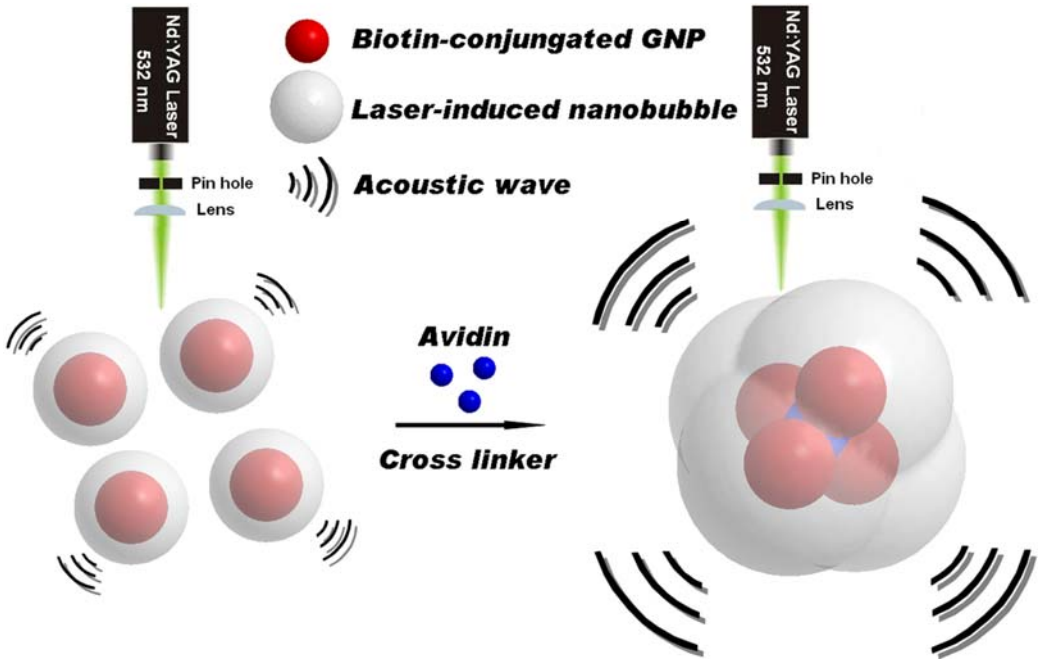

Figure 6.1 Schematic illustration of target-triggered GNPs aggregation enhancing the amplitude of *PA-LINB* signal for sensitive avidin detection.

6.2 Feasibility

As shown in Figure 6.1, the binding of avidin with two biotin-conjugated GNPs causes GNPs to form dimers, trimers, and larger aggregates. This GNPs aggregation increases the average diameter of the whole nanoparticle population. The subsequent change of *PA-LINB* can be measured by our photoacoustic setup [257] and correlated to the avidin concentration. The biotin-conjugated GNP probe was prepared by the classic thiol-gold method [28, 119-120]. As plotted in Figure 6.2, the -SH bonds were first modified by the reaction of N-(+)-biotinyl-6-aminocaproic acid N-succinimidyl ester and cysteamine. Afterwards, biotin is bound to the GNP surface by the high affinity of -SH and gold (see Experimental section).

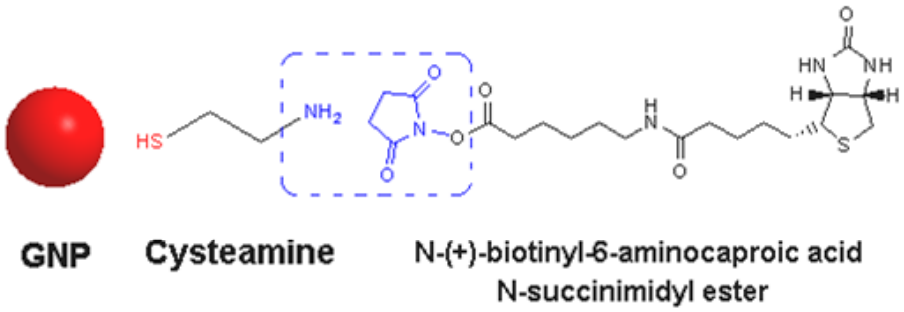

Figure. 6.2 Sythsis of biotin-conjugated GNP.

As expected, the amplitude of the *PA-LINB* signal shown in Figure 6.3a increased significantly after the addition of avidin (all measurements represent values averaged over 50 laser pulses). For comparison, UV/Vis spectra of the GNP probe before and after the addition of avidin were also collected under the same experimental conditions. The broadening and red-shift of the spectra shown in Figure 6.3b can be considered as the evidence of aggregation after the introduction of avidin. Figure 6.3c shows a typical evolution of the *PA-LINB* signal over the time after the addition of avidin. The *PA-LINB* signal raised significantly when aggregation starts and then gradually saturates until the action reaches equilibrium. The details of this experiment can be seen in Ex. 10.

A control test was performed in order to confirm that the increase of the PA signal is indeed due to the aggregation of GNP probes. The binding process of avidin and biotin (not biotin-conjugated GNP) was monitored by our PA setup. As it can be seen in Figure 6.3c (PA control), there was no significant PA signal change. This was expected, as the solutions of avidin, biotin and their reaction product are transparent in the visible spectral range. Hence, it can be assumed that the increase of the PA-LINB signal was not induced by the binding of avidin and biotin.

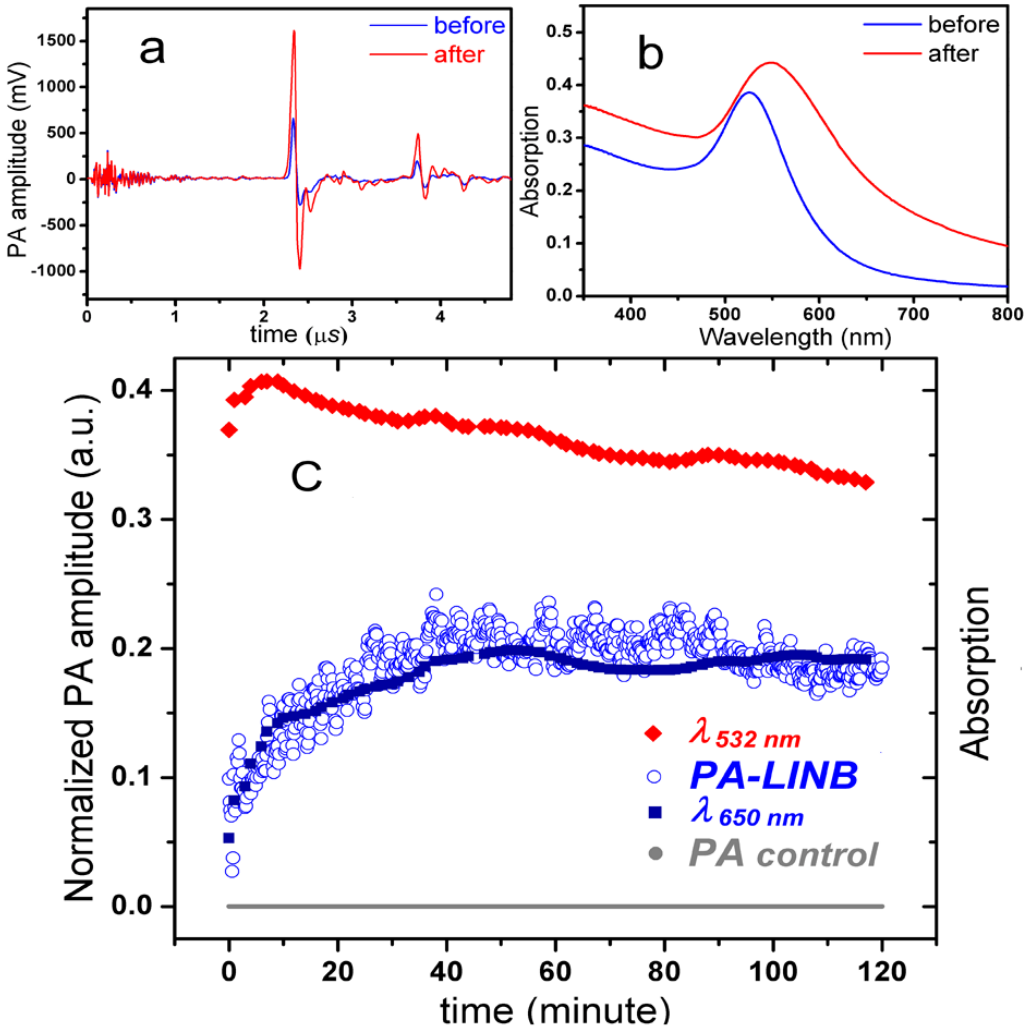

Figure 6.3 PA amplitude (a) and the corresponding UV/Vis absorption spectra (b) before and after the addition of avidin. (c) Time-dependent evolution of the PA amplitude (*PA-LINB*), absorption at 532 nm ($\lambda_{532\ nm}$) and 650 nm ($\lambda_{650\ nm}$) after addition of avidin (biotin-conjugated GNP size: 12.5 nm, concentration: 1.5×10^{12} particles/ml, avidin concentration: 30 nM). For control test, time-dependent evolution of PA amplitude (*PA control*) of mixing 30 nM of biotin and 30 nM avidin was also measured by our PA setup.

Another important observation is the lack of correlation between the *PA-LINB* signal and the absorbance at 532 nm ($\lambda_{532\ nm}$). Due to the gradually red-shift of absorption maximum at ~520 nm, $\lambda_{532\ nm}$ was decreasing constantly after a short increase. This excludes the possibility that the increase of the *PA-LINB* signal was due to the increase of absorbance of the solution at the laser wavelength. On the other hand, the *PA-LINB* signal shows a similarity to $\lambda_{650\ nm}$, and $\lambda_{650\ nm}$ is generally regarded as an indicator of aggregation level of the GNPs. Based on the discussion above, the increase of the *PA-LINB* signal can certainly be related to aggregation.

6.2 Sensitivity

To evaluate the sensitivity of this approach for protein quantification, the *PA-LINB* responses to different avidin concentrations were measured. The results are plotted in Figure 6.4. In this experiment, probes using different diameters of GNP (12.5 and 26.0 nm) were prepared and then diluted to different concentrations to perform the assay. For comparison, the UV/Vis response ratios ($\lambda_{650\ nm}/\lambda_{520\ nm}$) under the same conditions are also shown in Figure 6.4. The ratio of signals after and before aggregation, S/S_0, was calculated as an indicator of the sensitivity. As shown in Figure 6.4, the PA response is significantly more sensitive than a UV/Vis signal. This conclusion is confirmed by both sizes of biotin-conjugated GNP tested in this study. Table 6.1 summarizes the limit of detection (LOD) and the linear working range of the experiment above. The results in the table indicate that PA technique can detect avidin concentrations as low as 0.20 nM. The details of this experiment can be seen in Ex. 11.

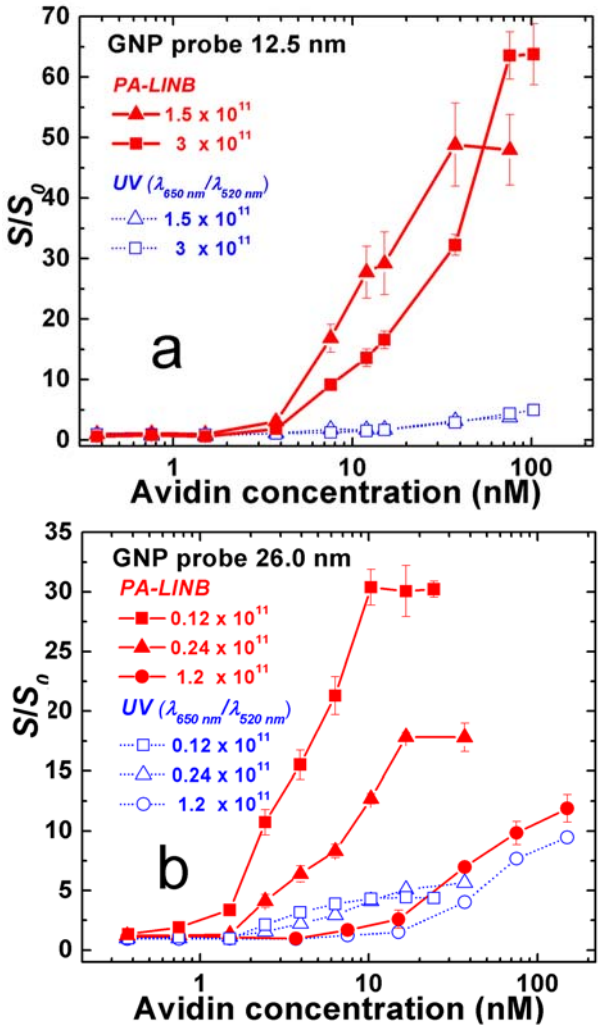

Figure 6.4 Comparison of the experimental results obtained from PA and UV/Vis at different concentrations of avidin. The Biotin-conjugated GNP size is a) 12.5 nm and b) 26 nm; S_0: response of the blank sample. Each of the data points in this figure was averaged from the measurements of consecutive 50 laser pulses.

Table 6.1 Summary of LOD and linear working range. The LOD is estimated according to the standard *3s* rule. The estimation of the probe concentration is described in Experiment Section.

GNP size	Probe concentration (particles/mL)	PA-LINB		UV/Vis	
		Linear range (nM)	LOD (nM)	Linear range (nM)	LOD (nM)
12.5 nm	3×10^{11}	2.5 -70	2.5	12 - 100	12
	1.5×10^{11}	2.0 - 30	2	10 - 30	10
	1.2×10^{11}	7.5 - 160	5	10 - 160	7
26.0 nm	0.24×10^{11}	1.6 - 20	0.5	2 - 16	2
	0.12×10^{11}	1.5 - 10	0.20	4 - 10	4
83.3 nm	0.012×10^{11}	0.4 - 10	0.4	3-10	3

The results shown in table 6.1 indicate that the improvement of the LOD is inversely proportional to the probe concentration. Therefore, a possible way to enhance the LOD is to use a probe concentration as low as our PA setup can detect. We also tried to use larger GNP (83.3 nm) to prepare the probe, because a larger GNP generally generates stronger PA signals [257]. Thus, a lower probe concentration can be used to perform the assay, when using larger GNP sizes. However, all measurements from large GNP probe (83.3 nm) display large standard deviations (data not shown). This effect can be explained by the statistic distribution of the particles in the focal zone of the laser beam, leading to large inhomogeneities for very low particle concentrations. For this reason, the larger probe cannot improve the LOD in this case.

On the other hand, it can been seen from Table 6.1 that the working range decreases with a decreasing probe concentration. A possible explanation for this phenomenon is that there are less binding sites available for avidin in the solution, and therefore the response saturates. However, it should be noted that an excess of avidin will hinder GNP aggregation and causes a decrease of the signal. This is a common problem for this type of cross-linking aggregation-based assay.

The PA technique offers several more advantages compared to UV/Vis spectroscopy in detecting aggregation. *PA-LINB* is an absolute measure of aggregation, which is quite different from UV/Vis spectroscopy, where a ratio of absorbance at different wavelengths is normally used to determine the degree of aggregation. The PA technique is significantly less sensitive to light scattering than UV/Vis spectroscopy [258], which makes it more accurate than UV/Vis spectroscopy in light scattering medium [259]. Hence, it would be possible to introduce scattering materials (magnetic nanoparticles, silica and polystyrene nano/microspheres) into the experiment for further improvement.

6.4 Summary

In summary, a new way to detect GNPs aggregation was described in this chapter, which is based on measuring the change of the PA signal generated by the laser-induced nanobubble. To our knowledge, this work is the first application of this technique in selective molecule quantification. A LOD for avidin was obtained as low as 0.20 nM. In principle, the method presented here could be extended to detect other interesting target s using different GNP probes.

CHAPTER 7

Strong Size-Dependent PA Effect in Aggregation-Based Pb^{2+} Detection

Contents

In CHAPTER 5, a new way of Pb^{2+}quantification based on leaching of GNPs was demonstrated. In this chapter, we present another Pb^{2+} detection method based on monitoring GNPs aggregation by *PA-LINB*.

7.1 Mechanism of Detecting Pb^{2+} Based on PA-LINB

The method is based on the increase of the *PA-LINB* signal caused by the aggregation of glutathione-conjugated GNPs (GSH-GNPs) in the presence of Pb^{2+} ions. Glutathione (GSH) plays an important role in shielding intracellular components from oxidative damage and in detoxifying of heavy metal ions in organisms [260]. Due to the presence of the mercapto group (-SH), GSH can easily bind to the GNP via Au-S bond to form the GSH-GNPs probe. In addition, GSH molecule contains two chelating ligands (Figure 7.1), which show a high affinity to Pb^{2+}. Hence, in the presence of Pb^{2+}, several GSH-GNPs conjugate with one Pb^{2+}, and nanoparticles aggregates are thereby produced [261-262]. Accordingly, the aggregation will yield a significant shift and broaden in the SPB of GNPs, which can be detected by an UV/Vis spectrometer. This mechanism has been clearly described in previous reports [263].

In the previous chapter, it has been proven that *PA-LINB* is a more sensitive tool than UV/Vis spectrometer for detecting aggregation. Hence, the aggregation of GSH-GNPs in the presence of Pb^{2+} can also be monitored by *PA-LINB* (see Figure 7.2). According to strong size-dependent PA effect, the aggregation of GSH-GNPs can cause a raise in *PA-LINB* signal, and this raise can be used for Pb^{2+} quantification in the solution. In this chapter, we tried to realize this idea.

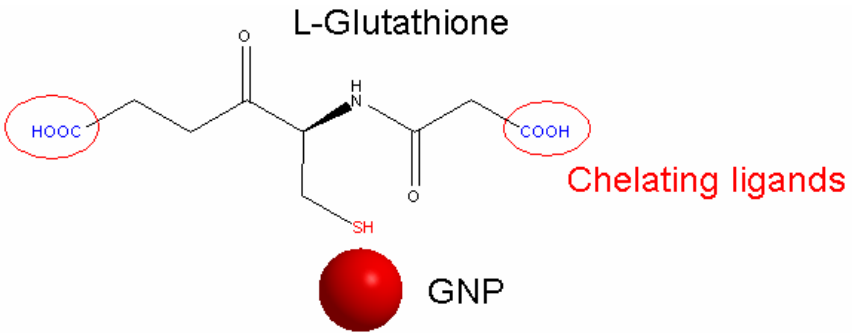

Figure 7.1 Structure of GSH-conjugated GNP

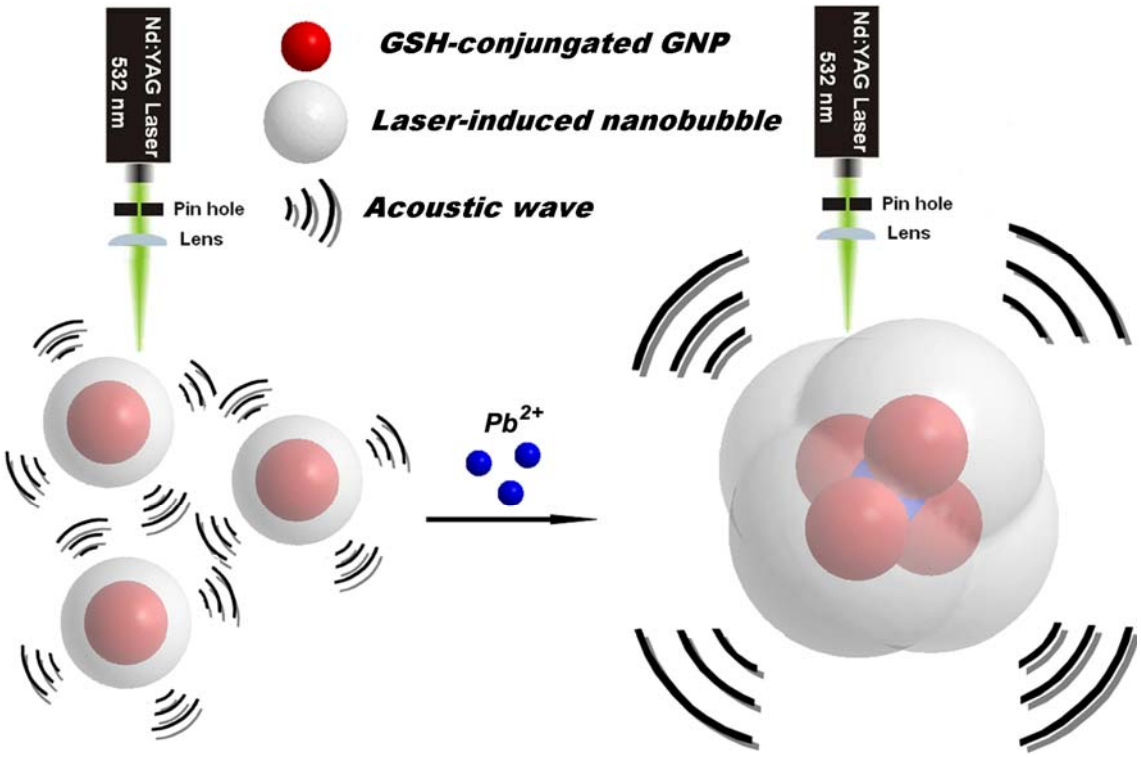

Figure 7.2 Schematic illustration of Pb^{2+}-triggered GNPs aggregation enhancing the amplitude of *PA-LINB* for sensitive Pb^{2+} detection.

7.2 Feasibility

The aggregation of GSH-GNPs in the presence of Pb^{2+} can be confirmed by the corresponding UV/Vis spectra. As shown in Figure 7.3 (left), the broadening and red-shift of the spectra was observed, when GSH-GNPs were mixed with the Pb^{2+} (final concentration 0, 1, 5, 20 μM). This fact can be viewed as the evidence of aggregation after the introduction of Pb^{2+}, since the broadening and red-shift of the spectra is caused by the coupling of surface plasmons of adjacent nanoparticles in aggregate. At a high Pb^{2+} concentration level, a color change of GSH-GNPs suspension can even be observed by naked eyes, as plotted in Figure 7.5 (right). Details of this experiment can be seen in Ex. 12.

For comparison, the corresponding *PA-LINB* signals under the same conditions were recorded. As plotted in Figure 7.4, the amplitude of *PA-LINB* increased significantly when GSH-GNPs were mixed with Pb^{2+}. According to the results in the last chapter, the *PA-LINB* will witness a great increase when GNP aggregation occurs. This assumption showed a good accordance with the phenomena observed above. We also noted that the increase of the *PA-LINB* signal in Figure 7.4 is related to the concentration of Pb^{2+}. The amplitude of PA-LINB is significant higher, when the Pb^{2+} concentration is higher. Clearly, with higher Pb^{2+} concentration, the amount or size of resulting aggregates increases, the corresponding *PA-LINB* signal is larger. Based on the facts above, the *PA-LINB* can be used as an index to quantify Pb^{2+} in aqueous solution via this approach.

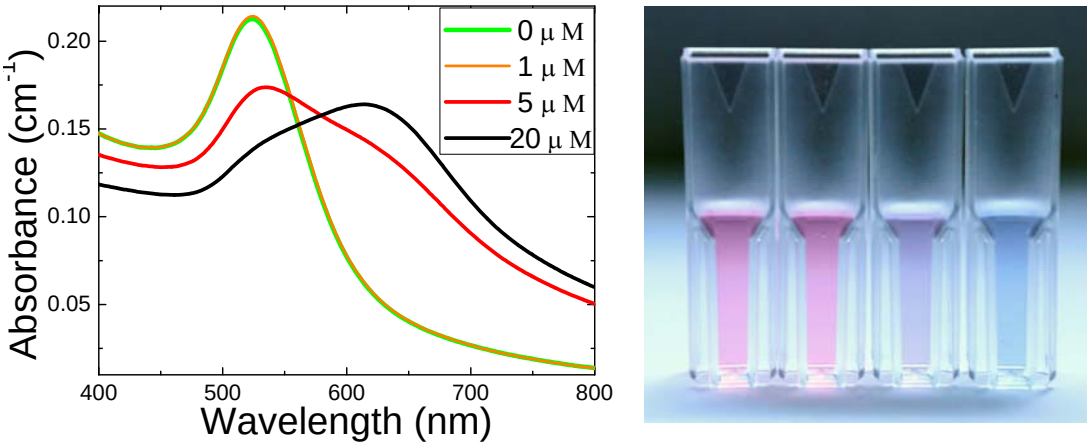

Figure 7.3 The UV/Vis spectra (left) and images (right) after GSH-GNPs suspensions mixed with various concentrations of Pb^{2+} (0, 1, 5, 20 μM).

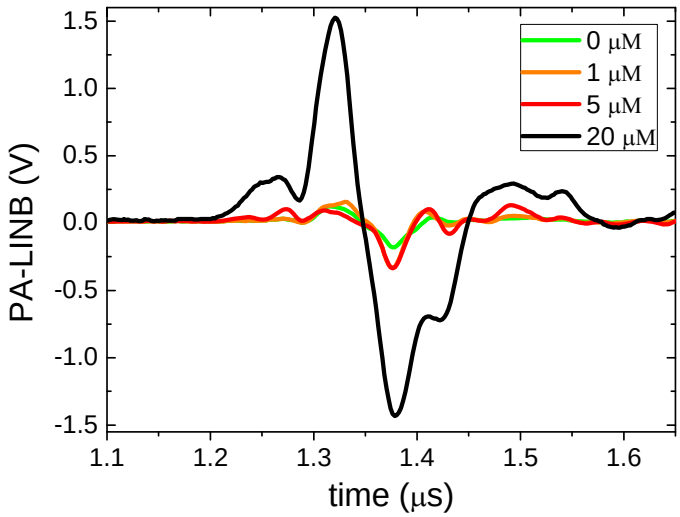

Figure 7.4 The PA signal after GSH-GNPs suspensions mixed with various concentrations of Pb^{2+} (0, 1, 5, 20 μM). The time delay (t_a) is the time needed for propagation of the generated acoustic pulse propagates to the detector, which depends on the position of the detector and the laser beam, and the sound speed in the corresponding medium.

7.3 Optimizing the Experimental Conditions

It is widely known that pH value and ionic strength of the matrix have great influence on the aggregation process of GNPs. For example, during the preparation of GSH-GNPs, we found GSH-GNPs are unstable in acidic conditions. The aggregation of GNPs immediately occurred when the GSH solution (acidic) was added. Hence, in order to

prevent GNPs from aggregation, the pH value of gold colloids was adjusted to ~10 before addition of GSH solution (see Experiment Section).

The concentration of salt also has a major influence on the aggregation of GSH-GNPs. The GSH contains two free –COOH groups and one $–NH_2$ group, which provide a hydrophilic interface and can protect the GSH-GNPs from aggregation. The results shown in Figure 7.5 prove that GSH-GNPs are stable even in a solution with high ionic strength (in 0.1 M NaCl solution). However, the repulsion effect of GSH is so strong that it even prevents GSH-GNPs from aggregation in the presence of Pb^{2+}. Figure 7.5 also shows the UV/Vis response of GSH-GNPs to various salt concentrations in the presence of the same concentration of Pb^{2+} (10 µM). Details can be seen in Ex. 13. The ratio of the absorbance values ($\lambda_{650\ nm}/\lambda_{520\ nm}$) was used to express the molar ratio of aggregated and non-aggregated GSH-GNPs, which can be seen as an index of aggregation level. As can been seen in Fig 7.5, no aggregation was observed when final salt concentration was below 0.06 M. When salt concentration is above 0.06 M, the GSH-GNP aggregated immediately after the addition of Pb^{2+} and reached equilibrium in about 20 min.

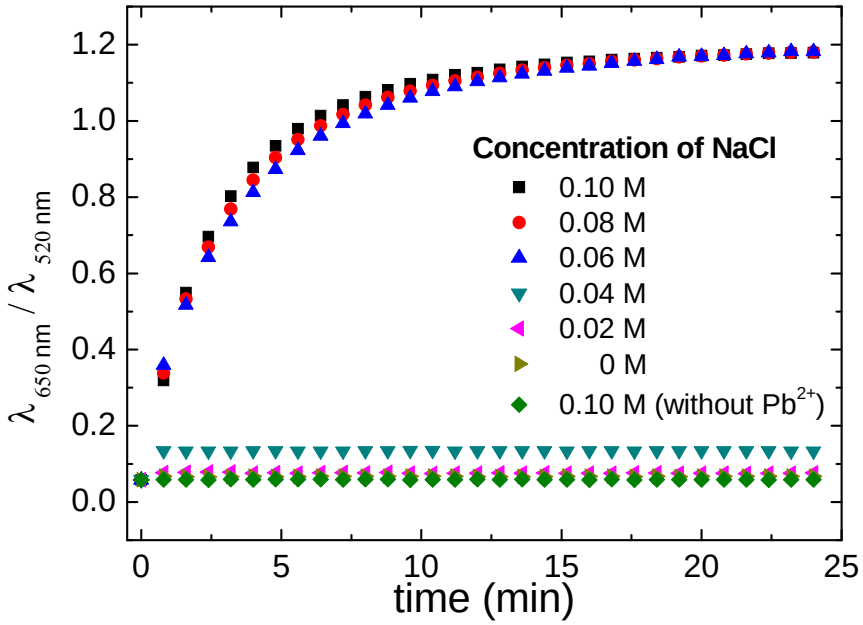

Figure 7.5 UV/Vis responses of GSH-GNPs to 10 µM of Pb^{2+} in various NaCl concentrations (0 – 0.10 M), and the UV/Vis spectrum of GSH-GNPs in 0.10 M of NaCl solution (without of Pb^{2+}).

7.4 Selectivity

To evaluate the selectivity of this assay, it was challenged with other environmentally relevant metal ions including Ba^{2+}, Ca^{2+}, Cd^{2+}, Co^{2+}, Cr^{3+}, Cu^{2+}, Fe^{2+}, Fe^{3}, Mg^{2+}, Mn^{2+}, Ni^{2+}, and Zn^{2+} ions. In a typical experiment, one of these metal ions was added to the GSH-GNPs in the presence of 0.1 M NaCl. After 20 min, the mixtures were measured by the PA setup. The details of this experiment can be seen in Ex. 14. As illustrated in Figure 7.6, only the Pb^{2+} sample showed a significant increase in the *PA-LINB* amplitude compared to the blank (pure water). No obvious *PA-LINB* amplitude increase was found for other metal ions.

The aggregation of GSH-GNPs was caused by the coordination between Pb^{2+} and –COOH of GSH. In theory, many other ions, i.e. Cu^{2+}, Cd^{2+}, Fe^{3+}, etc., share the same coordination effect with Pb^{2+}. Thus it is hard to explain the selective response of the GSH-GNPs towards Pb^{2+}. Su and co-worker believed that this selectivity partially is due to the fact that the aggregation rates of GSH-GNPs to Pb^{2+} is relative fast in comparison to other ions [263]. However, the exact mechanism still requires further investigation.

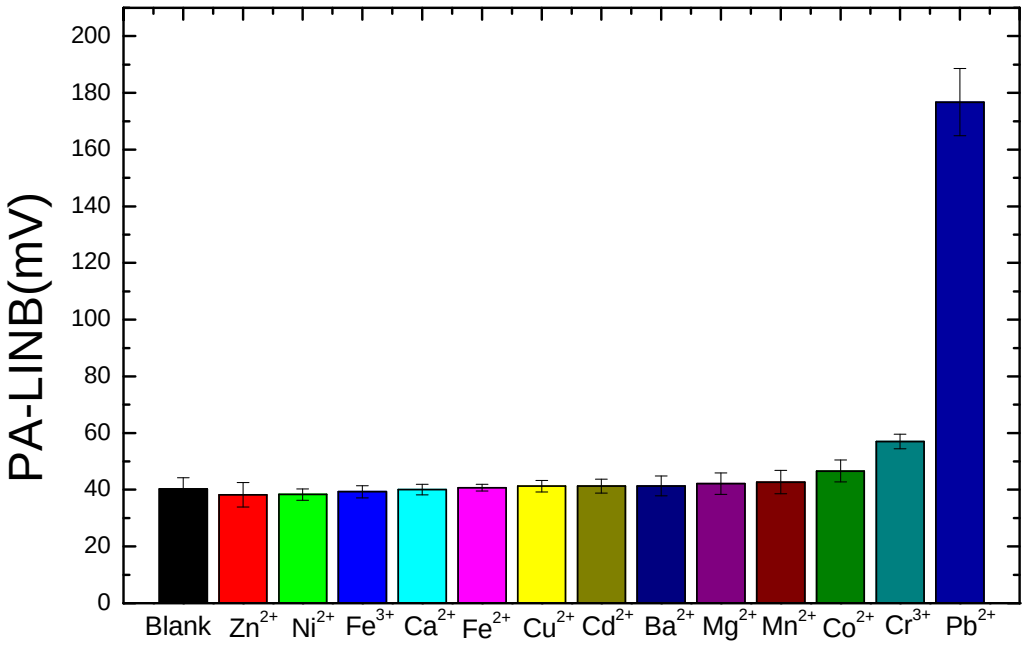

Figure 7.6 The PA responses after GSH-GNP mixed with various ions (Ba^{2+}, Ca^{2+}, Cd^{2+}, Co^{2+}, Cr^{3+}, Cu^{2+}, Fe^{2+}, Fe^{3}, Mg^{2+}, Mn^{2+}, Ni^{2+} and Zn^{2+}; final concentration 2 μM).

7.5 Sensitivity of the Assay

To evaluate the sensitivity of this approach for Pb^{2+} quantification, the *PA-LINB* responses to different Pb^{2+} concentrations (0 ~ 8 μM) were measured (see Ex. 15). The results are plotted in Figure 7.7. A linear relationship between *PA-LINB* and the Pb^{2+} concentration was observed from 42 to 1000 nM (R^2 = 0.9969, n = 6) (Figure 7.8). The results indicate that the PA technique can detect Pb^{2+} concentrations as low as 42 nM, which is below the maximum contamination level (75 nM) for lead in drinking water (defined by the U.S. Environmental Protection Agency).

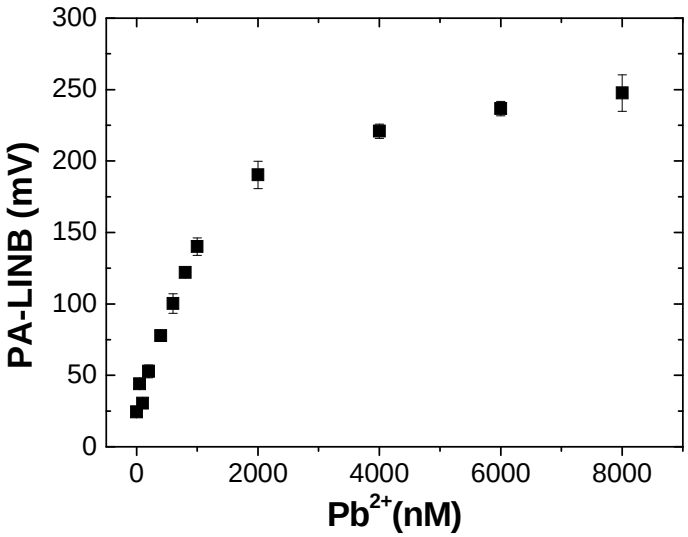

Figure 7.7 PA responses of GSH-GNP to various Pb^{2+} (0 ~ 8 μM)

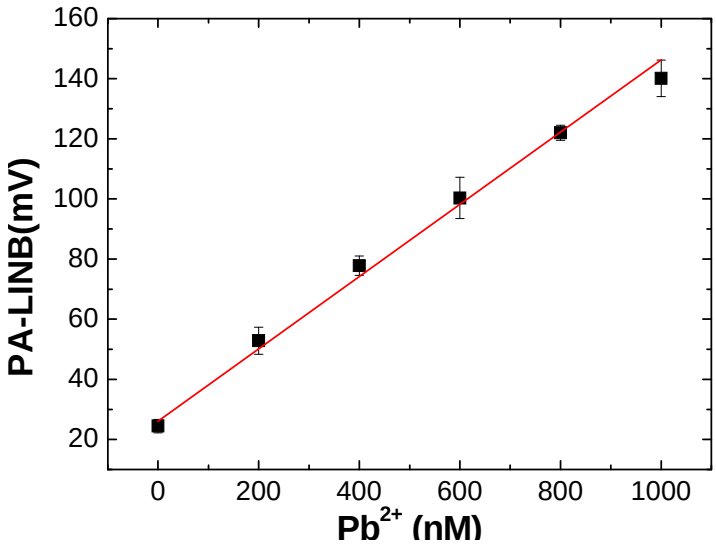

Figure 7.8 Calibration curve of the Assay.

7.6 Summary

A simple and rapid detection method for Pb^{2+} based on aggregation of GSH-GNPs probe monitoring by *PA-LINB* has been developed. A LOD of 42 nM was achieved. The linear working range of the calibration curve ranges from 42 to 1000 nM.

PART B

SERS-based Sensing

CHAPTER 8

Attempts of Direct SERS Monitoring of Immunological Recognition

Contents

8.1 Introduction of Label-Free SERS Detection

Another interesting optical property of GNPs is the surface-enhanced effect. SERS holds vast potential in biological and chemical sensing. With an enhancement factor of 10^{12}, SERS enables measurement of weak Raman scattering of single molecules [264-265]. In addition to the high sensitivity, SERS also offers high detection selectivity, since each molecule has a unique Raman spectrum, also known as "fingerprint" spectrum. SERS is a surface-sensitive technique [102]. The molecule needs to be directly absorbed on or very close to the metal surface to experience a significant enhancement of Raman scattering. Hence, another advantage of SERS is it enables detecting a specific target in a complex samples without physical separation of interferents, by controlling the surface chemistry around the metal surface [266-271].

An interesting sensing mechanism is the so-called label-free SERS detection. By incorporating a specific chemical moiety on the metal surface, the analytes can be captured on the metal surface. Thus, the analyte can be identified by its fingerprint spectrum and meanwhile quantified based on the intensities of certain specific bands. This sensing principle is straightforward, and eliminates the need for labels. In this chapter, we attempted to apply this sensing mechanism to detect the antigen-antibody binding.

8.2 Possible Detection Schemes

In this section, several possible label-free SERS detection schemes were tested. Benzo[a]pyrene (B[a]P) and anti-benzo[a]pyrene antibody were chosen as model to realize this scheme. B[a]P is a five-ring polycyclic aromatic hydrocarbon, whose structure is shown in Figure 8.1. The maximum tolerable limit of B[a]P in drinking water was set to 10 ng/L by the European Commission (Council Directive 98/83/EC). A vast number of studies have demonstrated the possible links between B[a]P and cancer [272-274]. Hence, the control and monitoring of B[a]P in drinking water is of great importance.

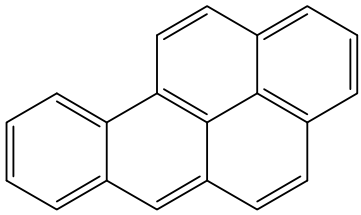

Figure 8.1 Molecular structure of benzo[a]pyrene.

As our first attempt, the surface of GNP was modified with anti-B[a]P antibody as SERS probe (see Experimental Section), and thus it is capable of capturing and separating B[a]P from the sample matrix. In principle, it is possible to detect those captured B[a]P molecules by SERS, due to existence of the surface-enhanced effect on the GNP surface. This detection scheme is plotted in Figure 8.2.

However, no SERS signal of B[a]P was found after the addition of B[a]P to a SERS probe (see the *Mixture* in Figure 8.3). The observed spectrum is significantly different from the SERS spectrum of B[a]P，which is also shown in Figure 8.3 (obtained by mixing B[a]P with silver nanoparticles, see Ex. 16). Neither is there any detectable change in the SERS spectrum after the addition of B[a]P to SERS probe.

One possible explanation is that, as we mentioned above, SERS is a surface-sensitive technique. The analyte needs to be directly absorbed on or very close to a metal surface to experience significant enhancement of SERS [275]. It has been proven that the SERS

intensity decreased by a factor of 10 when the analyte was 2.8 nm away from the surface [105-106]. Further increase of the distance to 20 nm will cause the SERS intensity dropping to one hundredth of the initial intensity [107]. In our case, the B[a]P molecules were separated from the surface by antibodies and as a result, the enhancement effect on these sites are comparably small.

Another possible explanation is that the enhancement effect of single isolated particles is relative small. The enormous enhancement factors of SERS ($10^8 \sim 10^{12}$) were often produced by nanoparticle aggregates [264-265]. Accordingly, this may help to explain that no SERS signal from B[a]P was observed after addition of B[a]P to the probes.

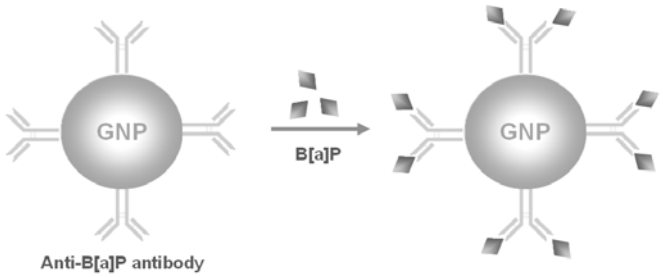

Figure 8.2 Scheme of label-free detection of B[a]P by SERS.

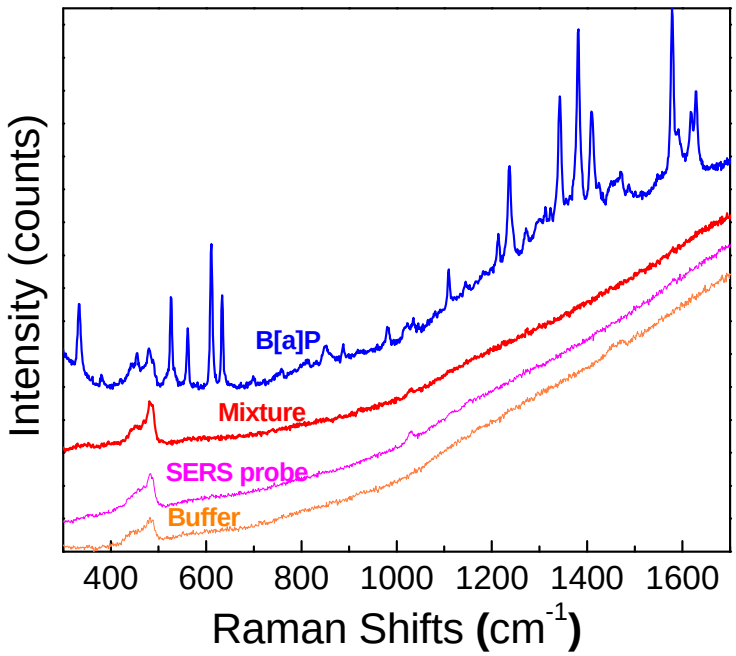

Figure 8.3 SERS spectra of buffer, SERS probe, the mixture of SERS probe and B[a]P. The SERS spectrum of B[a]P was obtained by mixing Ag NPs with B[a]P.

Addressing this problem, we introduced Ag NP aggregates to improve the system. Hereby, after the binding of B[a]P to SERS probe, Ag NPs were added accompanied by NaCl to form nanoparticle aggregates, as shown in Figure 8.4 (see Ex. 17). Theoretically, this procedure also increases the probability of B[a]P being absorbed direct on the aggregates surface. Thus, B[a]P can experience an enhancement effect from the aggregates. Yet, we still could not detect any SERS signal from B[a]P after the addition of Ag NP aggregates (data not shown).

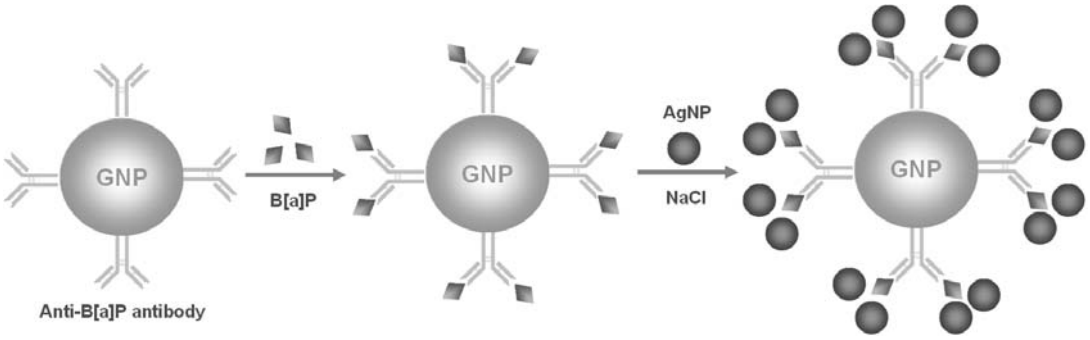

Figure 8.4 Scheme of label–free SERS detection of B[a]P by Ag NPs aggregates.

It is widely known that nanoparticle aggregates can provide enormous SERS enhancement due to the formation of "hot spots" during the aggregation. Actually, almost all the SERS signal is produced by analytes in these "hot spots", since the rest of the surface of aggregates is comparatively SERS inactive [276-278]. But these "hot spots" are well confined within the small gabs between adjacent nanoparticles. However, in our case, it is very hard for the relatively big B[a]P-antibody complex to enter the small gab. Thus, the captured B[a]P cannot share the enormous enhancement effect in the "hot spots". A counter example can be found in the last experiments. When free B[a]P was mixed with Ag NP aggregates, an intensive SERS signal was observed (Figure 8.3), because it is much easier for small molecules to enter the "hot spots". These facts may help to explain that the introduction of Ag NP aggregates does not improve the detection sensitivity of this approach.

Furthermore, there is a drawback of the above mentioned approach. Because the surface of the aggregates is directly exposed to the environment, the detection can be easily

interfered by the SERS signal of interfering species in the matrix. Accordingly, we ceased to invest more time in this approach.

Realizing the NP aggregates were ineffective in generating SERS enhancement in the above mentioned approach, we used another technique. After addition of B[a]P, the SERS probe was immediately treated with a Ag enhancement solution (Figure 8.4) and a silver layer was deposited on GNP (see Ex. 17). This silver amplification procedure is widely used for SERS [147]. After the amplification, some changes in the spectrum were observed. But this spectrum is significant different form the spectrum of B[a]P, as shown in Figure 8.5.

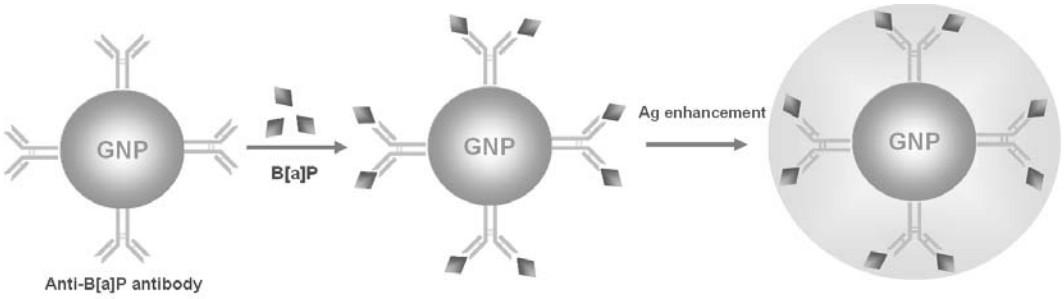

Figure 8.4 Scheme of SERS detection of B[a]P via silver enhancement.

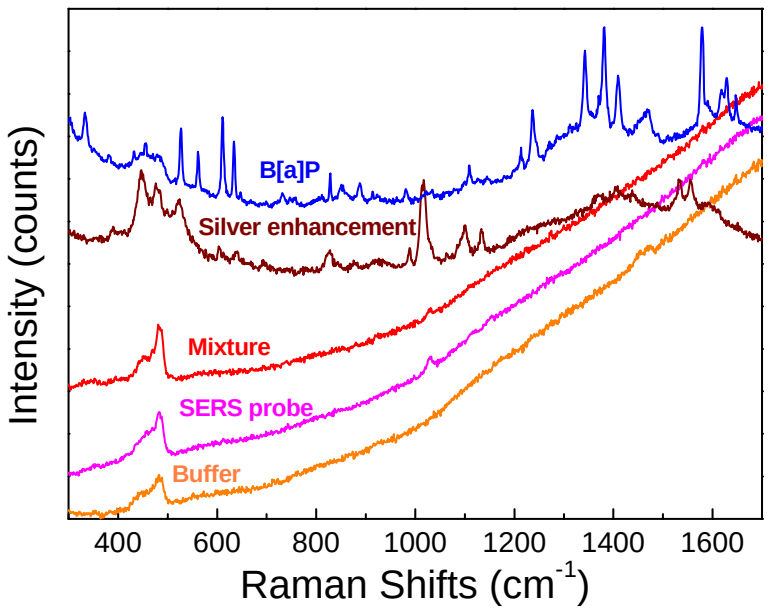

Figure 8.4 SERS spectra of buffer, SERS probe, the mixture of SERS probe and B[a]P, and the mixture after silver enhancement. The SERS spectrum of B[a]P was obtained by mixing silver nanoparticles with B[a]P in the presence of NaCl.

A reasonable explanation is the B[a]P-antibody complex may be unstable in the strong acidic Ag enhancement solution (pH 3.5 ~ 4). Thus, the B[a]P was detached from the SERS probe. Meanwhile, some species in the matrix were absorbed on the newly formed silver surface. Hence, we can observe some change in the spectra, but no SERS signal of B[a]P.

8.3 Summary

The ideas of direct motoring the antigen-antibody binding by SERS were tested in this chapter. However, these attempts proved to be unsuccessful. Despite the unsatisfying results, we can still gain useful experience and the direction for future work.

CHAPTER 9

Indirect Monitoring of Immunological Recognition based on Core-Shell SERS Tags

Contents

In this chapter, we present an indirect way to monitor immunological recognition based on SERS tags. SERS tag is a labeled nanoparticles, which includes strong SERS enhancement in the combination of Raman active dyes with metallic nanoparticles. The majority of SERS tags are designed in core-shell geometry, due to their significantly higher stability to environmental conditions. The main disadvantage of core-shell tags up to now was the time-consuming and complex preparation procedures. In this chapter, a rapid and straightforward method for the synthesis of core-shell SERS tags is described. Hence, the stability of the SERS tags was evaluated under extreme pH values, high ion strength, etc. Finally, the SERS tags are functionalized with anti-*Salmonell*a antibodies as a model to present a potential application of tags in biological sensing.

9.1 Introduction of SERS Tags

SERS exhibits a vast potential as a highly sensitive and selective tool for the detection of biological or chemical analytes. The fabrication of the SERS substrates or SERS tags is generally considered one of the most critical aspects of a SERS experiment. As one of the two pillars of a SERS experiment, the SERS tag is a labeled nanoparticle, usually consisting of gold or silver. Combined with resonant Raman reporter molecules, SERS tags can provide $10^6 \sim 10^{14}$-fold enhancement of the Raman scattering intensity, which

can even be sufficient for single-molecule detection [264, 266, 279]. Compared to other tags, such as plasmon-resonant particles, quantum dots, and fluorescent dyes, an unique advantage of SERS tags is that they are highly specific. Hence, a wide range of different SERS tags can be used simultaneously in single detection systems.

Most SERS tags developed recently are based on two principal approaches. One is the direct attachment of Raman reporter molecules and recognition elements on silver or gold nanoparticles. The first works were presented by Cao et al. [147]. The SERS tags they prepared enabled multiplex DNA and RNA detection. One limitation of this approach is the instability of the SERS tags caused by the direct exposure of tag surface to the environment.

An improved approach is to cover the surface of nanoparticles with a layer of silica or polymers, in which the Raman reporter molecules are embedded (so-called core-shell SERS tags). The first attempt to achieve this was made by Doering et al. and Mulvaney et al. [151, 280-281]. The silica shells protect the SERS tags from aggregation and facilitate functionalization. Even some more complex multilayer core-shell SERS tags have been developed recently through a layer-by-layer deposition procedure [149-151]. Generally, this procedure can improve the stability and other optical properties of SERS tags. However, this improvement comes at the cost of preparation time: obviously, the more complex the structure is, the longer the preparation time it needs (usually days or more), the more chemicals it consumes, and the harder the process is to handle [281]. Especially cumbersome, a vitrophilic (“affine to silica”) pretreatment needs to be performed usually on silver or gold nanoparticles to make their surfaces affine to silica. Merely this process can take days; so, a more straightforward and simpler synthesis method is highly desired.

9.2 Synthesis and Characterization of Core-Shell SERS tags

9.2.1 Synthesis

Here, a fast, daily use synthesis method of core-shell SERS tags is described. The whole process takes less than 2h, and there is no need for vitrophilic pretreatment. Both Ag and Au nanoparticles can be applied to fabricate the tags. Moreover, the choice of Raman reporter molecules is broad. Organic dyes with an isothiocyanate (-N=C=S) group or with multiple sulfur atoms can be employed, since they bind strongly on the core particles with silica encapsulation. The core particles can be directly coated by a sol-gel procedure after the absorption of the reporter molecules. Although the initial purpose of this coating method was to cover GNPs with conformal silica shells [282], we found it also effective in coating Ag NPs. The coating method involves two steps: the generation of silica sols with base-catalyzed hydrolysis of tetraethyl orthosilicate (TEOS), followed by nucleation and condensation of these sols onto the surface of tagged core particles.

Usually, Ag and Au nanoparticles have little affinity to silica, since they cannot form a passive oxide film in solution and the stabilizers absorbed on their surface also renders vitreophobic [283]. Thus, a vitrophilic pretreatment is often required in coating their surface with silica shells [280-281]. First the stabilizers must be removed, either by dialysis or by an ion-exchange resin. Then the surface is modified by amine- or mercapto-terminated siloxane to make it vitrophilic. This pretreatment certainly increases the preparation time. Moreover, the experimental conditions need to be carefully controlled to avoid aggregation, since the nanoparticles become less stable after removal of the stabilizers.

To address this problem, we managed to skip the vitrophilic pretreatment by directly coating the Ag NPs after attaching the Raman reporter molecules. As shown in Figure 9.1, Raman reporter molecules are first added to Ag NPs. After the reporters were absorbed onto the colloidal surface, it is transferred into 2-propanol to start the coating process.

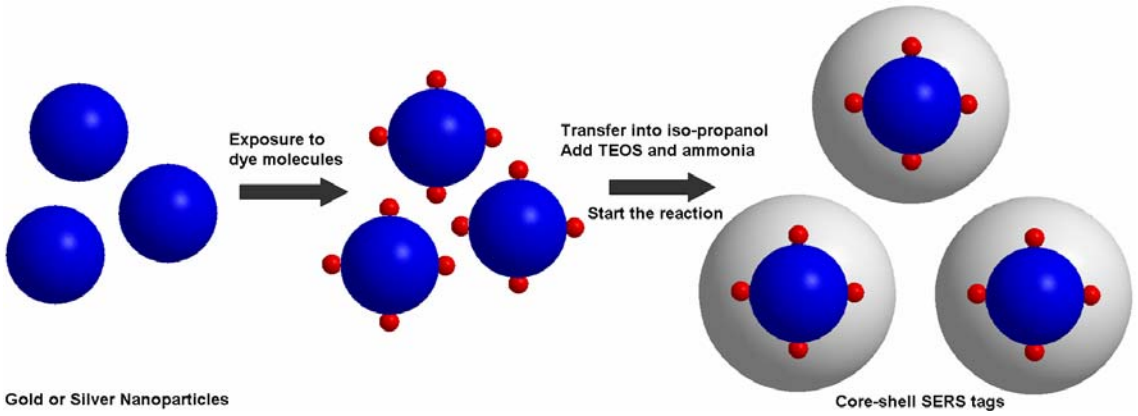

Figure 9.1 Schematic illustration of the preparation of the core-shell SERS tags.

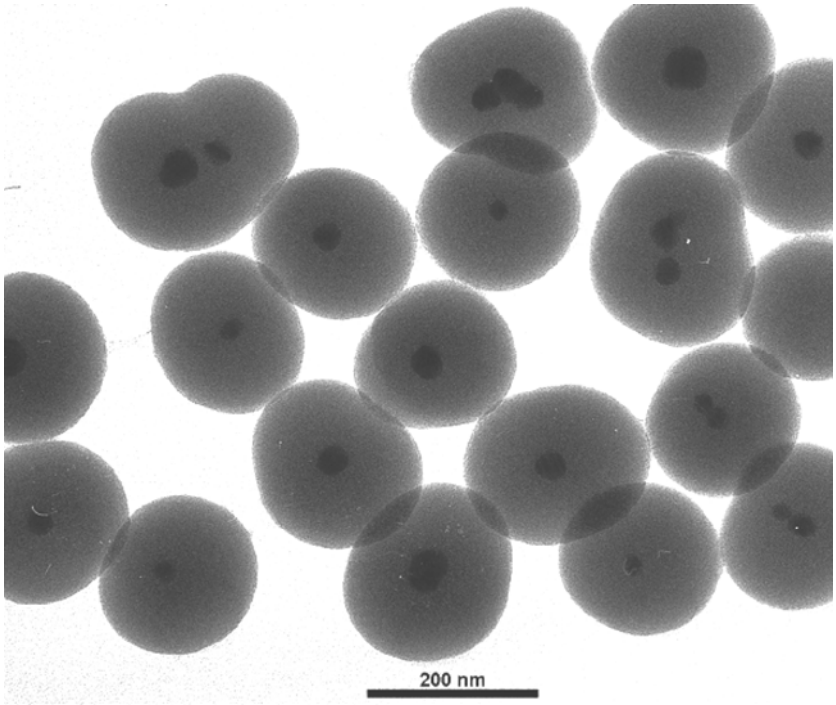

Figure 9.2 Transmission electron micrograph of the SERS tags (Ag).

The coating method we used is a sol-gel process which has been proven to be capable of coating a variety of NPs, such as gold sphere nanoparticles, silver nanowires, superparamagnetic Fe_3O_4, and others [282, 284]. It is also very effective in fabrication of core-shell SERS tags. In general, the silica shell is formed in situ by the base-catalyzed hydrolysis of TEOS, and the following deposition of silica onto the surface of Ag NPs, while the ammonia is added as a catalyst to speed up the process. Figure 9.2 shows a typical transmission electron microscopy (TEM) image of SERS tags synthesized by this approach. After the coating process, these core-shell tags are well-dispersed spherical nanoparticles. Au NPs can also be used to fabricate SERS tags, following a similar procedure. The details are shown in the Experimental Section.

Each molecule has a unique fingerprint Raman spectrum, since different functional groups are specified by different vibrational energies. As a result, the possible choice of Raman reporter molecules is vast. However, in our case, only molecules that strongly bind to Ag nanoparticles can be used as Raman reporter molecules. The experimental results show that organic dyes with an isothiocyanate (-N=C=S) group, such as tetramethylrhodamine-5-isothiocyanate (TRITC) and fluorescein 5(6)-isothiocyanate (FITC), or with multiple sulfur atoms (5, 5'-dithiobis(2-nitrobenzoic acid, DTNB) could be encapsulated in the silica shell (Figure 9.3). The -N=C=S or sulfur atoms yield a sulfur-Ag bond that is stable during the whole coating process. We also tried with Rhodamine B (without –N=C=S group and multiple sulfur atoms), but no Raman signal could be detected after silica coating (data not shown). Small organic molecules with a -SH group or $-NH_2$ group also strongly bind to Ag nanoparticles, such as thiophenol and aminobenzoic acid. The main reason we do not prefer those small molecules is that, according to previous reports [265, 285-286], resonance Raman can provide an additional 2 - 3 orders of magnitude of enhancement compared to SERS alone, but it is nearly impossible to achieve resonance Raman enhancement at a visible excitation range for those small molecules.

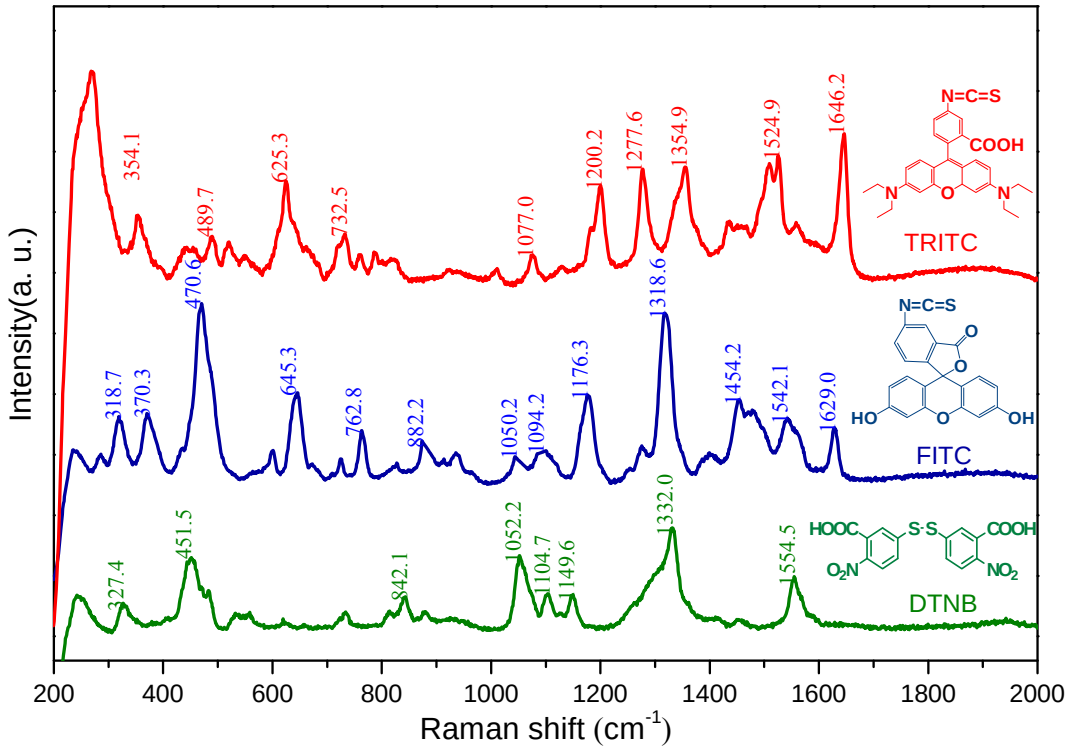

Figure 9.3 Typical Raman spectra of three SERS tags and the chemical structures of three Raman reporter molecules, TRITC, FITC and DTNB (λ_{ex} = 633 nm, accumulation time 10 s, objective 20×).

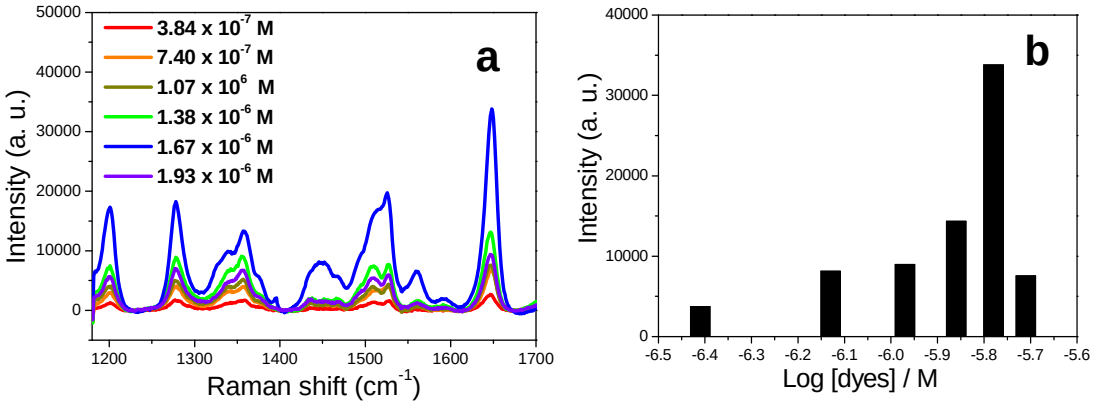

Figure 9.4 (a) Raman spectra of the SERS tags prepared under six TRITC concentrations (3.84×10^{-7}, 7.40×10^{-7}, 1.07×10^{-6}, 1.38×10^{-7}, 1.67×10^{-7}, and 1.93×10^{-7} M). (b) Peak intensities at 1646 cm^{-1} (λ_{ex} = 633 nm, accumulation time 10 s, objective 20×).

The influence of the concentration of the Raman reporters was also investigated. Figure 9.4a shows the SERS spectra of SERS tags prepared with different concentrations of TRITC. From 3.84×10^{-7} to 1.67×10^{-6} M, the signal of the SERS tags increases with the dye concentration (see Figure 9.4b). Especially when the concentration increases from 1.38×10^{-6} to 1.67×10^{-6} M, the signal increases dramatically: for instance, the peak intensity at 1646 cm^{-1} jumps from 14, 352 counts to 33, 796 counts. This increase could be explained by the increasing number of dye molecules which can be embedded into the silica. An explanation for the sudden drop of signal at the concentration 1.93×10^{-6} M is less obvious. According to previous reports [287], excess dye molecules could hinder the TEOS accessing the surface of the nanoparticles and hence result in failing silica encapsulation. Other researchers attributed these intensity discontinuities to fluctuations of molecule-surface charge transfer interactions [288]. The exact explanation of this phenomenon requires further investigation.

9.2.2 Stability of the Tags

High stability is a special advantage of core-shell SERS tags. Firstly, the silica shell renders the tags amenable to use in a variety of solvents (see Ex. 19). Figure 9.5a shows that the core-shell SERS tag maintains its stability in NaCl, NaOH, HCl, ethanol, THF, and DMF. In contrast, the bare colloidal Ag, as a model of a naked SERS tag, rapidly agglomerates when transferred from H_2O into NaCl, HCl, THF, or ethanol (see Figure 9.5b). It is only stable in NaOH and DMF, where the nanoparticles can maintain enough negative charge on their surface. Secondly, the silica shell isolates the core particles from surrounding environment. Thus, it eliminates the influences of the possible disturbances presented in the environment. A proof has been shown in Figure 9.6. When concentrated crystal violet (10^{-5} M) is added into the tag solution, the Raman spectrum remains the same and no signal from crystal violet is observed (see Ex. 20).

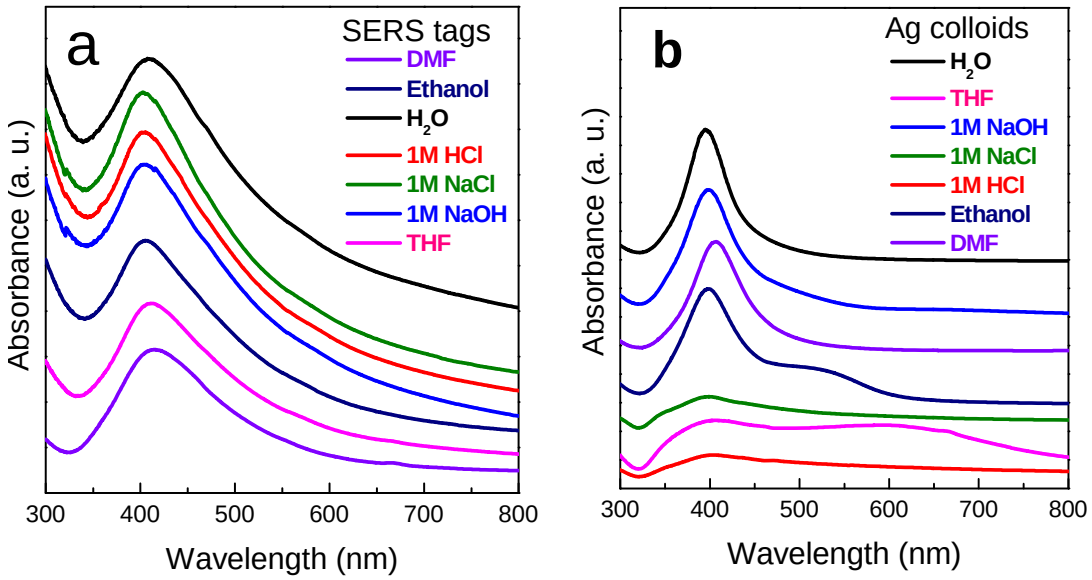

Figure 9.5 Stability comparisons between silica-coated SERS tags (a) and uncoated silver nanoparticles (b) (as a model for naked SERS tags) in different solutions. The lack of changes in the UV/Vis spectra indicates a high degree of stability of the tags.

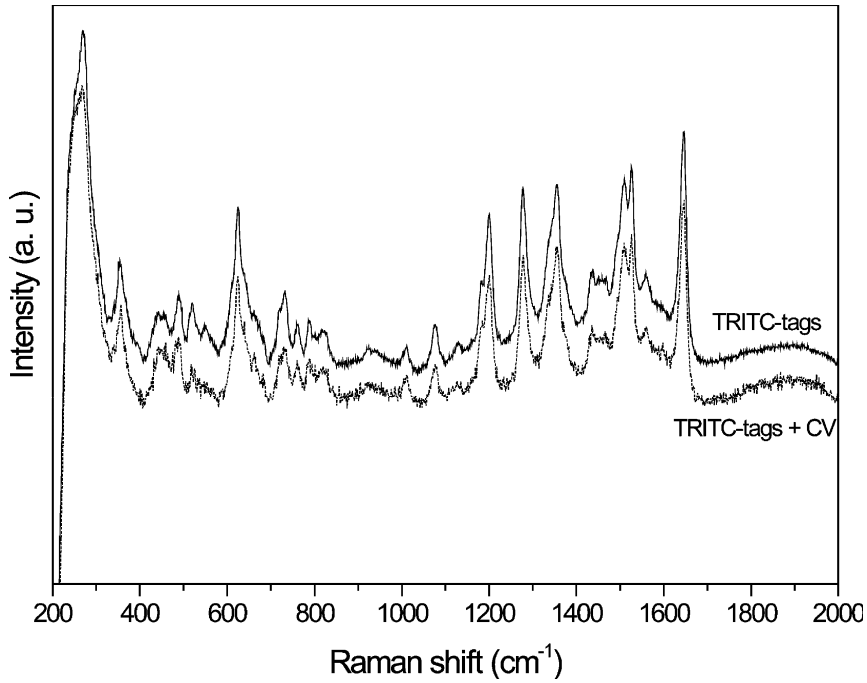

Figure 9.6 Raman spectra obtained with and without the addition 10^{-5} M crystal violet presented in the solution (λ_{ex} = 633 nm, accumulation time 10 s, objective 20×).

9.3 Application

The silica shell offers an additional advantage: it is easily functionalized. After amino groups or carboxylic groups are introduced onto the surface of the SERS tags, it can be bound to proteins, peptides, various nucleotides, or others. As shown in Figure 9.6, the primary amino groups were introduced onto the SERS tags' surface by a reaction with APTMS, subsequently conjugated with pAB anti-*Salmonell*a antibody. In a typical sandwich immunoassay, anti-*Salmonell*a antibody was chosen as a model to investigate the potential of our SERS tags in bioimaging (see experimental section). The right-hand side of Figure 9.8 shows a photographic image after the modified tags (TRITC) bound to *Salmonell*a bacteria, while the left side represents a SERS intensity map of the same surface region, based on the area of the peak at 1646 cm^{-1} (see Ex. 21)

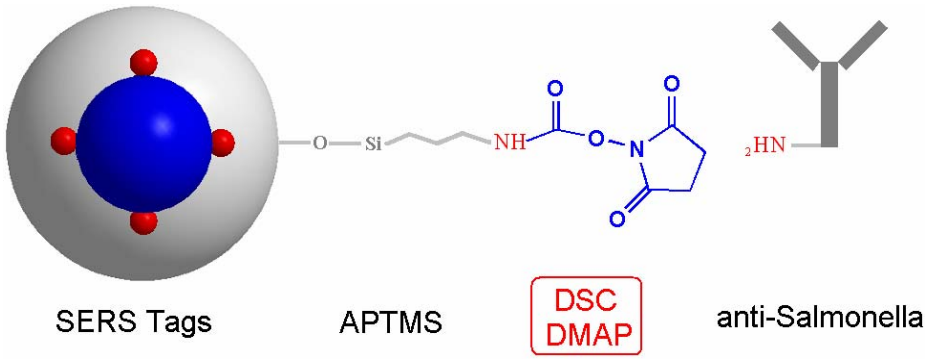

Figure 9.6 Modification of SERS tags.

In most parts of the map, the occurrences are similarly distributed with some exceptions, because the resolution of SERS intensity maps is confined by the objective and laser wavelength to comparable low level (1 - 2 µm). Typical SERS spectra of different spots of the map, labeled with green dots in the photographic image, can be seen in the inset in Figure 9.8 on the left. The distinct differences between the SERS spectra from bacteria and from the background indicate the high sensitivity of our detection model and underline the great potential of our SERS tags.

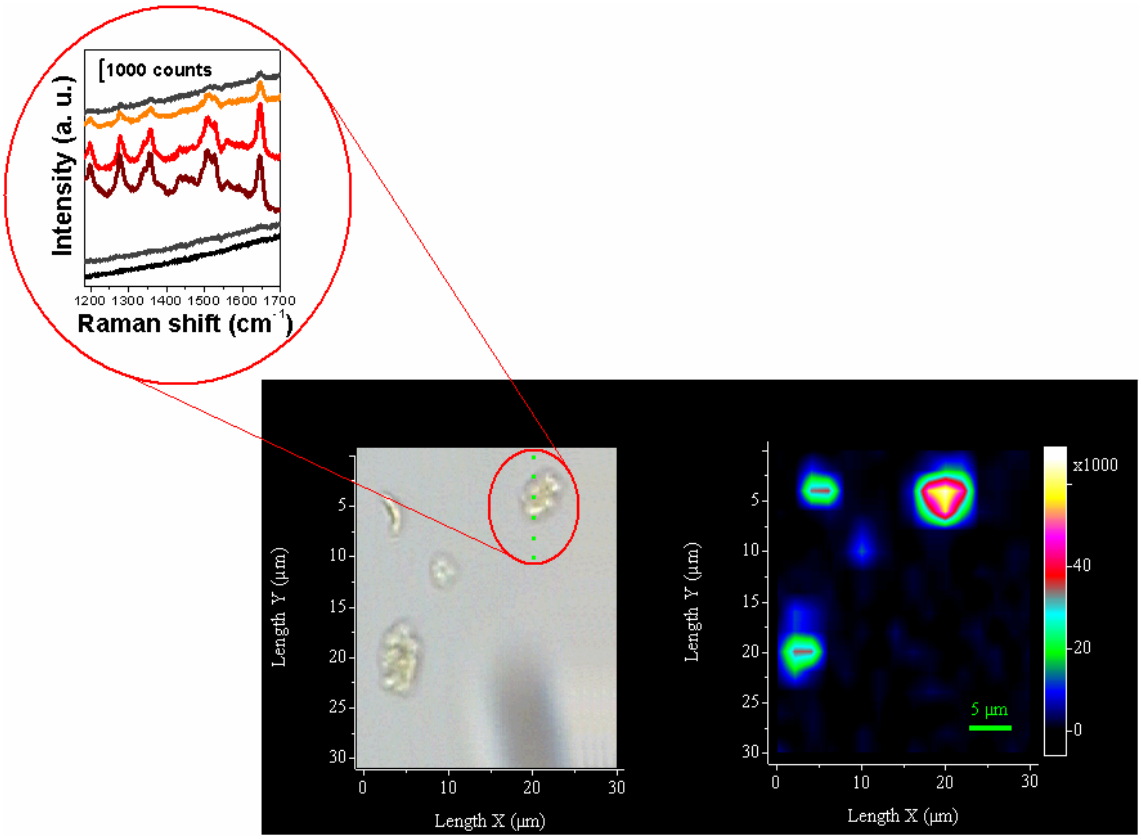

Figure 9.8 Photograph of *Salmonella* after binding to the modified SERS tags (left), SERS intensity map (right) indicating distribution of *Salmonella* bacteria, and the original Raman spectra (no baseline correction and smoothing) on six green points (insert). The maps are constructed on the band area at 1646.2 cm^{-1} (λ_{ex} = 633 nm, accumulation time 10 s, water immersion objective 63×, step size 2 µm).

9.4 Summary

In this chapter, core-shell SERS tags were successfully synthesized by a rapid procedure. Additionally, the size and the shape were well characterized by TEM. Several differently labeled SERS tags could be prepared by simply employing different dyes. The narrow, well- resolved bands allow employing multiple SERS tags simultaneously in a single detection system. Additionally, the synthesized SERS tags exhibit a high stability in different environments. Moreover, the experimental results showed that a rapid and specific method for bioimaging of cells could be built after modifying the SERS tags with antibodies. The core-shells SERS tags could also be modified with other recognition elements, such as DNA or aptamers. Accordingly, the application of core-shells SERS tags in biochemical analysis is vast.

III. Conclusions and Future Work

Research Summary

The research work in this thesis can be divided into two parts. In the first one, a new size-dependent PA effect of GNPs and its theoretical foundation was described, and applied in chemical sensing. The second part discusses the applications of nanoparticle probe and surface-enhanced Raman scattering in the field of chemical and biological sensing.

The strong size-dependent effect of GNPs is described in CHAPTER 4. This new effect was discovered when our group studied the PA response of GNP suspensions. We found that the PA signal of GNPs was enhanced by several orders of magnitude after aggregation. This phenomenon is in contradiction to the conventional PA theory. According to it, the PA amplitude of homogeneous liquids is direct proportional to their absorbance, but the absorbance of GNPs at the illumination wavelength (532 nm) decreases significantly after aggregation. We realized the observed PA signal was actually produced from a phenomenon called laser-induced nanobubble, and the size of GNPs plays an important role in this phenomenon. After running simulations based on the widely known Rayleigh-Plesset cavitation model [120, 224-225, 228-230], an equation that appropriately explained the new effect was acquired. Thus, the equation was validated by further experiments. All the relevant results showed a good accordance with the new equation.

The following sections mainly describe the applications of this new PA effect in chemical and biological sensing. As mentioned above, the equation implies that PA signal produced by laser-induced nanobubble on GNPs (*PA-LINB*) strongly depends on GNPs size. As a result, *PA-LINB* can be used as a tool to monitoring the variation of the size of GNPs.

In CHAPTER 5, we demonstrated a new way of quantification of Pb^{2+} in aqueous solution based on leaching of GNPs in the presence of $S_2O_3^{2-}$ and 2-mercaptoethanol. The corresponding size decrease was monitoring by *PA-LINB*. A very low detection

limit (0.5 nM) for Pb^{2+} can be achieved. An additional advantage provided by *PA-LINB* is that this assay can be performed in scattering media. Furthermore, based on the relevant information we obtained in this experiment, the equation could be validated once more.

Since aggregation can be seen as a GNP size increasing process, it is reasonable to hypothesize that *PA-LINB* can be utilized for detecting aggregation. This assumption was tested in CHAPTER 6. A model system, avidin triggered aggregation of biotin conjugated GNPs, was used to test this hypothesis. The results show, *PA-LINB* is ten times more sensitive than traditional aggregation monitoring tools (UV/Vis absorption) at optimized conditions. This application also represented the first work of PA spectroscopy in selective molecular detection，in which a low detection limit (0.2 nM) for avidin was achieved.

In the following section, CHAPTER 7, we further extended this sensitive tool to an aggregation-based assay for Pb^{2+}. This approach is very sensitive and selective for Pb^{2+} ions. The detection limit (42 nM) is well below the maximum contamination level for lead (75 nM) in drinking water as defined by the U.S. Environmental Protection Agency. But, it should be noted here that the aggregation of GNPs is influenced by many factors, such as pH value, ion strength of the sample etc. Since the sensing mechanisms of the two discussed applications are based on GNPs aggregation, the practical applications of them may be limited. However, these limitations should not be considered as the drawbacks of the PA effect as aggregation detection tool.

In the second part of this thesis, we tried to directly detect the antigen-antibody binding by SERS. Many label-free SERS detection schemes have demonstrated and tested in CHAPTER 8. But all these attempts yielded unsatisfied results. Hence, we switched to an indirect way, which was based on labeled SERS nanoparticle probes. In CHAPTER 9, a rapid and straightforward way for the synthesis of core-shell SERS tags was demonstrated. Then, the tags were functionalized with anti- *Salmonella* antibody as a model to present a potential application of tags in biological sensing.

Future Research Directions

The approximations of the equation show good accordance with the observed phenomena. Yet the intrinsic mechanism of the size-dependent PA effect on GNPs remains unknown. By taking a broad view on all the optical properties of GNPs, one would notice the similarity of this effect to many surface-enhanced optical phenomena. For instance, when the GNPs aggregate, the Raman scattering of the molecules absorbed on GNPs can also be enhanced several orders of magnitude, as well as many nonlinear optical responses. Due to these similarities, we believe that this PA effect is also a surface-enhanced phenomenon. If this assumption would be correct, the intrinsic mechanism of this effect would also relate on the enhancement of electromagnetic fields on the particle surface. This could also be the direction of future work, as the study of the intrinsic mechanism of this size-dependent PA effect may also help to explain other surface-enhanced effects.

IV. Experimental Section

Contents

---

1. Instrument

1.1 PA Spectroscopy

1.1.1 The Setup

The PA system used in this thesis is shown in Figure E1 (top). A frequency-doubled, Q-switched Nd:YAG laser (SL280 Spectron Laser System, Frankfurt, Germany, 532 nm, 6 ns, 10 Hz) was employed. The laser beam was focused by a planoconvex lens (100 mm focal length) into a conventional 1-cm glass cuvette equipped with a piezoelectric transducer on one side (side-on detection) [224]. The PA signals were amplified (HCA-100M-50k-C high speed current amplifier, Femto, Berlín, Germany) and recorded with a digital oscilloscop. A fraction of the laser beam was coupled out, which was employed for online monitoring of the laser pulse energy by a pyroelectric detector (Pyroelectric J25LPMB, Laser System, Dieburg, Germany). To obtain a reliable time reference, the oscilloscope was triggered by the Q-switch trigger of the Nd:YAG laser. For improvement of the signal-to-noise ratio, each PA measurement was averaged over 50 laser pulses. The data acquisition was performed with an in-house developed software (programmed in MATLAB 6.5).

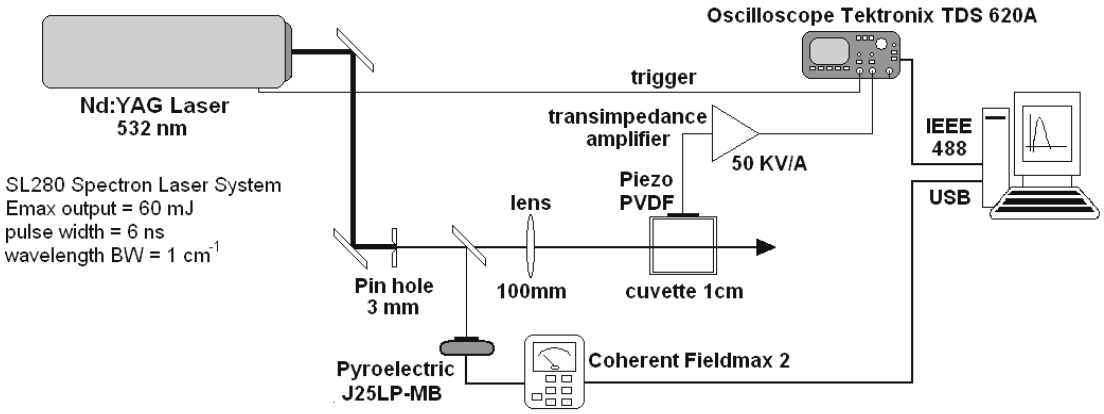

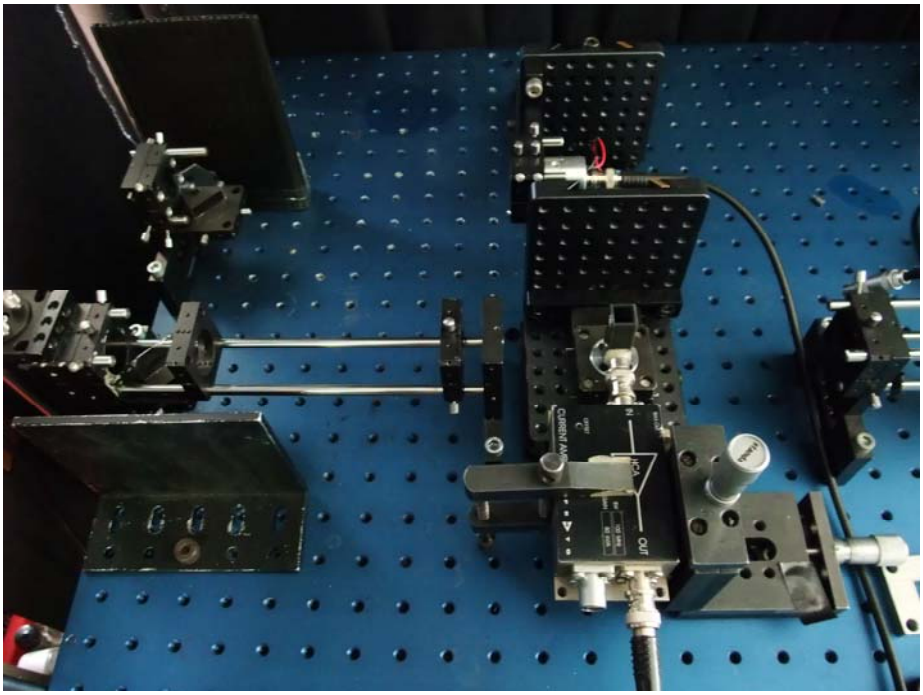

Figure E1 Scheme (top) and image (down) of the experimental setup.

1.1.2 PA Sensor Cuvette

Figure E2 shows the PA sensor cuvette used in this study. For the detection of the acoustic signal, a 25-µm thick piezoelectric PVDF film (bi-oriented piezoelectric PVDF, Piezotec SA, Saint-Louis, France) was used. The PVDF film was circular with a diameter of 6 mm and was coupled to a conventional 1-cm glass cuvette by a conductive epoxy. The conductive epoxy provides both electric and acoustic contacts. The electrode was coupled with conductive epoxy to the other side of the PVDF film. The electrodes were connected to a BNC socket. A glass cuvette is sufficiently chemically inert and provides acoustic coupling with the water. The acoustic transmission factor between water and glass is 1.8, between glass and conductive epoxy is 0.85 and between the epoxy and PVDF is 0.53. For each interface transmission factor can be calculated according Eq. 2.19. Hence, the acoustic transmission efficiency of the system "water/glass/epoxy/PVDF" is 0.82 [289].

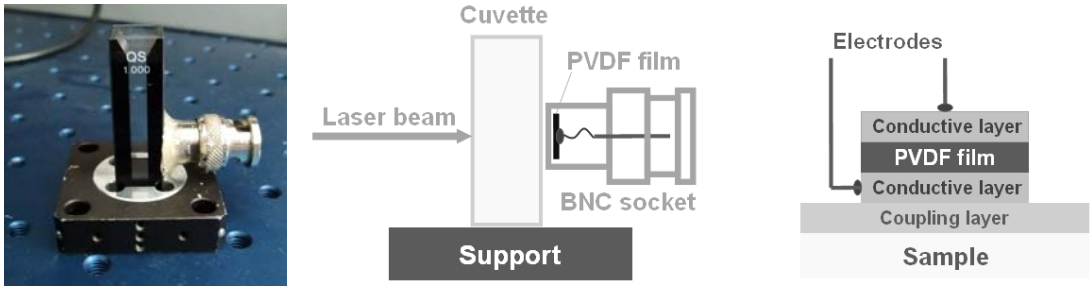

Figure E2 Image (left) and schematic setup (middle) of PA sensor cuvette, and the scheme of coupling of piezoelectric polymer film (right).

1.1.3 PA Signal Analysis

The PA signals were detected perpendicularly to the laser beam, as shown in Figure E3 (top). A typical PA signal detected by our PA setup is also shown in Figure E2. The origin of the abscissa is set to the instant of laser pulse generation. The noise in the first ~1 µs originates from electromagnetic emissions of the Q-switch of the Nd: YAG laser. The peak at t_a = 2.25 µs is the PA signal of GNPs.

As shown in Figure E3, the time delay (t_a) the generated pressure pulse needs to reach the cuvette walls, where the detector is placed, depends on a distance d and the speed of sound in the corresponding medium: $t = d/c$. According to this equation, t_a corresponds to a distance of 2.1 mm in water with a sound velocity of 1490 ms^{-1} (the distance between the inner walls and the center of the cuvette) plus 4.1 mm in glass with a sound velocity of 5000 ms^{-1} (cuvette walls thickness).[1] A detailed view of the PA signal is shown in the inset of figure E3. The p_{ac} in this figure represents the amplitude of PA signal, which was adopted in all PA measurements.

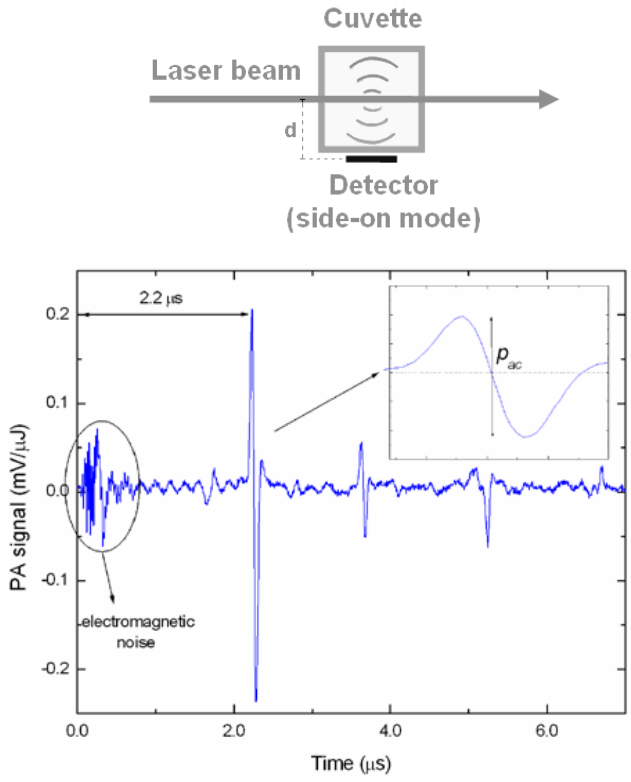

Figure E3 Image of Side on dectecting mode (top) and a typical PA signal (down). The inset shows an expanded view around the main peak.

1.2 Raman Spectroscopy

For the Raman measurements, a confocal Raman System Renishaw 2000 (Renishaw, U.K.) was used. A 633 nm laser source (beam power: 25 mW) was employed for excitation, and a motorized XY stage was utilized to perform Raman mapping. Calibration of the instrument was done referring to the 520 cm^{-1} line of silicon. All spectra were processed via the WiRE 1.2 software based on GRAMS 32 (version 4.14, Thermo Galactic) which controlled the instrument itself including data acquisition.

1.3 UV/Vis Spectroscopy

UV/Visible absorption spectra were collected by means of a scanning spectrophotometer (Beckman 650).

1.4 TEM

Transmission electron micrographs were taken using a JEOL JEM 2010 instrument.

2. Materials

2.1 Chemcials

The following reagents were used without further purification and Milli-Q water (18 $M\Omega \cdot cm^{-1}$) was used to prepare all aqueous solutions.

Albumin from bovine serum (A3912, Sigma-Aldrich, Steinheim)

3-Aminopropyltrimethoxysilane (281778, Sigma-Aldrich, Steinheim)

Ammonia, 25 wt % (105428, Merck, Darmstadt)

Ascorbic acid (A5960, Sigma-Aldrich, Steinheim)

Barium nitrate (101729, Merck, Darmstadt)

Calcium chloride (499609, Merck, Darmstadt)

Cadmium acetate dihydrate (32308, Riedel-de Haën)

Cobalt(II) nitrate hexahydrate (60833, Sigma-Aldrich, Steinheim)

Chromium(III) nitrate nonahydrate (27080, Sigma-Aldrich, Steinheim)

Copper(II) sulfate pentahydrate (102790, Merck, Darmstadt)

Crystal violet (C3886, Sigma-Aldrich, Steinheim)

Cysteamine (30070, Sigma-Aldrich, Steinheim)

Dimethylformamide, water-free (227056, Sigma-Aldrich, Steinheim)

4-(Dimethylamino)pyridine (29224, Sigma-Aldrich, Steinheim)

5, 5'-Dithiobis (2-nitrobenzoic acid)(D218200, Sigma-Aldrich, Steinheim)

Hydroxylamine hydrochloride (159417, Sigma-Aldrich, Steinheim)

Hydrogen tetrachloroaurate(III) (520918, Sigma-Aldrich, Steinheim)

Iron(III) chloride (236489, Sigma-Aldrich, Steinheim)

Iron(II) sulfate tetrahydrate (Fisher Scientific, Pittsburgh, PA, USA)

Fluorescein 5(6)-isothiocyanate (46950, Sigma-Aldrich, Steinheim)

L-Glutathione (23150, SERVA Electrophoresis GmbH)

Methyl cyanide (34998, Sigma-Aldrich, Steinheim)

2-Mercaptoethanol (63689, Sigma-Aldrich, Steinheim)

Magnesium chloride hexahydrate (442615, Merck, Darmstadt)

Manganese(II) chloride tetrahydrate (M9522, Sigma-Aldrich, Steinheim)

N-(+)-Biotinyl-6-aminocaproic acid N-succinimidyl ester (14412, Sigma-Aldrich, Steinheim)

Nickel(II) nitrate hexahydrate (72253, Sigma-Aldrich, Steinheim)

N, *N*′-Disuccinimidyl carbonate (225827, Sigma-Aldrich, Steinheim)

2-Propanol (molecular biology grade, SERVA Electrophoresis GmbH)

Lead(II) nitrate (107398, Merck, Darmstadt)

Tetramethylrhodamine-5-isothiocyanate (T0820, Sigma-Aldrich, Steinheim)

Trisodium citrate (71402, Sigma-Aldrich, Steinheim)

TWEEN 20 (P9416, Sigma-Aldrich, Steinheim)

Silver nitrate (101510, Merck, Darmstadt)

Sodium thiosulfate (S8503, Sigma-Aldrich, Steinheim)

Tetraethyl orthosilicate (86580, Sigma-Aldrich, Steinheim)

Zinc chloride (20808, Sigma-Aldrich, Steinheim)

2.2 Antibody and Bacteria

Anti-*Salmonella* (pAb goat, CAT No. G5 V61-500, 2.0 - 2.5 g/L) were purchased from BioDesign International (Saco).

Heat-inactivated *Salmonella typhimurium* ATCC 14028 cells were a gift from the Instituto Zooprofilattico Sperimentale Dell'Abruzzo e del Molise "G. Caporale" (Teramo, Italy).

Anti-Benzo[a]pyren antibody (mAb mouse, Institut für Wasserchemie der TU München).

3. Synthesis

3.1 Synthesis of GNPs

Gold nanoparticles with different sizes were prepared as described previously with slight modifications [44, 239-240].

GNP 1: 5 mL of 1% trisodium citrate was quickly mixed with 1.7 mL of 1% $HAuCl_4$ in 50 mL of boiling water solution under vigorous stirring.

GNP 2: 800 µL of 1% $HAuCl_4$ was quickly adding to the solution contained 9.0 mL of 40 mM $NH_2OH{\cdot}HCl$ and 10 mL of GNP 1 and 81 mL H_2O at room temperature.

GNP 3: 600 µL of 1% $HAuCl_4$ was quickly adding to the solution contained 2.2 mL of 40 mM $NH_2OH{\cdot}HCl$ and 40 mL of GNP 2 and 58 mL H_2O at room temperature.

GNP 4: 295 µL of 1% $HAuCl_4$ was quickly adding to the solution contained 2.2 mL of 40 mM $NH_2OH{\cdot}HCl$ and 25 mL of GNP 3 and 72 mL H_2O at room temperature.

GNP 5: 220 µL of 1% $HAuCl_4$ was quickly adding to the solution contained 2.2 mL of 40 mM $NH_2OH{\cdot}HCl$ and 20 mL of GNP 4 and 78 mL H_2O at room temperature.

GNP 6: 160 µL of 1% $HAuCl_4$ was quickly adding to the solution contained 2.2 mL of 40 mM $NH_2OH{\cdot}HCl$ and 40 mL of GNP 5 and 58 mL H_2O at room temperature. From GNP 2 to GNP 6, additional 1.0 mL of 1% trisodium citrate was added to stabilize the nanoparticles after the synthesis.

Table E1 shows the detailed information of all six batches of GNPs. The absorption peaks and their intensities were obtained by means of the UV/Vis spectroscopy (Beckman 650). The molar concentration of GNP 1 (2.5×10^{-8} M) was determined according to the Beer's law by using the extinction coefficient of 10^8 $M^{-1}{\cdot}cm^{-1}$ for GNP with a diameter of 13 nm at 520 nm [290]. Thus，the number concentration of GNP 1

(1.5×10^{13} particles/mL) can be estimated based its molar concentration. According to previous reports [44-45, 239], the reduction of Au^{3+} by NH_2OH is dramatically accelerated by Au surfaces. As a result, no new particle nucleation occurs in solution during the preparation. Hence, from GNP 2 to GNP 6, the number concentration was calculated based on the small GNP concentration that were added as seeds. The NP sizes were verified by TEM images (at least 200 particles were measured, respectively).

Table E1 Detailed information about the gold nanoparticles.

	GNP 1	**GNP 2**	**GNP 3**	**GNP 4**	**GNP 5**	**GNP 6**
λ_{max} (nm)	518.0	526.0	522.5	525.5	537.0	560.0
Extinction (cm^{-1})	2.50	1.07	1.04	0.49	0.39	1.07
Concentration (particles/mL)	1.5×10^{13}	1.5×10^{12}	6.0×10^{12}	1.5×10^{11}	3.0×10^{10}	1.2×10^{10}
Diameter (nm)	12.5 ± 1.0	19.1 ± 2.6	26.4 ± 3.5	44.9 ± 6.8	60.0 ± 7.9	83.3 ± 10.5

3.2 Synthesis of AgNPs

Colloidal Ag was prepared from $AgNO_3$ reduced by $NH_2OH{\cdot}HCl$, as described by Leopold and Lendl with slight modifications [291]. Briefly, 11.6 mg of $NH_2OH{\cdot}HCl$ dissolved in 100 mL of H_2O was mixed with 3.3 mL of 0.1 M NaOH. Then, 9 mL of the above solution, 1 mL of 10 mM $AgNO_3$ was added under gentle stirring at room temperature. A rapid color change was observed, and finally a clear brownish-yellow Ag colloids could be obtained. Then, colloidal Ag was stored at 4°C until use.

3.3 Synthesis of Biotin-conjugated GNPs

Gold nanoparticles with different sizes were synthesized as described previously. Biotin-labelled GNPs were prepared by the following steps: 1.0 mg (2.2×10^{-6} mol) N-(+)-biotinyl-6-aminocaproic acid N-succinimidyl ester and 0.17 mg (2.2×10^{-7} mol) cysteamine were dissolved in 1.0 mL water-free DMF. Four hours later, 100 μL of the above solution was added into 10 mL GNPs under gentle stirring at room temperature. After 10 min, 300 μL 10% Albumin from bovine serum (BSA) was added to help to stabilize the nanoparticles and incubated overnight at room temperature. Then the biotin-GNP was separated from the reaction mixture by centrifugation and redispersed in 10 mL H_2O containing 0.1% BSA, and stored in 4 °C until use.

3.4 Synthesis of GSH-GNPs

GNPs with diameter 26.4 ± 3.5 nm (number concentration 6×10^{11} particles/mL) were used in this experiment. GSH-conjugated GNPs were prepared by following procedures: firstly, the pH value of GNPs suspension was adjusted to ~10 by 0.1 M K_2CO_3. To 10 mL of the above GNPs suspension, 780 μL of 0.019 M L-glutathione was added under gentle stirring. As results, the pH value of the suspension gradually decreased to ~8. The mixture was subsequently left overnight without disturbance at room tempture. The excess GSH in solution was removed by dialyzed in 0.1% (wt) sodium citrate solution. Then, the resulting GSH- conjugated GNPs were kept at 4 ^{o}C until use.

3.5 Synthesis of anti-B[a]P Antibody-conjugated GNPs

The pH value of gold colloids (GNP 1) was first adjusted to ~ 9 by 0.1 M K_2CO_3. Then 1 mL of the above GNPs suspension was mixed with 50 μL of 1mg/mL anti-B[a]P antibody under gentle stirring. After 10 min, 150 μL of 5% (wt) BSA was added and stand for 1h. After centrifugation and washing by PBS (0.1 M, pH 7.2), the antibody-conjugated GNPs were dispersed in 0.1 mL PBS and were stored at 4°C until use.

3.6 Synthesis of Core-Shell SERS Tags

In a typical procedure, aliquot of 10^{-5} M Raman reporter molecule solution was gently mixed with 1 mL of the silver or gold colloids and allowed to stand for 30 min. Then the mixture was slowly transferred into 2-propanol (H_2O/2-propanol ratio maintained at 1/5). Under gentle stirring, 150 μL of ammonia (25%, wt) and 3.62 μL of tetraethyl orthosilicate were added consecutively. The reaction was allowed to proceed for 10 min at room temperature. The tags can be separated from the reaction mixture by centrifugation for 10 min at ~1430 g, washed twice by 1 mL of ethanol, and then redispersed in 1 mL of H_2O or other solvents as needed.

3.7 Modification of SERS Tags with anti-*Salmonella* Antibody

The goat anti-*Salmonella* antibody was immobilized on the surface of SERS tags via the following procedure. First, the amino groups were introduced to the surface of the tags. Aliquot of 5 μL of 3-aminopropyltrimethoxysilane was injecting into 500 μL of SERS tags dispersed in 5 mL of ethanol under gentle stirring and stand 30 min at room temperature. Then, the tags were successively washed with ethanol, H_2O, DMF, and finally redispersed in 1 mL of anhydrous DMF. Then the tags were treated with 160 mg of N, N'-disuccinimidyl carbonate, 8 mg of 4-(dimethylamino)pyridine and 250 μL of triethylamine dispersed in 3.2 mL of anhydrous DMF for 1 h. After centrifugation and washing with ethanol, the tags were dispersed in 1 mL of MES buffer (pH 4.65) followed by the addition of 400 μL of 1 mg/mL pAb anti-*Salmonella* antibody. After 4 h, 500 μL of 40 mM glycine was added for deactivation overnight. After centrifugation and washing with PBS, the tags were dispersed in 1 mL of PBS (pH 8.2, 1% NaN_3) and were stored at 4 °C until use.

4. List of Experiments

Ex. 1

GNPs with different average sizes were prepared as previously described. Then, six batches of colloidal gold were diluted by Milli-Q water to obtain the same extinction at 532 nm (~0.226 cm^{-1}), which was verified by UV/Vis spectroscopy. Then the six batches of colloidal gold were tested by our PA setup, and corresponding PA signals were recorded and were plotted in Figure 2.2.

Ex. 2

Firstly, colloidal gold (GNP 1) was diluted fifty times by Milli-Q water and 1.5 ml of it was placed in the PA sensor cuvette. Then, the samples of gold colloids were irradiated under various fluencies and the corresponding PA responses were recorded.

Ex. 3

Samples of colloidal gold with different number concentrations were obtained by diluting the corresponding colloidal gold according to the dilution rations shown in following table. Then the samples were tested by the PA setup, and the corresponding PA response were show in Figure 2.6 after normalized to the laser fluencies.

Table E2

	Dilution ratios			
Sample No.	**GNP 1**	**GNP 2**	**GNP 3**	**GNP 6**
1	5	3	3	2.5
2	10	5	4	5
3	25	7	5	10
4	50	10	10	30
5	100	15	15	50
6	200	25	30	
7		50	50	

Ex. 4

Six batches of GNPs with different average sizes were measured by the PA setup. The PA responses normalized to their particles concentration and to laser fluencies were shown in Figure 2.7. The results are used to compare with the results obtained from simulation.

Ex. 5

Firstly, 2.36 mL of colloidal gold (GNP 1) was first diluted by 30 mL of 5 mM glycine-NaOH buffer (pH 10.0). In a typical Pb^{2+} detection procedure, 3mL of the above diluted GNPs was equilibrated with 1 mL of 5 mM $Na_2S_2O_3$ (in buffer) and additional 1 mL buffer at room temperature for 15 min. Then Pb^{2+} ions (final concentration 0, 100, 250 μM) and 102 μL of 50 mM 2-mercaptoethanol were added to the above mixture. Then, the mixture was gentle shaking at room temperature for 2 h. An aliquot of 1mL of the mixtures was then transferred into the PA sensor cuvette for PA measurement. For comparison, the UV/Vis spectra were also collected, and aliquots of the mixtures were placed on the copper grids for TEM measurement.

Ex. 6

In this experiment, 0.788 mL of colloidal gold (GNP 1) was first diluted by 5 mL of 5 mM glycine-NaOH buffer (pH 10.0). Then, 3 mL of the above diluted colloidal gold was mixed with 1 mL of 5 mM $Na_2S_2O_3$ (in buffer) and additional 1 mL buffer. And Pb^{2+} ions were added to each aliquot to give a final concentration of 5 μM. The mixture was equilibrated at room temperature. After 15 min, two aliquots (1 mL) of the mixture were transferred into a glass cuvette and the PA sensor cuvette, respectively. After addition of 20.4 μL of 50 mM 2-mercaptoethanol to each aliquot, the corresponding PA signals and UV/Vis spectra of the sample were recorded by our PA setup and the UV/Vis spectrometer, respectively.

Ex. 7

In order to determine the optimum size for the assay, five different GNPs were used to perform the assay ($D_{np:}$ 12.5, 26.4, 44.9, 60.0, 83.3 nm). The corresponding PA responses of each size were recorded (the ratio of the Pb^{2+} concentration to the total surface GNP in the each sample were maintained constant).

Ex. 8

For Pb^{2+} sensing, 5 mL of 5 mM glycine-NaOH solution (pH 10.0) solutions containing the GNPs 1 (1.25 nM), $Na_2S_2O_3$ (1.0 mM), and Pb^{2+} ions (0 ~ 10 μM) were equilibrated at room temperature for 15 min. Then, 10 μL of 50 mM 2-mercaptoethanol was added to each of these mixtures, which were equilibrated through gentle shaking at room temperature for other 2 h. The mixtures were measured by the PA setup and UV/Vis spectroscopy, respectively. In this section, the final concentrations of the species were provided.

Ex. 9

In order to evaluate the performance of this assay in scattering medium, a similar experiment to Ex.8 was performed. One difference of this experiment is that each sample contained 0.05 g/L of spherical silica particles (diameter 500 nm) as scattering materials. For comparison, the UV/Vis responses were also collected.

Ex. 10

The as prepared biotin-conjugated GNPs (average diameter 12.5 nm) was diluted by Milli-Q water to obtain a particle concentration of 1.5×10^{12} particles/ml. Then, an aliquot of 3 mL of the above diluted biotin-conjugated GNPs was placed in the PA sensor cuvette and a glass cuvette, respectively. After addition of 3.3 μL of 1 mg/mL avidin, the temporal evolution PA signal was recorded. For comparison, the corresponding UV/Vis absorption spectra were also collected.

Ex. 11

To evaluate the influence of GNPs size to the sensitivity, GNPs with different diameters (12.5 and 26.0 nm) were used to syntheses the biotin-conjugated GNPs. Then, these biotin-conjugated GNPs were diluted to obtain different particles concentrations to perform the assay. The PA responses of them to different avidin concentrations are measured.

In a typical procedure, aliquots (3 mL) of Biotin-conjugated GNPs suspensions were maintained at room temperature in the presence of avidin (0 - 432 nM) for 2 h. Then, a part of the above aliquots (1.5 mL) was measured by our PA setup. For comparison, the other part (1 mL) was measured by the UV/Vis spectrometer.

Ex. 12

Firstly, the as prepared GSH-conjugated GNPs (average diameter 26.4 nm) were diluted ten times by Milli-Q water. Then, in each 10mL of the above diluted GSH-conjugated GNPs, Pb^{2+} ions form one stocking solution (10mM) were added (resulting a final concentration 0.1, 1, 10 μM) in the presence of 0.1 M NaCl. The mixtures were equilibrated at room temperature through gently shacking for 20 min. Then, the mixtures were tested both by the PA setup and the UV/Vis spectrometer.

Ex. 13

To evaluate the influence of salt concentration, the assay was performed under different NaCl concentrations. Aliquots of 1.0 mL of ten times diluted GSH-conjugated GNPs were mixed with different volumes (0, 20, 40, 60, 80, 100 μL) of 1 M NaCl in the presence of 10 μM Pb^{2+}. Then the changes of absorption of the mixtures were recorded by the UV/Vis spectrometer.

Meanwhile, in order to study the stability of GSH-conjugated GNPs at high concentration of NaCl solution, an aliquot of 1.0 mL of ten times diluted GSH-conjugated GNPs was mixed with 100 μL of 1 M NaCl, and the corresponding UV/Vis spectra were collected. .

Ex. 14

To evaluate the selectivity of this assay, it was challenged with other environmentally relevant metal ions, including Ba^{2+}, Ca^{2+}, Cd^{2+}, Co^{2+}, Cr^{3+}, Cu^{2+}, Fe^{2+}, Fe^{3}, Mg^{2+}, Mn^{2+}, Ni^{2+}, and Zn^{2+} ions. In a typical experiment, 20 μL of 0.1 mM metal salts solution were added to 1 mL of 20 times diluted GSH-conjugated GNPs. After addition of 100 μL of 1 M NaCl, the mixtures were gently shacked for 20 min at room temperature, and then were tested by the PA setup.

Ex. 15

In a typical procedure, 50 μL of GSH conjugated GNPs suspension was added to 950 μL water samples containing different Pb^{2+} (0 ~ 8 μM), then additional 60 μL of 1 M NaCl was added in. After 20 min, the sampled were analysis by our PA setup.

Ex. 16

An aliquot of 5 μL of anti-B[a]P antibody conjugated GNPs was mixed with 5 μL of 10^{-6} M of B[a]P dissolved in 10% methyl cyanide solution. After 15 min, the mixture is a subject of SERS measurement. For comparison, the SERS spectrum of 10% methyl cyanide (buffer), anti-B[a]P antibody conjugated GNPs (SERS probe) were also collected. The SERS spectrum of B[a]P was measured by mixed 100 μL of 10^{-6} M B[a]P(in 10% methyl cyanide) with 100 μL Ag NPs as well as 5 μL of 1 M NaCl.

Ex. 17

An aliquot of 5 μL of anti-B[a]P antibody conjugated GNPs were mixed with 100 μL of 10^{-5} M of B[a]P. After 1 h later, the anti-B[a]P antibody conjugated GNPs were be separated from the mixture by centrifugation for 10 min at ~ 16000 g, and washed twice by 100 μL of PBS, and then redispersed in 100 μL of H_2O. After addition of 10 μL of Ag NPs, it was tested by Raman spectroscopy.

Ex. 18

An aliquot of 5 μL of anti-B[a]P antibody conjugated GNPs were mixed with 5 μL of 10^{-5} M of B[a]P in PBS. After 1 h, the mixture was treated with 10 μL silver enhancement solution. One minuet later, the mixture was tested by Raman spectroscopy. The silver enhancement solution was freshly prepared, containing 0.5% (wt) of Tween 20, 1 mM of $AgNO_3$ and 1 mM of ascorbic acid in water.

Ex. 19

In order to test the stability of SERS tags in different solvents, the SERS tags were separated from the suspension by centrifugation at ~ 1430 g for 10 min, and then redispersed in 1 mL of 1 M NaCl, 1 M HCl，1 M NaOH，ethanol，THF，DMF, respectively. Thus, the tag suspensions were subjects of UV/Vis measurement. By comparison, silver nanoparticles dispersed in corresponding solvents were also tested by UV/Vis spectroscopy.

Ex. 20

In 10 μL SERS tags, 1 μL of 10^{-4} M crystal violet was added, and the mixture was measured by Raman spectroscopy.

Ex. 21

The sample for imaging was prepared by fixing *Salmonella* bacteria on a glass slide, as previous described [292]. Briefly, a glass slide was cleaned and modified with amino groups. After the surface was activated by N,N'-disuccinimidyl carbonate and 4-(dimethylamino)pyridine, the goat anti-*Salmonella* antibodies were spotted on it using a BioOdyssey Calligrapher miniarrayer. The slide was treated with 100 μL of 10^8 cells/mL of *Salmonella* bacteria (CAYLA, France, 10^{11} cells/mL) for 10 min and washed several times by PBS buffer (pH 7.2, containing 0.05% Tween 20). After deactivating and blocking by 2% casein (in PBS buffer) for 4 h, the slide was ready for

imaging process. A volume of 100 μL of diluted (10 times) modified tags was exposed to the slide for 10 min, and then the slide was washed thoroughly by PBS (pH 7.2, containing 0.05% Tween 20). Thereafter, the SERS intensity map was collected in an area of 30 μm × 30 μm on the slide, using a 63× water immersion objective.

4. Simulations

4.1 Theory

The simulation of PA signal produced by LINB on GNPs was calculated by Dr. Martín G. González using MATLAB 6.5 based on following theories and equations.

Generally speaking, when illuminated by strong laser pulses, the temperature of GNP continues to rise after reaching the boiling temperature of water. We assume that all the excess energy absorbed by the GNP during the laser pulse is spent to heat the water at the critical temperature T_{cw}. Hence, the initial amount of evaporated water can be estimated as by [225],

$$m_{b,0} = \frac{4}{3} \cdot \pi \cdot \left(R_{b,0}^3 - R_{np}^3\right) \cdot \rho_{cw} = \frac{\left(F - F_c\right) \cdot \sigma_{abs}}{E_{cw}} \tag{1}$$

Where $R_{b,0}$ is the initial radius of the bubble, R_{np} is the radius of a GNP, ρ_{cw} *is* the critical density of water, F is the fluence of the laser, E_{cw} is the internal energy of water at the critical temperature, F_c is the critical threshold laser fluence for LINB, σ_{abs} is the absorption cross section of GNP.

Hence, the initial radius of bubble $R_{b,0}$ can be estimated by the following equation,

$$R_{b,0} = \left(\frac{3}{4 \cdot \pi \cdot \rho_{cw}} \cdot \left(\frac{\left(F - F_c\right) \cdot \sigma_{abs}}{E_{cw}} \right) + R_{np}^3 \right)^{1/3} \tag{2}$$

Where the threshold F_c can be obtained by Eq. (3) and Eq. (4),

$$F_c = \frac{\chi_w \cdot \tau_L}{\sigma_{abs}} \cdot \frac{4 \cdot \pi \cdot R_{np} \cdot c_w \cdot \rho_w \cdot T_{bo}}{1 + \frac{\xi_1}{\xi_2 - \xi_1} \cdot \mathrm{erfcx}\left(\xi_2 \cdot \sqrt{\frac{\chi_w \cdot \tau_L}{R_{np}}} \right) - \frac{\xi_1}{\xi_2 - \xi_1} \cdot \mathrm{erfcx}\left(\xi_1 \cdot \sqrt{\frac{\chi_w \cdot \tau_L}{R_{np}}} \right)} \tag{3}$$

$$\xi_{1,2} = \frac{3}{2} \cdot \left(\frac{c_w \cdot \rho_w}{c_{np} \cdot \rho_{np}} \mp \sqrt{\frac{c_w \cdot \rho_w}{c_{np} \cdot \rho_{np}} \cdot \left(\frac{c_w \cdot \rho_w}{c_{np} \cdot \rho_{np}} - \frac{4}{3} \right)} \right) \tag{4}$$

Here, *erfcx* is the scaled complementary error function in MATLAB 6.5, $c_{w,}$, ρ_w, are the specific heat capacity at constant pressure and density of water, $c_{np,}$ $\rho_{,np}$ are the specific heat capacity and density of GNP, respectively. χ_w is the thermal diffusion of water. τ_L is the laser pulse duration. And, in the case of $\tau_L >> 2R_{np}$, the absorption cross section σ_{abs} in Eq. (2) can be estimated as [79, 132, 293]

$$\sigma_{abs} = \frac{12 \cdot \pi \cdot R_{np}^3 \cdot \varepsilon_w^{3/2} \cdot \omega_L \cdot \varepsilon_2}{c \cdot \left((\varepsilon_1 + 2 \cdot \varepsilon_w)^2 + \varepsilon_2^2 \right)} \tag{5}$$

where, c the speed of light, ω_L the angular frequency of the illuminated radiation, and ε_w and $\varepsilon = \varepsilon_1 + i\varepsilon_2$ denote the dielectric functions of the surrounding medium (assumed to be frequency independent) and of the particle material, respectively.

The temperature and the pressure inside the initial bubble are those at the critical point of water (T_{cw}, ρ_{cw}). The time of the bubble expansion to the critical density is negligible, since time of generation of PA signals is very short (1 ns, approximately) [225].

After the initiation of the boiling, the dynamics of the bubble is governed by the Rayleigh-Plesset equation [235-236].

$$\frac{p_b(t) - p_A}{\rho_w} = R_b(t) \cdot \frac{d^2 R_b(t)}{dt^2} + \frac{3}{2} \cdot \left(\frac{dR_b(t)}{dt} \right)^2 + \frac{4 \cdot \upsilon_w}{R_b(t)} \cdot \frac{dR_b(t)}{dt} + \frac{2 \cdot \gamma_w}{\rho_w \cdot R_b(t)} \tag{6}$$

where $p_b(t)$ is the pressure inside the bubble, p_A is atmospheric pressure, υ_w and γ_w are the kinematic viscosity and surface tension of water, respectively. The term containing the surface tension acts as increased external pressure, where the viscosity acts as friction force to the bubble motion and is responsible for the damping of the oscillations [238]. Considering adiabatic expansion of the bubble,

$$V_b(t) = \frac{4}{3} \cdot \pi \cdot \left(R_b^3(t) - R_{np}^3 \right) \tag{7}$$

$$T_b(t) = T_{cw} \cdot \left(\frac{V_b(t) - b}{V_{cw} - b} \right)^{-R_s / c_{V_{cw}}} \tag{8}$$

$$p_b(t) = \frac{R \cdot T_b}{V_b(t) - b} - \frac{a}{V_b(t)^2} \tag{9}$$

where $V_b(t)$ and $T_b(t)$ are the volume and the temperature of the bubble, respectively, R_s is the specific gas constant, c_{Vcw} is the specific heat capacity at constant volumen for water at the critical point, a and b are the van der Waals equation parameters, and R is the universal gas constant.

Finally, the acoustic pressure p_{ac} producing from expanding and oscillating bubble at a distance r_s can be estimated as [238],

$$p_{ac} = \frac{\rho_w}{4 \cdot \pi \cdot r_s} \cdot \frac{d^2 V_b(t)}{dt^2} \tag{10}$$

In Table E3 summarizes the values of constants used for the simulation. In Figures E6 is given the NP cross section for diferent diameters. The figure reveals that the equation 5 fits very well the measured data.

Table E3 Constants used for the simulation

ρ_{cw}	367 kg·m^{-3}	ε_w	9.15
F	0 - 5 J/cm^2	ε_1 *	-4.9
E_{cw}	2·10^6 J·kg^{-1}	ε_2 *	2.38
ρ_w (25 °C)	997 kg·m^{-3}	T_{cw}	374 °C
c_w	2.05·10^3 J·kg^{-1}·K^{-1}	p_{cw}	218 atm
χ_w (25 °C)	9.4·10^{-8} m^2·s^{-1}	υ_w	9·10^{-7} m^2·s^{-1}
τ_L	10 ns	γ_w	0.072 N·s^{-1}
λ_L	532 nm	a	0.547 Pa·m^3·mol^{-2}
c	3·10^8 m·s^{-1}	b	3.05·10^{-5} m^3·mol^{-1}
c_{np}	1.93·10^4 J·kg^{-1}·K^{-1}	ρ_{np}	129 kg·m^{-3}

* For GNP and photon energy of $h \cdot c/\lambda_L$ where h is the Planck constant [294].

4.2 Simulation Results

In Figure E4 the simulation results of cross section σ_{abs} and evolution bubble volume for various GNP diameters are shown.

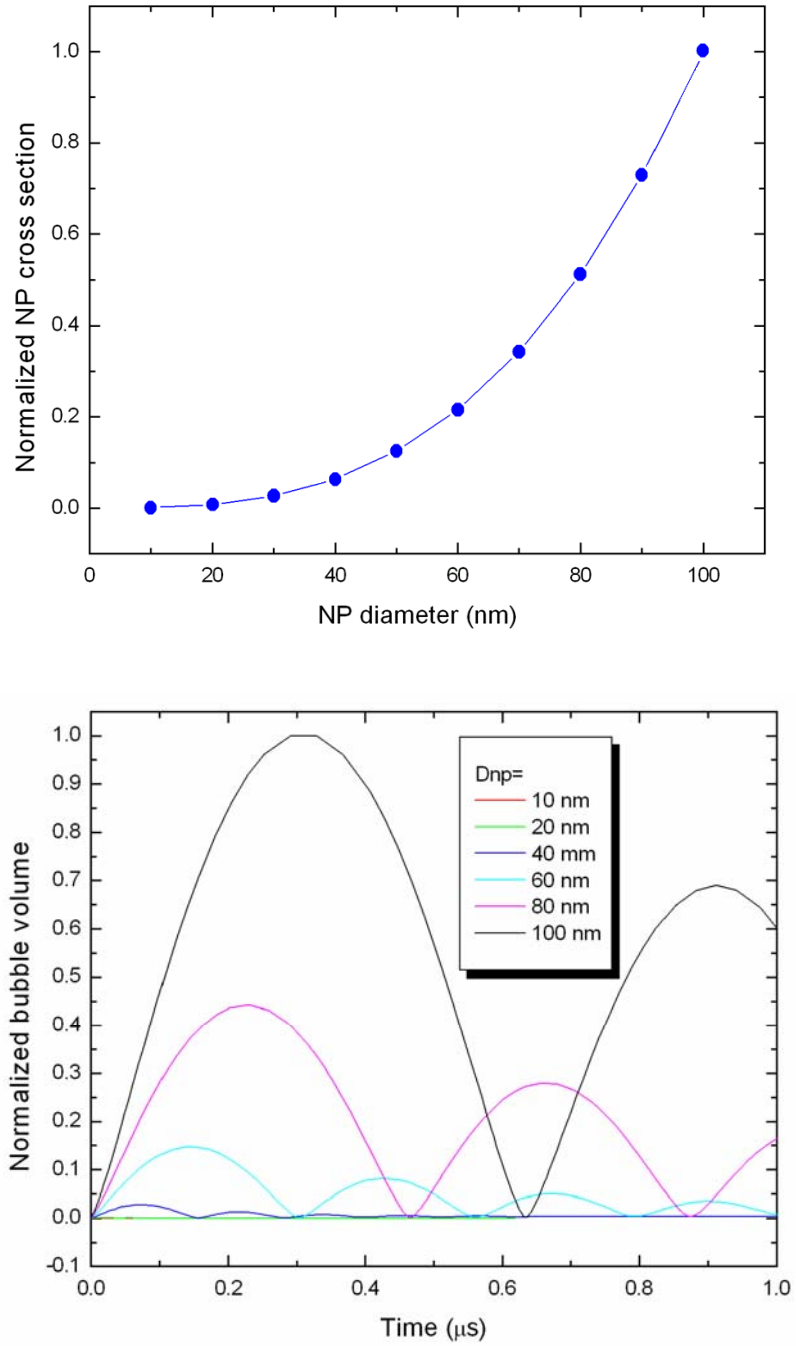

Figure E4 Normalized GNP cross section (top) and time evolution bubble volume for GNPs with various diameters (down).

The Figure E5 showed the simulation result of PA amplitudes for various GNPs diameter, and it also reveals the following relationship between the *PA-LINB* and the GNP diameter:

$$p_{ac} \propto D_{np}^{3} \tag{11}$$

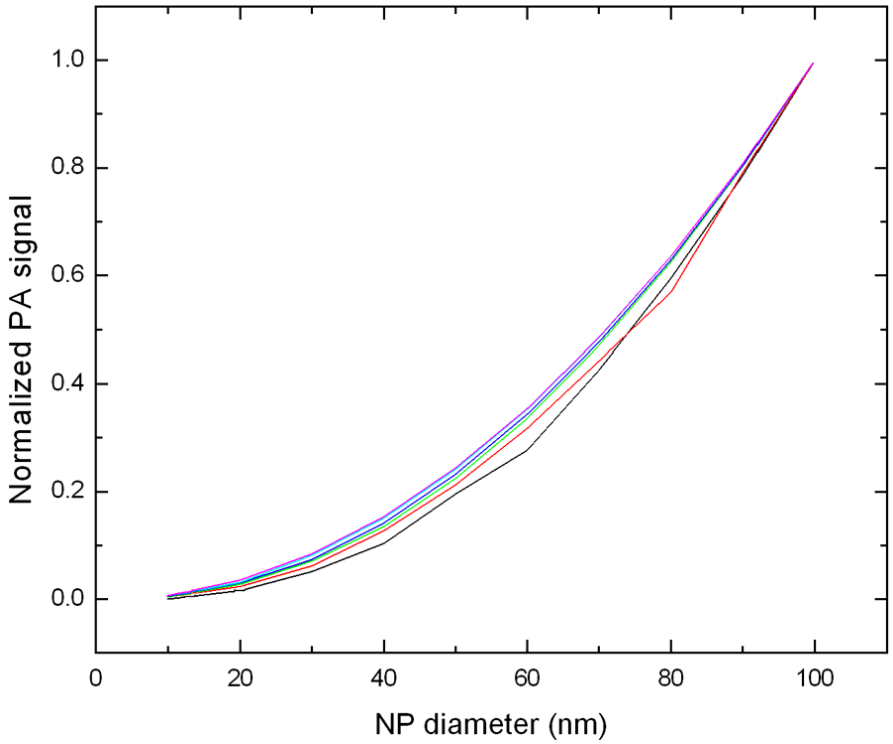

Figure E5 Simulation of PA amplitudes vs. GNPs under different laser fluences (10Fc ~ 100Fc).

V. Appendix

List of Symbols

A	Absorbance or extinction, log (I_0/I)
c	Concentration of the absorbing substance
c_0	Sound speed of in the medium
C	Constant depends on the PA setup
C_P	Heat capacity
d	Sample thickness
D_{np}	Diameter of nanoparticles
E_a	Absorbed light energy by the sample
E_{cw}	Internal energy of water at the critical point
E_t	Light energy transmitted through the sample
E_{th}	Thermal energy
F	Laser fluence
F_c	Threshold laser fluence for bubble generation
F^t_c	Theoretical threshold fluence for bubble generation
F_s	Irradiated surface area
I_0	Light intensity of the excitation beam
I	Light intensity after transmitting through a sample
I_{ac}	Intensity of the acoustic signal
I_r	Reflection intensity of acoustic signal
I_t	Transmission intensity of acoustic signal
k	Compressibility of the medium
L_p	Sound pressure level, decibels(dB)
p	Sound pressure
P_{ac}	Acoustic pressure response
P_r	Reflection sound pressure
P_t	Transmission sound pressure
p_A	Atmospheric pressure
$p_b(t)$	Pressure inside the bubble
$p_b(t)-p_A$	Positive contribution to the
R	Beam diameter
r_{12}	Reflectance factor form medium 1 to medium 2

t_{12}	Transmittance factor form medium 1 to medium 2
ΔT	Resulting temperature rise in the illuminated region
v	Particle velocity of sound
V_0	Original illuminated volume in the sample
V	Illuminated volume in the sample
ΔV	Resulting volume expansion in the illuminated region
$V(b)$	Volume of laser-induced nanobubbles
Z	Acoustic impedance or the impedance
α_{ac}	Attenuation coefficient of acoustic signal in a medium
β	Thermal expansion coefficient.
γ_w	Surface tension of water
δ	Optical penetration depth
ε	Extinction coefficient
κ	Account for the dielectric properties of the GNP
λ_{520nm}	Absorbance at 520 nm
λ_{532nm}	Absorbance at 650 nm
λ_{532nm}	Absorbance at 532 nm
μ_a	Absorption coefficient
υ_w	Kinematic viscosity
δ	Optical penetration depth
ρ	Density of liquid
ρ_w	Density of water
σ_{abs}	Absorption cross section of nanoparitcle

List of Acronyms

Ag NPs	Silver nanoparticles
B[a]P	Benzo[a]pyrene
BSA	Albumin from bovine serum
DLS	Dynamic light scattering
DMF	Dimethylformamide
EPA	U.S. Environmental Protection Agency
FITC	Fluorescein 5(6)-isothiocyanate
GNPs	Gold nanoparticles
GSH	Glutathione
GSH-GNPs	Glutathione-conjugated gold nanoparticles
HRS	Hyper-Rayleigh scattering
ICP/MS	Inductively coupled plasma/mass spectrometry
LINB	Laser-induced nanobubbles
LOD	Limit of detection
NLO	Nonlinear optics
NPs	Nanoparticles
NSET	Nanoparticle based fluorescence energy transfer
PA	Photoacoustic
PAS	Photoacoustic spectroscopy
PA-LINB	PA signal produced from LINB on GNPs
PBS	Phosphate buffered saline
PVDF	Polyvinylidenefluoride
SADC	Sodium acetate dicarboxylate
SERS	Surface enhanced Raman scattering
SHG	Second-harmonic generation
SPB	Surface plasmon band
SPR	Surface plasmon resonance
TEOS	Tetraethyl orthosilicate
THF	Tetrahydrofuran
TRITC	Tetramethylrhodamine-5-isothiocyanate

VI. References

[1] Daniel, M.-C.; Astruc, D., Gold Nanoparticles: Assembly, Supramolecular Chemistry, Quantum-Size-Related Properties, and Applications toward Biology, Catalysis, and Nanotechnology, *Chemical Reviews,* **2003,** *104*, 293-346.

[2] Antonii, F., *Panacea Aurea-Auro Potabile*. Bibliopolio Frobeniano: Hamburg, 1618.

[3] Kahn, R. L., *Serum Diagnosis for Syphilis, in Colloid Chemistry: Theoretical and Applied*. The Chemical Catalog Co.: New York, 1929; Vol. II, p 757.

[4] Hauser, E. A., Aurum Potabile, *Journal of Chemical Education,* **1952,** *29*, 456.

[5] Brown, D. H.; Smith, W. E., The Chemistry of the Gold Drugs Used in the Treatment of Rheumatoid Arthritis, *Chemical Society Reviews,* **1980,** *9*, 217-240.

[6] Kunckel, J., *Nützliche Observationes oder Anmerckungen, von den fixen und flüchtigen Saltzen, auro und argento potabili, spiritu mundi und dergleichen*. Schultze: Hamburg, 1676.

[7] Dictionnaire de Chymi, Lacombe: Paris, 1769.

[8] Graham, T., Liquid Diffusion Applied to Analysis, *Philosophical Transactions of the Royal Society,* **1861,** *151*, 183-224.

[9] Hyatt, A. D.; Eaton, B. T., *Immuno-Gold Electron Microscopy in Virus Diagnosis and Research*. CRC Press: Boca Raton, FL, USA, 1993.

[10] Turkevich, J.; Stevenson, P. C.; Hillier, J., A Study of the Nucleation and Growth Processes in the Synthesis of Colloidal Gold, *Discussions of the Faraday Society,* **1951,** *11*, 55-75.

[11] Frens, G., Controlled Nucleation for the Regulation of the Particle Size in Monodisperse Gold Suspensions, *Nature Physical Science,* **1973**, 20-22.

[12] Hayat, M. A., *Colloidal Gold: Principles, Methods, and Applications (Colloidal Gold: Principles, Methods & Application)*. Academic Press: New York, 1989.

[13] Schmid, G., *Clusters and Colloids: From Theory to Applications*. VCH Verlagsgesellschaft: Weinheim, 1994.

[14] Faraday, M., Experimental Relations of Gold (and other Metals) to Light, *Philosophical Transactions of the Royal Society,* **1857,** *147*, 145-181.

[15] Wang, Y., Nonlinear Optical Properties of Nanometer-Sized Semiconductor Clusters, *Accounts of Chemical Research,* **1991,** *24*, 133-139.

[16] Steigerwald, M. L.; Brus, L. E., Semiconductor Crystallites: A Class of Large Molecules, *Accounts of Chemical Research,* **1990,** *23*, 183-188.

[17] Weller, H., Quantized Semiconductor Particles: A Novel State of Matter for Materials Science, *Advanced Materials,* **1993,** *5*, 88-95.

[18] Henglein, A., Small-Particle Research: Physicochemical Properties of Extremely Small Colloidal Metal and Semiconductor Particles, *Chemical Reviews,* **1989,** *89*, 1861-1873.

[19] Storhoff, J. J.; Mirkin, C. A., Programmed Materials Synthesis with DNA, *Chemical Reviews,* **1999,** *99*, 1849-1862.

[20] Haynes, C. L.; Van Duyne, R. P., Nanosphere Lithography: A Versatile Nanofabrication Tool for Studies of Size-Dependent Nanoparticle Optics, *The Journal of Physical Chemistry B,* **2001,** *105*, 5599-5611.

[21] Xia, Y.; Yang, P.; Sun, Y.; Wu, Y.; Mayers, B.; Gates, B.; Yin, Y.; Kim, F.; Yan, H., One-Dimensional Nanostructures: Synthesis, Characterization, and Applications, *Advanced Materials,* **2003,** *15*, 353-389.

[22] Murphy, C. J.; Sau, T. K.; Gole, A. M.; Orendorff, C. J.; Gao, J.; Gou, L.; Hunyadi, S. E.; Li, T., Anisotropic Metal Nanoparticles: Synthesis, Assembly, and Optical Applications, *The Journal of Physical Chemistry B,* **2005,** *109*, 13857-13870.

[23] Pérez-Juste, J.; Pastoriza-Santos, I.; Liz-Marzán, L. M.; Mulvaney, P., Gold Nanorods: Synthesis, Characterization and Applications, *Coordination Chemistry Reviews,* **2005,** *249*, 1870-1901.

[24] Burda, C.; Chen, X.; Narayanan, R.; El-Sayed, M. A., Chemistry and Properties of Nanocrystals of Different Shapes, *Chemical Reviews,* **2005,** *105*, 1025-1102.

[25] Pileni, M. P., Control of the Size and Shape of Inorganic Nanocrystals at Various Scales from Nano to Macrodomains, *The Journal of Physical Chemistry C,* **2007,** *111*, 9019-9038.

[26] Wang, H.; Brandl, D. W.; Nordlander, P.; Halas, N. J., Plasmonic Nanostructures: Artificial Molecules, *Accounts of Chemical Research,* **2006,** *40*, 53-62.

[27] Schwartzberg, A. M.; Zhang, J. Z., Novel Optical Properties and Emerging

Applications of Metal Nanostructures, *The Journal of Physical Chemistry C,* **2008,** *112*, 10323-10337.

[28] Rosi, N. L.; Mirkin, C. A., Nanostructures in Biodiagnostics, *Chemical Reviews,* **2005,** *105*, 1547-1562.

[29] Cheng, M. M.-C.; Cuda, G.; Bunimovich, Y. L.; Gaspari, M.; Heath, J. R.; Hill, H. D.; Mirkin, C. A.; Nijdam, A. J.; Terracciano, R.; Thundat, T.; Ferrari, M., Nanotechnologies for Biomolecular Detection and Medical Diagnostics, *Current Opinion in Chemical Biology,* **2006,** *10*, 11-19.

[30] Willets, K. A.; Van Duyne, R. P., Localized Surface Plasmon Resonance Spectroscopy and Sensing, *Annual Review of Physical Chemistry,* **2007,** *58*, 267-297.

[31] Schultz, D. A., Plasmon Resonant Particles for Biological Detection, *Current Opinion in Biotechnology,* **2003,** *14*, 13-22.

[32] Nicewarner-Peña, S. R.; Freeman, R. G.; Reiss, B. D.; He, L.; Peña, D. J.; Walton, I. D.; Cromer, R.; Keating, C. D.; Natan, M. J., Submicrometer Metallic Barcodes, *Science,* **2001,** *294*, 137-141.

[33] Raschke, G.; Kowarik, S.; Franzl, T.; Sönnichsen, C.; Klar, T. A.; Feldmann, J.; Nichtl, A.; Kürzinger, K., Biomolecular Recognition Based on Single Gold Nanoparticle Light Scattering, *Nano Letters,* **2003,** *3*, 935-938.

[34] Nehl, C. L.; Liao, H.; Hafner, J. H., Optical Properties of Star-Shaped Gold Nanoparticles, *Nano Letters,* **2006,** *6*, 683-688.

[35] Bukasov, R.; Shumaker-Parry, J. S., Highly Tunable Infrared Extinction Properties of Gold Nanocrescents, *Nano Letters,* **2007,** *7*, 1113-1118.

[36] Henzie, J.; Lee, M. H.; Odom, T. W., Multiscale Patterning of Plasmonic Metamaterials, *Nature Nanotechnology,* **2007,** *2*, 549-554.

[37] Lu, Y.; Liu, G. L.; Kim, J.; Mejia, Y. X.; Lee, L. P., Nanophotonic Crescent Moon Structures with Sharp Edge for Ultrasensitive Biomolecular Detection by Local Electromagnetic Field Enhancement Effect, *Nano Letters,* **2004,** *5*, 119-124.

[38] Bradley, J. S., *In Clusters and Colloids*. Schmid, G., Ed. VCH: Weinheim, 1994.

[39] Brown, K. R.; Natan, M. J., Hydroxylamine Seeding of Colloidal Au Nanoparticles in Solution and on Surfaces, *Langmuir,* **1998,** *14*, 726-728.

[40] Jana, N. R.; Gearheart, L.; Murphy, C. J., Evidence for Seed-Mediated Nucleation in the Chemical Reduction of Gold Salts to Gold Nanoparticles, *Chemistry of Materials,* **2001,** *13*, 2313-2322.

[41] Sau, T.; Pal, A.; Jana, N. R.; Wang, Z. L.; Pal, T., Size Controlled Synthesis of Gold Nanoparticles using Photochemically Prepared Seed Particles, *Journal of Nanoparticle Research,* **2001,** *3*, 257-261.

[42] Meltzer, S.; Resch, R.; Koel, B. E.; Thompson, M. E.; Madhukar, A.; Requicha, A. A. G.; Will, P., Fabrication of Nanostructures by Hydroxylamine Seeding of Gold Nanoparticle Templates, *Langmuir,* **2001,** *17*, 1713-1718.

[43] Carrot, G.; Valmalette, J. C.; Plummer, C. J. G.; Scholz, S. M.; Dutta, J.; Hofmann, H.; Hilborn, J. G., Gold Nanoparticle Synthesis in Graft Copolymer Micelles, *Colloid & Polymer Science,* **1998,** *276*, 853-859.

[44] Brown, K. R.; Walter, D. G.; Natan, M. J., Seeding of Colloidal Au Nanoparticle Solutions. 2. Improved Control of Particle Size and Shape, *Chemistry of Materials,* **1999,** *12*, 306-313.

[45] Stremsdoerfer, G.; Perrot, H.; Martin, J. R.; Clechet, P., Autocatalytic Deposition of Gold and Palladium onto n-GaAs in Acidic Media, *Journal of The Electrochemical Society,* **1988,** *135*, 2881-2886.

[46] Sun, C.-F.; Hu, C.-L.; Xu, X.; Ling, J.-B.; Hu, T.; Kong, F.; Long, X.-F.; Mao, J.-G., $BaNbO(IO_3)_5$: A New Polar Material with a Very Large SHG Response, *Journal of the American Chemical Society,* **2009,** *131*, 9486-9487.

[47] Ray, P. C., Size and Shape Dependent Second Order Nonlinear Optical Properties of Nanomaterials and Their Application in Biological and Chemical Sensing, *Chemical Reviews,* **2010,** *110*, 5332-5365.

[48] Ghosh, S. K.; Pal, T., Interparticle Coupling Effect on the Surface Plasmon Resonance of Gold Nanoparticles: From Theory to Applications, *Chemical Reviews,* **2007,** *107*, 4797-4862.

[49] Stewart, M. E.; Anderton, C. R.; Thompson, L. B.; Maria, J.; Gray, S. K.; Rogers, J. A.; Nuzzo, R. G., Nanostructured Plasmonic Sensors, *Chemical Reviews,* **2008,** *108*, 494-521.

[50] Murray, R. W., Nanoelectrochemistry: Metal Nanoparticles, Nanoelectrodes, and Nanopores, *Chemical Reviews,* **2008,** *108*, 2688-2720.

[51] Daniel, M.-C.; Astruc, D., Gold Nanoparticles: Assembly, Supramolecular Chemistry, Quantum-Size-Related Properties, and Applications toward Biology, Catalysis, and Nanotechnology, *Chemical Reviews,* **2003,** *104*, 293-346.

[52] Sassolas, A.; Leca-Bouvier, B. D.; Blum, L. J., DNA Biosensors and Microarrays, *Chemical Reviews,* **2007,** *108*, 109-139.

[53] Griffin, J.; Singh, A. K.; Senapati, D.; Rhodes, P.; Mitchell, K.; Robinson, B.; Yu, E.; Ray, P. C., Size- and Distance-Dependent Nanoparticle Surface-Energy Transfer (NSET) Method for Selective Sensing of Hepatitis C Virus RNA, *Chemistry – A European Journal,* **2009,** *15*, 342-351.

[54] LaFratta, C. N.; Walt, D. R., Very High Density Sensing Arrays, *Chemical Reviews,* **2008,** *108*, 614-637.

[55] Li, D.; Song, S.; Fan, C., Target-Responsive Structural Switching for Nucleic Acid-Based Sensors, *Accounts of Chemical Research,* **2010,** *43*, 631-641.

[56] Griffin, J.; Ray, P. C., Gold Nanoparticle Based NSET For Monitoring Mg^{2+} Dependent RNA Folding, *The Journal of Physical Chemistry B,* **2008,** *112*, 11198-11201.

[57] Friedrich, H.; de Jongh, P. E.; Verkleij, A. J.; de Jong, K. P., Electron Tomography for Heterogeneous Catalysts and Related Nanostructured Materials, *Chemical Reviews,* **2009,** *109*, 1613-1629.

[58] Liu, J.; Cao, Z.; Lu, Y., Functional Nucleic Acid Sensors, *Chemical Reviews,* **2009,** *109*, 1948-1998.

[59] Kumbhar, A. S.; Kinnan, M. K.; Chumanov, G., Multipole Plasmon Resonances of Submicron Silver Particles, *Journal of the American Chemical Society,* **2005,** *127*, 12444-12445.

[60] Darbha, G. K.; Ray, A.; Ray, P. C., Gold Nanoparticle-Based Miniaturized Nanomaterial Surface Energy Transfer Probe for Rapid and Ultrasensitive Detection of Mercury in Soil, Water, and Fish, *ACS Nano,* **2007,** *1*, 208-214.

[61] Wang, H.; Brandl, D. W.; Nordlander, P.; Halas, N. J., Plasmonic Nanostructures: Artificial Molecules, *Accounts of Chemical Research,* **2006,** *40*, 53-62.

[62] Lim, S. I.; Zhong, C.-J., Molecularly Mediated Processing and Assembly of Nanoparticles: Exploring the Interparticle Interactions and Structures, *Accounts of Chemical Research,* **2009,** *42*, 798-808.

[63] Jain, P. K.; Huang, X.; El-Sayed, I. H.; El-Sayed, M. A., Noble Metals on the Nanoscale: Optical and Photothermal Properties and Some Applications in Imaging, Sensing, Biology, and Medicine, *Accounts of Chemical Research,* **2008,** *41*, 1578-1586.

[64] Jun, Y.-W.; Seo, J.-W.; Cheon, J., Nanoscaling Laws of Magnetic Nanoparticles and Their Applicabilities in Biomedical Sciences, *Accounts of Chemical Research,* **2008,** *41*, 179-189.

[65] Dasary, S. S. R.; Singh, A. K.; Senapati, D.; Yu, H.; Ray, P. C., Gold Nanoparticle Based Label-Free SERS Probe for Ultrasensitive and Selective Detection of Trinitrotoluene, *Journal of the American Chemical Society,* **2009,** *131*, 13806-13812.

[66] Camden, J. P.; Dieringer, J. A.; Zhao, J.; Van Duyne, R. P., Controlled Plasmonic Nanostructures for Surface-Enhanced Spectroscopy and Sensing, *Accounts of Chemical Research,* **2008,** *41*, 1653-1661.

[67] Mulder, W. J. M.; Strijkers, G. J.; van Tilborg, G. A. F.; Cormode, D. P.; Fayad, Z. A.; Nicolay, K., Nanoparticulate Assemblies of Amphiphiles and Diagnostically Active Materials for Multimodality Imaging, *Accounts of Chemical Research,* **2009,** *42*, 904-914.

[68] Takeuchi, Y.; Ida, T.; Kimura, K., Colloidal Stability of Gold Nanoparticles in 2-Propanol under Laser Irradiation, *The Journal of Physical Chemistry B,* **1997,** *101*, 1322-1327.

[69] Alvarez, M. M.; Khoury, J. T.; Schaaff, T. G.; Shafigullin, M. N.; Vezmar, I.; Whetten, R. L., Optical Absorption Spectra of Nanocrystal Gold Molecules, *The Journal of Physical Chemistry B,* **1997,** *101*, 3706-3712.

[70] Kreibig, U.; Vollmer, M., *Optical Properties of Metal Clusters*. Springer-Verlag: Berlin/Heidelberg, 1995.

[71] James, T. H., *The Theory of the Photographic Process*. Macmillan Pub Co: 1977.

[72] Logunov, S. L.; Ahmadi, T. S.; El-Sayed, M. A.; Khoury, J. T.; Whetten, R. L., Electron Dynamics of Passivated Gold Nanocrystals Probed by Subpicosecond Transient Absorption Spectroscopy, *The Journal of Physical Chemistry B,* **1997,** *101*, 3713-3719.

[73] Schaaff, T. G.; Shafigullin, M. N.; Khoury, J. T.; Vezmar, I.; Whetten, R. L.; Cullen, W. G.; First, P. N.; Gutiérrez-Wing, C.; Ascensio, J.; Jose-Yacamán, M. J., Isolation of Smaller Nanocrystal Au Molecules: Robust Quantum Effects in Optical Spectra, *The Journal of Physical Chemistry B,* **1997,** *101*, 7885-7891.

[74] Zaitoun, M. A.; Mason, W. R.; Lin, C. T., Magnetic Circular Dichroism Spectra for Colloidal Gold Nanoparticles in Xerogels at 5.5 K, *The Journal of Physical Chemistry B,* **2001,** *105*, 6780-6784.

[75] Melinger, J. S.; Kleiman, V. D.; McMorrow, D.; Gröhn, F.; Bauer, B. J.; Amis, E., Ultrafast Dynamics of Gold-Based Nanocomposite Materials, *The Journal of Physical Chemistry A,* **2003,** *107*, 3424-3431.

[76] Griffin, J.; Singh, A. K.; Senapati, D.; Lee, E.; Gaylor, K.; Jones-Boone, J.; Ray, P. C., Sequence-Specific HCV RNA Quantification Using the Size-Dependent Nonlinear Optical Properties of Gold Nanoparticles, *Small,* **2009,** *5*, 839-845.

[77] Darbha, G. K.; Rai, U. S.; Singh, A. K.; Ray, P. C., Gold-Nanorod-Based Sensing of Sequence Specific HIV-1 Virus DNA by Using Hyper-Rayleigh Scattering Spectroscopy, *Chemistry – A European Journal,* **2008,** *14*, 3896-3903.

[78] Templeton, A. C.; Pietron, J. J.; Murray, R. W.; Mulvaney, P., Solvent Refractive Index and Core Charge Influences on the Surface Plasmon Absorbance of Alkanethiolate Monolayer-Protected Gold Clusters, *The Journal of Physical Chemistry B,* **1999,** *104*, 564-570.

[79] Link, S.; El-Sayed, M. A., Size and Temperature Dependence of the Plasmon Absorption of Colloidal Gold Nanoparticles, *The Journal of Physical Chemistry B,* **1999,** *103*, 4212-4217.

[80] Itoh, T.; Asahi, T.; Masuhara, H., Femtosecond Light Scattering Spectroscopy of Single Gold Nanoparticles, *Applied Physics Letters,* **2001,** *79*, 1667.

[81] Su, K. H.; Wei, Q. H.; Zhang, X.; Mock, J. J.; Smith, D. R.; Schultz, S., Interparticle Coupling Effects on Plasmon Resonances of Nanogold Particles, *Nano Letters,* **2003,** *3*, 1087-1090.

[82] Link, S.; Mohamed, M. B.; El-Sayed, M. A., Simulation of the Optical Absorption Spectra of Gold Nanorods as a Function of Their Aspect Ratio and the Effect of the Medium Dielectric Constant, *The Journal of Physical Chemistry B,* **1999,** *103*, 3073-3077.

[83] Yan, B.; Yang; Wang, Y., Comment on "Simulation of the Optical Absorption Spectra of Gold Nanorods as a Function of Their Aspect Ratio and the Effect of the Medium Dielectric Constant", *The Journal of Physical Chemistry B,* **2003,** *107*, 9159-9159.

[84] Swanson, N. L.; Billard, B. D., Optimization of Extinction from Surface Plasmon

Resonances of Gold Nanoparticles, *Nanotechnology,* **2003,** *14*, 353.

[85] Chandrasekharan, N.; Kamat, P. V.; Hu, J.; Jones, G., Dye-Capped Gold Nanoclusters: Photoinduced Morphological Changes in Gold/Rhodamine 6G Nanoassemblies, *The Journal of Physical Chemistry B,* **2000,** *104*, 11103-11109.

[86] Agarwal, G. S.; Jha, S. S., Theory of Second Harmonic Generation at A Metal Surface With Surface Plasmon Excitation, *Solid State Communications,* **1982,** *41*, 499-501.

[87] Hua, X. M.; Gersten, J. I., Theory of Second-Harmonic Generation by Small Metal Spheres, *Physical Review B,* **1986,** *33*, 3756-3764.

[88] Dadap, J. I.; Shan, J.; Eisenthal, K. B.; Heinz, T. F., Second-Harmonic Rayleigh Scattering from a Sphere of Centrosymmetric Material, *Physical Review Letters,* **1999,** *83*, 4045.

[89] Novak, J. P.; Brousseau, L. C.; Vance, F. W.; Johnson, R. C.; Lemon, B. I.; Hupp, J. T.; Feldheim, D. L., Nonlinear Optical Properties of Molecularly Bridged Gold Nanoparticle Arrays, *Journal of the American Chemical Society,* **2000,** *122*, 12029-12030.

[90] Chandra, M.; Indi, S. S.; Das, P. K., First Hyperpolarizabilities of Unprotected and Polymer Protected Copper Nanoparticles Prepared by Laser Ablation, *Chemical Physics Letters,* **2006,** *422*, 262-266.

[91] Kneipp, J.; Kneipp, H.; Wittig, B.; Kneipp, K., One- and Two-Photon Excited Optical pH Probing for Cells Using Surface-Enhanced Raman and Hyper-Raman Nanosensors, *Nano Letters,* **2007,** *7*, 2819-2823.

[92] Raman, C. V.; Krishnan, K. S., Polarisation of Scattered Light-quanta, *Nature,* **1928,** *122*.

[93] Haynes, C. L.; McFarland, A. D.; Duyne, R. P. V., Surface-Enhanced Raman Spectroscopy, *Analytical Chemistry,* **2005,** *77*, 338 A-346 A.

[94] Van Labeke, D.; Jacon, M.; Bernard, L., The Influence of the Symmetry of the Vibrations on Resonance Raman Intensities, *Chemical Physics Letters,* **1974,** *27*, 123-125.

[95] Jeanmaire, D. L.; Van Duyne, R. P., Surface Raman Spectroelectrochemistry: Part I. Heterocyclic, Aromatic, and Aliphatic Amines Adsorbed on the Anodized Silver Electrode, *Journal of Electroanalytical Chemistry and Interfacial Electrochemistry,*

1977, *84*, 1-20.

[96] Albrecht, M. G.; Creighton, J. A., Anomalously Intense Raman Spectra of Pyridine at A Silver Electrode, *Journal of the American Chemical Society,* **1977,** *99*, 5215-5217.

[97] Vance, F. W.; Lemon, B. I.; Hupp, J. T., Enormous Hyper-Rayleigh Scattering from Nanocrystalline Gold Particle Suspensions, *The Journal of Physical Chemistry B,* **1998,** *102*, 10091-10093.

[98] Galletto, P.; Brevet, P. F.; Girault, H. H.; Antoine, R.; Broyer, M., Enhancement of the Second Harmonic Response by Adsorbates on Gold Colloids: The Effect of Aggregation, *The Journal of Physical Chemistry B,* **1999,** *103*, 8706-8710.

[99] Das, S.; Gersten, J. I., Electronic Raman Scattering from Spherical Particles, *Physical Review B,* **1988,** *37*, 6063.

[100] Johnson, R. C.; Li, J.; Hupp, J. T.; Schatz, G. C., Hyper-Rayleigh Scattering Studies of Silver, Copper, and Platinum Nanoparticle Suspensions, *Chemical Physics Letters,* **2002,** *356*, 534-540.

[101] Chandra, M.; Das, P. K., "Small-particle limit" in the Second Harmonic Generation from Noble Metal Nanoparticles, *Chemical Physics,* **2009,** *358*, 203-208.

[102] Campion, A.; Kambhampati, P., Surface-Enhanced Raman Scattering, *Chemical Society Reviews,* **1998,** *27*, 241-250.

[103] Schatz, G. C.; Van-Duyne, R. P.; Chalmers, J. M.; Griffiths, P. R., *Handbook of Vibrational Spectroscopy*. John Wiley & Sons: New York, 2002; Vol. 1, p 759-774.

[104] Moskovits, M.; DiLella, D. P.; Maynard, K. J., Surface Raman Spectroscopy of A Number of Cyclic Aromatic Molecules Adsorbed on Silver: Selection Rules and Molecular Reorientation, *Langmuir,* **1988,** *4*, 67-76.

[105] Whitney, A. V.; Elam, J. W.; Zou, S.; Zinovev, A. V.; Stair, P. C.; Schatz, G. C.; Van Duyne, R. P., Localized Surface Plasmon Resonance Nanosensor: A High-Resolution Distance-Dependence Study Using Atomic Layer Deposition, *The Journal of Physical Chemistry B,* **2005,** *109*, 20522-20528.

[106] Whitney, A. V.; Elam, J. W.; Zou, S.; Zinovev, A. V.; Stair, P. C.; Schatz, G. C.; Van Duyne, R. P., Localized Surface Plasmon Resonance Nanosensor: A High-Resolution Distance-Dependence Study Using Atomic Layer Deposition, *The Journal of Physical Chemistry B,* **2005,** *109*, 20522-20528.

[107] Pettinger, B.; Domke, K. F.; Zhang, D.; Schuster, R.; Ertl, G., Direct Monitoring of Plasmon Resonances in A Tip-Surface Gap of Varying Width, *Physical Review B,* **2007,** *76*, 113409.

[108] Kim, Y.; Johnson, R. C.; Hupp, J. T., Gold Nanoparticle-Based Sensing of "Spectroscopically Silent" Heavy Metal Ions, *Nano Letters,* **2001,** *1*, 165-167.

[109] Segets, D.; Martinez Tomalino, L.; Gradl, J.; Peukert, W., Real-Time Monitoring of the Nucleation and Growth of ZnO Nanoparticles Using an Optical Hyper-Rayleigh Scattering Method, *The Journal of Physical Chemistry C,* **2009,** *113*, 11995-12001.

[110] Neely, A.; Perry, C.; Varisli, B.; Singh, A. K.; Arbneshi, T.; Senapati, D.; Kalluri, J. R.; Ray, P. C., Ultrasensitive and Highly Selective Detection of Alzheimer's Disease Biomarker Using Two-Photon Rayleigh Scattering Properties of Gold Nanoparticle, *ACS Nano,* **2009,** *3*, 2834-2840.

[111] Wang, G.; Sun, W., Optical Limiting of Gold Nanoparticle Aggregates Induced by Electrolytes, *The Journal of Physical Chemistry B,* **2006,** *110*, 20901-20905.

[112] Duboisset, J.; Russier-Antoine, I.; Benichou, E.; Bachelier, G.; Jonin, C.; Brevet, P. F., Single Metallic Nanoparticle Sensitivity with Hyper Rayleigh Scattering, *The Journal of Physical Chemistry C,* **2009,** *113*, 13477-13481.

[113] Singh, A. K.; Senapati, D.; Wang, S.; Griffin, J.; Neely, A.; Candice, P.; Naylor, K. M.; Varisli, B.; Kalluri, J. R.; Ray, P. C., Gold Nanorod Based Selective Identification of Escherichia coli Bacteria Using Two-Photon Rayleigh Scattering Spectroscopy, *ACS Nano,* **2009,** *3*, 1906-1912.

[114] Ray, P. C., Diagnostics of Single Base-Mismatch DNA Hybridization on Gold Nanoparticles by Using the Hyper-Rayleigh Scattering Technique, *Angewandte Chemie International Edition,* **2006,** *45*, 1151-1154.

[115] Moran, A. M.; Sung, J.; Hicks, E. M.; Van Duyne, R. P.; Spears, K. G., Second Harmonic Excitation Spectroscopy of Silver Nanoparticle Arrays, *The Journal of Physical Chemistry B,* **2005,** *109*, 4501-4506.

[116] Liu, Z. D.; Li, Y. F.; Ling, J.; Huang, C. Z., A Localized Surface Plasmon Resonance Light-Scattering Assay of Mercury (II) on the Basis of Hg^{2+}-DNA Complex Induced Aggregation of Gold Nanoparticles, *Environmental Science & Technology,* **2009,** *43*, 5022-5027.

[117] Leuvering, J. H.; Thal, P. J.; van der Waart, M.; Schuurs, A. H., Sol Particle Immunoassay (SPIA), *Journal of Immunoassay,* **1980,** *1*, 77-91.

[118] Nam, J. M.; Thaxton, C. S.; Mirkin, C. A., Nanoparticle-based Bio-bar Codes for the Ultrasensitive Detection of Proteins, *Science,* **2003,** *301*, 1884-1990.

[119] Elghanian, R.; Storhoff, J. J.; Mucic, R. C.; Letsinger, R. L.; Mirkin, C. A., Selective Colorimetric Detection of Polynucleotides Based on the Distance-Dependent Optical Properties of Gold Nanoparticles, *Science,* **1997,** *277*, 1078-1081.

[120] Mirkin, C. A.; Letsinger, R. L.; Mucic, R. C.; Storhoff, J. J., A DNA-based method for rationally assembling nanoparticles into macroscopic materials, *Nature,* **1996,** *382*, 607-609.

[121] Dusemund, B.; Hoffmann, A.; Salzmann, T.; Kreibig, U.; Schmid, G., Cluster Matter: the Transition of Optical Elastic Scattering to Regular Reflection, *Zeitschrift für Physik D Atoms, Molecules and Clusters,* **1991,** *20*, 305-308.

[122] Cobbe, S.; Connolly, S.; Ryan, D.; Nagle, L.; Eritja, R.; Fitzmaurice, D., DNA-Controlled Assembly of Protein-Modified Gold Nanocrystals, *The Journal of Physical Chemistry B,* **2002,** *107*, 470-477.

[123] Park, S.-J.; Lazarides, A. A.; Mirkin, C. A.; Letsinger, R. L., Directed Assembly of Periodic Materials from Protein and Oligonucleotide-Modified Nanoparticle Building Blocks, *Angewandte Chemie International Edition,* **2001,** *40*, 2909-2912.

[124] Hirsch, L. R.; Jackson, J. B.; Lee, A.; Halas, N. J.; West, J. L., A Whole Blood Immunoassay Using Gold Nanoshells, *Analytical Chemistry,* **2003,** *75*, 2377-2381.

[125] Thanh, N. T. K.; Rosenzweig, Z., Development of an Aggregation-Based Immunoassay for Anti-Protein A Using Gold Nanoparticles, *Analytical Chemistry,* **2002,** *74*, 1624-1628.

[126] Norsten, T. B.; Frankamp, B. L.; Rotello, V. M., Metal Directed Assembly of Terpyridine-Functionalized Gold Nanoparticles, *Nano Letters,* **2002,** *2*, 1345-1348.

[127] Lin, S.-Y.; Liu, S.-W.; Lin, C.-M.; Chen, C.-h., Recognition of Potassium Ion in Water by 15-Crown-5 Functionalized Gold Nanoparticles, *Analytical Chemistry,* **2001,** *74*, 330-335.

[128] Obare, S. O.; Hollowell, R. E.; Murphy, C. J., Sensing Strategy for Lithium Ion Based on Gold Nanoparticles, *Langmuir,* **2002,** *18*, 10407-10410.

[129] Liu, J.; Lu, Y., A Colorimetric Lead Biosensor Using DNAzyme-Directed Assembly of Gold Nanoparticles, *Journal of the American Chemical Society,* **2003,** *125*, 6642-6643.

[130] Nam, J.-M.; Stoeva, S. I.; Mirkin, C. A., Bio-Bar-Code-Based DNA Detection with PCR-like Sensitivity, *Journal of the American Chemical Society,* **2004,** *126*, 5932-5933.

[131] Yguerabide, J.; Yguerabide, E. E., Light-Scattering Submicroscopic Particles as Highly Fluorescent Analogs and Their Use as Tracer Labels in Clinical and Biological Applications: I. Theory, *Analytical Biochemistry,* **1998,** *262*, 137-156.

[132] Jain, P. K.; Lee, K. S.; El-Sayed, I. H.; El-Sayed, M. A., Calculated Absorption and Scattering Properties of Gold Nanoparticles of Different Size, Shape, and Composition: Applications in Biological Imaging and Biomedicine, *The Journal of Physical Chemistry B,* **2006,** *110*, 7238-7248.

[133] Du, B.-A.; Li, Z.-P.; Liu, C.-H., One-Step Homogeneous Detection of DNA Hybridization with Gold Nanoparticle Probes by Using a Linear Light-Scattering Technique, *Angewandte Chemie International Edition,* **2006,** *45*, 8022-8025.

[134] Russier-Antoine, I.; Huang, J.; Benichou, E.; Bachelier, G.; Jonin, C.; Brevet, P.-F., Hyper Rayleigh Scattering of Protein-Mediated Gold Nanoparticles Aggregates, *Chemical Physics Letters,* **2008,** *450*, 345-349.

[135] Xie, H.; Gill-Sharp, K. L.; O'Neal, D. P., Quantitative Estimation of Gold Nanoshell Concentrations in Whole Blood Using Dynamic Light Scattering, *Nanomedicine: Nanotechnology, Biology and Medicine,* **2007,** *3*, 89-94.

[136] Aslan, K.; Holley, P.; Davies, L.; Lakowicz, J. R.; Geddes, C. D., Angular-Ratiometric Plasmon-Resonance Based Light Scattering for Bioaffinity Sensing, *Journal of the American Chemical Society,* **2005,** *127*, 12115-12121.

[137] Dai, Q.; Liu, X.; Coutts, J.; Austin, L.; Huo, Q., A One-Step Highly Sensitive Method for DNA Detection Using Dynamic Light Scattering, *Journal of the American Chemical Society,* **2008,** *130*, 8138-8139.

[138] Jans, H.; Liu, X.; Austin, L.; Maes, G.; Huo, Q., Dynamic Light Scattering as a Powerful Tool for Gold Nanoparticle Bioconjugation and Biomolecular Binding Studies, *Analytical Chemistry,* **2009,** *81*, 9425-9432.

[139] Kalluri, Jhansi R.; Arbneshi, T.; Afrin Khan, S.; Neely, A.; Candice, P.; Varisli, B.; Washington, M.; McAfee, S.; Robinson, B.; Banerjee, S.; Singh, Anant K.; Senapati, D.; Ray, Paresh C., Use of Gold Nanoparticles in a Simple Colorimetric and Ultrasensitive Dynamic Light Scattering Assay: Selective Detection of Arsenic in Groundwater, *Angewandte Chemie International Edition,* **2009,** *48*, 9668-9671.

[140] Berne, B. J.; Pecora, R., *Dynamic Light Scattering*. John Wiley: New York, 1976.

[141] Clays, K.; Persoons, A., Hyper-Rayleigh Scattering in Solution, *Physical Review Letters,* **1991,** *66*, 2980-2983.

[142] *Surface-Enhanced Raman Scattering-Physics and Applications, Topics in Applied Physics, Kneipp, K.; Moskovits, M.; Kneipp, H. (Eds.)*. Springer-Verlag: Berlin/Heidelberg, 2006; Vol. 103.

[143] Shafer-Peltier, K. E.; Haynes, C. L.; Glucksberg, M. R.; Van Duyne, R. P., Toward a Glucose Biosensor Based on Surface-Enhanced Raman Scattering, *Journal of the American Chemical Society,* **2002,** *125*, 588-593.

[144] Tao, A.; Kim, F.; Hess, C.; Goldberger, J.; He, R.; Sun, Y.; Xia, Y.; Yang, P., Langmuir-Blodgett Silver Nanowire Monolayers for Molecular Sensing Using Surface-Enhanced Raman Spectroscopy, *Nano Letters,* **2003,** *3*, 1229-1233.

[145] Sanles-Sobrido, M.; Rodriguez-Lorenzo, L.; Lorenzo-Abalde, S.; Gonzalez-Fernandez, A.; Correa-Duarte, M. A.; Alvarez-Puebla, R. A.; Liz-Marzan, L. M., Label-free SERS Detection of Relevant Bioanalytes on Silver-coated Carbon Nanotubes: the Case of Cocaine, *Nanoscale,* **2009,** *1*, 153-158.

[146] Cho, H.; Lee, B.; Liu, G. L.; Agarwal, A.; Lee, L. P., Label-free and highly sensitive biomolecular detection using SERS and electrokinetic preconcentration, *Lab on a Chip,* **2009,** *9*, 3360-3363.

[147] Cao, Y. C.; Jin, R.; Mirkin, C. A., Nanoparticles with Raman Spectroscopic Fingerprints for DNA and RNA Detection, *Science,* **2002,** *297*, 1536-1540.

[148] Vo-Dinh, T.; Allain, L. R.; Stokes, D. L., Cancer Gene Detection Using Surface-Enhanced Raman Scattering (SERS), *Journal of Raman Spectroscopy,* **2002,** *33*, 511-516.

[149] Kim, J.-H.; Kim, J.-S.; Choi, H.; Lee, S.-M.; Jun, B.-H.; Yu, K.-N.; Kuk, E.; Kim, Y.-K.; Jeong, D. H.; Cho, M.-H.; Lee, Y.-S., Nanoparticle Probes with Surface Enhanced Raman Spectroscopic Tags for Cellular Cancer Targeting, *Analytical Chemistry,* **2006,** *78*, 6967-6973.

[150] Wang, C.; Chen, Y.; Wang, T.; Ma, Z.; Su, Z., Monodispersed Gold Nanorod-Embedded Silica Particles as Novel Raman Labels for Biosensing, *Advanced Functional Materials,* **2008,** *18*, 355-361.

[151] Küstner, B.; Gellner, M.; Schütz, M.; Schöppler, F.; Marx, A.; Ströbel, P.; Adam,

P.; Schmuck, C.; Schlücker, S., SERS Labels for Red Laser Excitation: Silica-Encapsulated SAMs on Tunable Gold/Silver Nanoshells, *Angewandte Chemie International Edition,* **2009,** *48*, 1950-1953.

[152] Bell, A. G., Selenium and the Photophone, *Nature,* **1880,** *22*, 500-503.

[153] Bell, A. G., On the Production and Reproduction of Sound by Light, *American Journal of Science,* **1881,** *13*, 156-158.

[154] Tyndall, J., Action of an Intermittent Beam of Radiant Heat upon Gaseous Matter, *Proceedings of the Royal Society of London,* **1881,** *31*, 307-317.

[155] Roentgen, W. C., On Tones Produced by the Intermittent Irradiation of a Gas, *Philosophical Magazine,* **1881,** *11*, 308-311.

[156] Rosencwaig, A., Theory of the Photoacoustic Effect with Solids, *Journal of Applied Physics,* **1976,** *47*, 64.

[157] Rosencwaig, A., *Photoacoustic and Photoaocustic Spctroscopy*. John Wiley & Sons: New York, 1980.

[158] McDonald, F., Generalized Theory of the Photoacoustic Effect, *Journal of Applied Physics,* **1978,** *49*, 2313.

[159] McDonald, F., Theory of Photoacoustic Signal Generation for Optimized Photoacoustic Cells, *Journal of Applied Physics,* **1981,** *52*, 1462.

[160] Bar-Cohen, Y.; Xue, T.; Lih, S.-S., *Polymer Piezoelectric Transducers for Ultrasonic NDE*. NDTnet 1, Paper 9 (http://www.ndt.net/): 1996.

[161] Shen, Y. C.; Zhao, Y. Z.; Zhang, S. Y.; Lu, Z. H., A New Optical Method for Detecting Laser-generated Acoustic Pulse in Solution, *Analytical Sciences,* **2001,** *110*, s458-s461.

[162] Kruger, R.; Kiser, J. W.; Romilly, A.; Schmidt, P., Thermoacoustic CT of the Breast: Pilot Study Observations, *Proceedings of SPIE,* **2001,** *4256*, 1.

[163] Almond, D. P.; Patel, P. M., *Photothermal Science and Techniques (Chapman & Hall Series in Accounting and Finance)*. Springer-Verlag: Berlin/Heidelberg, 1996.

[164] Tam, A. C., Photothermal Spectroscopy as A Sensitive Spectroscopic Tool, *Proceedings of SPIE,* **1991,** *1435*, 114-127.

[165] Patel, C., Optoacoustic Spectroscopy of Liquids, *Applied Physics Letters,* **1979,** *34*, 467.

[166] Patel, C. K. N.; Tam, A. C., Pulsed Optoacoustic Spectroscopy of Condensed Matter, *Reviews of Modern Physics,* **1981,** *53*, 517.

[167] Welsch, E.; Ristau, D., Photothermal Measurements on Optical Thin Films, *Applied Optics,* **1995,** *34*, 7239-7253.

[168] Tam, A., Optimization of Optoacoustic Cell for Depth Profiling Studies of Semiconductor Surfaces, *Applied Physics Letters,* **1980,** *36*, 471.

[169] Norris, P.; Caffrey, A.; Stevens, R.; Klopf, J.; McLeskey, J.; Smith, A., Femtosecond Pump-probe Nondestructive Examination of Materials (invited), *Review of Scientific Instruments,* **2003,** *74*, 400.

[170] Cross, F. W.; Al-Dhahir, R. K.; Dyer, P. E.; MacRobert, A. J., Time-resolved Photoacoustic Studies of Vascular Tissue Ablation at Three Laser Wavelengths, *Applied Physics Letters,* **1987,** *50*, 1019.

[171] De Tommasi, A.; Occhiogrosso, M.; Vailati, G.; Baldassarre, L.; Cingolani, A., Evaluation of the Ar^+ Laser Thermal Effect in Rabbit Brain Tissue by Means of Optical Absorption Coefficients. Photoacoustic Measurements, *Acta Neurochirurgica,* **1986,** *79*, 139-144.

[172] Pilatou, M.; Kolkman, R.; Hondebrink, E.; Bolt, R.; de Mul, F., Photoacoustic Imaging of Blood Perfusion in Tissue and Phantoms, *Proceedings of SPIE,* **2001,** *4256*, 28.

[173] Kolkman, R. G. M.; Klaessens, J. H. G. M.; Hondebrink, E.; Hopman, J. C. W.; Steenbergen, W.; van Leeuwen, T. G.; Thijssen, J. M.; de Mul, F. F. M., Photoacoustic Monitoring and Imaging of Blood Vessel Size in Vivo, *Proceedings of SPIE,* **2003,** *4960*, 1-6.

[174] Oberheide, U.; Jansen, B.; Bruder, I.; Lubatschowski, H.; Welling, H.; Ertmer, W., Optoacoustic Online Control for Laser Cyclophotocoagulation, *Proceedings of SPIE,* **2001,** *4256*, 53-60.

[175] Larin, K. V.; Hartrumpf, O.; Larina, I. V.; Esenaliev, R. O., Comparison of Optoacoustic Tomography with Ultrasound and X-ray Imaging for Breast Cancer Detection, *Proceedings of SPIE,* **2001,** *4256*, 147-153.

[176] Beard, P. C., Photoacoustic Imaging of Blood Vessel Equivalent Phantoms,

Proceedings of SPIE, **2002,** *4618*, 54-62.

[177] Jeon, R., Depth Profilometric Case Studies in Caries Diagnostics of Human Teeth Using Modulated Laser Radiometry and Luminescence, *Review of Scientific Instruments,* **2003,** *74*, 380.

[178] Majaron, B.; Milner, T.; Nelson, J., Determination of Parameter for Dual-wavelength Pulsed Photothermal Profiling of Human Skin, *Review of Scientific Instruments,* **2003,** *74*, 387.

[179] Fujiwara, M.; Okuda, R.; Ozeki, M.; Asada, H.; Matsushita, T.; Muralidharan, S.; Freiser, H., Crystal Structure of 4,4'-Bis(4-chloro-1-phenyl-3-methyl-5-pyrazolonyl), *Analytical Sciences,* **2001,** *17*, 353-354.

[180] Beck, H. A.; Bozóki, Z.; Niessner, R., Screening of Pentachlorophenol-Contaminated Wood by Thermodesorption Sampling and Photoacoustic Detection, *Analytical Chemistry,* **2000,** *72*, 2171-2176.

[181] Sigrist, M., Trace Gas Monitoring by Laser Photoacoustic Spectroscopy and Related Techniques (plenary), *Review of Scientific Instruments,* **2003,** *74*, 486.

[182] Beck, H. A.; Niessner, R.; Haisch, C., Development and Characterization of a Mobile Photoacoustic Sensor for On-line Soot Emission Monitoring in Diesel Exhaust Gas, *Analytical and Bioanalytical Chemistry,* **2003,** *375*, 1136-1143.

[183] Schramm, D.; Sthel, M.; da Silva, M.; Carneiro, L.; Souza, A.; Vargas, H., Diesel Engines Gas Emissions Monitored by Photoacoustic Spectroscopy, *Review of Scientific Instruments,* **2003,** *74*, 513.

[184] Slezak, V.; Codnia, J.; Peuriot, A.; Santiago, G., Resonant Photoacoustic Detection of NO_2 Traces with a Q-switched Green Laser, *Review of Scientific Instruments,* **2003,** *74*, 516.

[185] da Silva, M. G.; Santos, E. O.; Sthel, M. S.; Cardoso, S. L.; Cavalli, A.; Monteiro, A. R.; de Oliveira, J. G.; Pereira, M. G.; Vargas, H., Effect of Heat Treatment on Ethylene and CO_2 Emissions Eates during Papaya (*Carica papaya* L.) Fruit Ripening, *Review of Scientific Instruments,* **2003,** *74*, 703.

[186] Altuzar, V., Atmospheric pollution profiles in Mexico City in two different seasons, *Review of Scientific Instruments,* **2003,** *74*, 500.

[187] Sawada, T.; Oda, S.; Shimizu, H.; Kamada, H., Laser-induced Photoacoustic Spectroscopy of Some Rare Earth Ions in Aqueous Solutions, *Analytical Chemistry,*

1979, *51*, 688-690.

[188] Kim, J.-I.; Stumpe, R.; Klenze, R., Laser-induced Photoacoustic Spectroscopy for the Speciation of Transuranic Elements in Natural Aquatic Systems, *Chemistry and Materials Science,* **1990,** *157*, 129-179.

[189] Fontes, A. S.; Bento, A. C.; Miranda, L. C. M.; Baesso, M. L., Thermal Lens Evaluation of the Presence of Adulterants in Brewed Coffee, *Analytical Sciences,* **2001,** *17*, s526-s529.

[190] Ponce-Parra, C.; Tomás, S. A.; Cruz-Orea, A.; López-Bueno, G.; Sanmartín, E.; Sánchez-Sinencio, F., Photoacoustic Monitoring of Water Vapour Permeability in Alkaline-cooked Corn Pericarp, *Analytical Sciences,* **2001,** *17*, s538-s540.

[191] Hu, C., Spherical Model of an Acoustical Wave Generated by Rapid Laser Heating in a Liquid, *Journal of the Acoustical Society of America,* **1969,** *46*, 728.

[192] Asshauer, T.; Rink, K.; Delacrétaz, G., Acoustic Transient Generation by Holmium-laser-induced Cavitation Bubbles, *Journal of Applied Physics,* **1994,** *76*, 5007.

[193] Sigrist, M., Laser Generation of Acoustic Waves in Liquids and Gases, *Journal of Applied Physics,* **1986,** *60*, R83.

[194] Sigrist, M., Laser-generated Stress Waves in Liquids, *Journal of the Acoustical Society of America,* **1978,** *64*, 1652.

[195] Brewer, R. G.; Rieckhoff, K. E., Stimulated Brillouin Scattering in Liquids, *Physical Review Letters,* **1964,** *13*, 334.

[196] Emmony, D. C., Interaction of IR Laser Radiation with Liquids, *Infrared Physics,* **1985,** *25*, 133-139.

[197] Tam, A. C., Applications of Photoacoustic Sensing Techniques, *Reviews of Modern Physics,* **1986,** *58*, 381.

[198] Boyd, R. W., *NonlinearOptics*. Academic Press: New York, 1992.

[199] Gojani, A. B.; Danehy, P. M.; Alderfer, D. W.; Saito, T.; Takayama, K., Development of Laser-induced Grating Spectroscopy for Underwater Temperature Measurement in Shock Wave Focusing Regions, *Proceedings of SPIE,* **2004,** *5251*, 313-322.

[200] Atkins, P. W., *Physikalische Chemie (Lehrbuch)*. Wiley-VCH: Weinheim, 1996.

[201] Schwedt, G., *Analytishce Chemie: Grundlagen, Methoden und Praxis*. Thieme-Verlag: Stuttgart, 1995.

[202] Gusev, V. Ė.; Karabutov, A. A., *Laser Optoacoustics*. AIP Press: New York, 1993.

[203] Kuttruff, H., *Physik und Technik des Ultraschalls*. Hirzel-Verlag: Stuttgart, 1988.

[204] Stöcker, H., *Taschenbuch der Physik*. Verlag Harri Deutsch: Thun, Frankfurt am Main, 1994.

[205] Duck, F. A., *Physical Properties of Tissue: a Comprehensive Reference Book*. Academic Press Inc.: San Diego, 1990.

[206] Kinney, J. B.; Staley, R. H., Applications of Photoacoustic Spectroscopy, *Annual Review of Materials Science,* **1982,** *12*, 295-321.

[207] Mandelis, A.; Peralta, S.; Thoen, J., Photoacoustic Frequency-domain Depth Profiling of Continuously Inhomogeneous Condensed Phases: Theory and Simulations for the Inverse Problem, *Journal of Applied Physics,* **1991,** *70*, 1761.

[208] Wang, L. V.; Wu, H.-i., *Biomedical Optics: Principle and Imaging*. John Wiley & Sons, Inc.: Hoboken, New Jersey, 2007.

[209] Thomas III, L. J.; Kelly, M. J.; Amer, N. M.; Kelly, M.; Amer, N., The Role of Buffer Gases in Optoacoustic Spectroscopy, *Applied Physics Letters,* **1978,** *32*, 736.

[210] Nodov, E., Optimization of Resonant Cell Design for Optoacoustic Gas Spectroscopy (H-type), *Applied Optics,* **1978,** *17*, 1110-1119.

[211] West, G.; Barrett, J.; Siebert, D.; Reddy, K., Photoacoustic Spectroscopy, *Review of Scientific Instruments,* **1983,** *54*, 797.

[212] Farrow, M. M.; Burnham, R. K.; Auzanneau, M.; Olsen, S. L.; Purdie, N.; Eyring, E. M., Piezoelectric Detection of Photoacoustic Signals, *Applied Optics,* **1978,** *17*, 1093-1098.

[213] Sam, C. L.; Shand, M. L., Photoacoustic Spectroscopy of Solids Immersed in Transparent Liquids, *Optics Communications,* **1979,** *31*, 174-177.

[214] Zhao, Z. M. Pulsed Photoacoustic Techniques and Glucose Determinnation in Human Blood and Tissue. University of Oulu, 2002.

[215] Sullivan, B.; Tam, A., Profile of Laser-produced Acoustic Pulse in a Liquid, *Journal of the Acoustical Society of America,* **1984,** *75*, 437.

[216] Kuo, C.; Vieira, M.; Patel, C., Transient Optoacoustic Pulse Generation and Detection, *Journal of Applied Physics,* **1984,** *55*, 3333.

[217] Monchalin, J.-P., Optical Detection of Ultrasound, *IEEE Transaction on Ultrasonics, Ferroelectrics and Frequency Control,* **1986,** *33*, 485-499.

[218] Paltauf, G.; Schmidt-Kloiber, H.; Guss, H., Optical Detection of Laser-induced Stress Waves for Measurement of the Light Distribution in Living Tissue, *Proceedings of SPIE,* **1996**, 127-135.

[219] Paltauf, G., Measurement of Laser-induced Acoustic Waves with a Calibrated Optical Transducer, *Journal of Applied Physics,* **1997,** *82*, 1525.

[220] Guzatov, D. V.; Oraevsky, A. A.; Oraevsky, A. N., Plasmon Resonance in Ellipsoidal Nanoparticles with Shells, *Quantum Electronics,* **2003,** *33*, 817.

[221] Oldenburg, S. J.; Averitt, R. D.; Westcott, S. L.; Halas, N. J., Nanoengineering of Optical Resonances, *Chemical Physics Letters,* **1998,** *288*, 243-247.

[222] Zharov, V. P.; Galitovsky, V.; Viegas, M., Photothermal Detection of Local Thermal Effects during Selective Nanophotothermolysis, *Applied Physics Letters,* **2003,** *83*, 4897-4899.

[223] Portney, N.; Ozkan, M., Nano-oncology: Drug Delivery, Imaging, and Sensing, *Analytical and Bioanalytical Chemistry,* **2006,** *384*, 620-630.

[224] Schmid, T., Photoacoustic Spectroscopy for Process Analysis, *Analytical and Bioanalytical Chemistry,* **2006,** *384*, 1071-1086.

[225] Egerev, S.; Ermilov, S.; Ovchinnikov, O.; Fokin, A.; Guzatov, D.; Klimov, V.; Kanavin, A.; Oraevsky, A., Acoustic Signals Generated by Laser-irradiated Metal Nanoparticles, *Applied Optics,* **2009,** *48*, C38-C45.

[226] Karabutov, A. A.; Savateeva, E. V.; Oraevsky, A. A., Optoacoustic Supercontrast for Early Cancer Detection, *Proceedings of SPIE,* **2001,** *4256*, 179-187.

[227] Anderson, R.; Parrish, J., Selective Photothermolysis: Precise Microsurgery by Selective Absorption of Pulsed Radiation, *Science,* **1983,** *220*, 524-527.

[228] Sun, J. M.; Gerstman, B. S.; Li, B., Bubble Dynamics and Shock Waves

Generated by Laser Absorption of a Photoacoustic Sphere, *Journal of Applied Physics,* **2000,** *88*, 2352-2362.

[229] Pustovalov, V. K., Thermal Processes under the Action of Laser Radiation Pulse on Absorbing Granules in Heterogeneous Biotissues, *International Journal of Heat and Mass Transfer,* **1993,** *36*, 391-399.

[230] Till, S.; Milsom, P.; Rowlands, G., A Simplified Physical Model of Pressure Wave Dynamics and Acoustic Wave Generation Induced by Laser Absorption in the Retina, *Bulletin of Mathematical Biology,* **2004,** *66*, 791-808.

[231] Leighton, T. G.; Leighton, *The Acoustic Bubble*. Academic Press Inc: San Diego, 1994.

[232] Haisch, C.; Liermann, J.; Panne, U.; Niessner, R., Characterization of Colloidal Particles by Laser-induced Plasma Spectroscopy (LIPS), *Analytica Chimica Acta,* **1997,** *346*, 23-35.

[233] Scherbaum, F. J.; Knopp, R.; Kim, J. I., Counting of Particles in Aqueous Solutions by Laser-induced Photoacoustic Breakdown Detection, *Applied Physics B: Lasers and Optics,* **1996,** *63*, 299-306.

[234] Karpiouk, A. B.; Aglyamov, S. R.; Bourgeois, F.; Ben-Yakar, A.; Emelianov, S. Y., Quantitative Ultrasound Method to Detect and Monitor Laser-induced Cavitation Bubbles, *Journal of Biomedical Optics,* **2008,** *13*, 034011-13.

[235] Rayleigh, L., VIII. On the Pressure Developed in a Liquid during the Collapse of a Spherical Cavity, *Philosophical Magazine,* **1917,** *34*, 94-98.

[236] Brennen, C., Cavitation and Bubble Dynamics (Oxford Engineering Science Series). Mcgraw Hill Book Co.: New York, 1995.

[237] Vokurka, K., On Rayleigh's Model of a Freely Oscillating Bubble. I. Basic Relations, *Czechoslovak Journal of Physics,* **1985,** *35*, 28-40.

[238] Kotaidis, V.; Plech, A., Cavitation Dynamics on the Nanoscale, *Applied Physics Letters,* **2005,** *87*, 213102-3.

[239] Brown, K. R.; Lyon, L. A.; Fox, A. P.; Reiss, B. D.; Natan, M. J., Hydroxylamine Seeding of Colloidal Au Nanoparticles. 3. Controlled Formation of Conductive Au Films, *Chemistry of Materials,* **1999,** *12*, 314-323.

[240] Liu, X.; Huan, S.; Bu, Y.; Shen, G.; Yu, R., Liposome-mediated Enhancement of

the Sensitivity in Immunoassay Based on Surface-enhanced Raman Scattering at Gold Nanosphere Array Substrate, *Talanta,* **2008,** *75*, 797-803.

[241] Akinori Takami; Yamada, H.; Nakano, K.; Koda, S., Size Reduction of Silver Particles in Aqueous Solution by Laser Irradiation, *Japanese Journal of Applied Physics,* **1996,** *35*, L781-L783.

[242] Kurita, H.; Takami, A.; Koda, S., Size Reduction of Gold Particles in Aqueous Solution by Pulsed Laser Irradiation, *Applied Physics Letters,* **1998,** *72*, 789-791.

[243] McGrath, T. E.; Beveridge, A. C.; Diebold, G. J., Laser-Induced "Regeneration" of Colloidal Particles: The Effects of Thermal Inertia on the Chemical Reactivity of Laser-Heated Particles, *Angewandte Chemie International Edition,* **1999,** *38*, 3353-3356.

[244] Feng, D.; van Deventer, J. S. J., The Role of Heavy Metal Ions in Gold Dissolution in the Ammoniacal Thiosulphate System, *Hydrometallurgy,* **2002,** *64*, 231-246.

[245] Grosse, A. C.; Dicinoski, G. W.; Shaw, M. J.; Haddad, P. R., Leaching and Recovery of Gold Using Ammoniacal Thiosulfate Leach Liquors (a review), *Hydrometallurgy,* **2003,** *69*, 1-21.

[246] Needleman, H., Lead Poisoning, *Annual Review of Medicine,* **2004,** *55*, 209-222.

[247] *http://www.epa.gov/safewater/contaminants/index.html (accessed February 2010).*

[248] Anderson, J. L.; Bowden, E. F.; Pickup, P. G., Dynamic Electrochemistry: Methodology and Application, *Analytical Chemistry,* **1996,** *68*, 379-444.

[249] Burlingame, A. L.; Boyd, R. K.; Gaskell, S. J., Mass Spectrometry, *Analytical Chemistry,* **1996,** *68*, 599-652.

[250] Kavallieratos, K.; Rosenberg, J. M.; Chen, W. Z.; Ren, Tong, Fluorescent Sensing and Selective Pb(II) Extraction by a Dansylamide Ion-Exchanger, *Journal of the American Chemical Society,* **2005,** *127*, 6514-6515.

[251] Brown, A. K.; Li, J.; Pavot, C. M. B.; Lu, Y., A Lead-Dependent DNAzyme with a Two-Step Mechanism, *Biochemistry,* **2003,** *42*, 7152-7161.

[252] Liu, C.-W.; Huang, C.-C.; Chang, H.-T., Highly Selective DNA-Based Sensor for Lead(II) and Mercury(II) Ions, *Analytical Chemistry,* **2009,** *81*, 2383-2387.

[253] Geary, C. D.; Zudans, I.; Goponenko, A. V.; Asher, S. A.; Weber, S. G., Electrochemical Investigation of Pb^{2+} Binding and Transport through a Polymerized Crystalline Colloidal Array Hydrogel Containing Benzo-18-crown-6, *Analytical Chemistry,* **2004,** *77*, 185-192.

[254] Lin, T.-J.; Chung, M.-F., Using Monoclonal Antibody to Determine Lead Ions with a Localized Surface Plasmon Resonance Fiber-optic Biosensor, *Sensors,* **2008,** *8*, 582-593.

[255] Wang, Z.; Lee, J. H.; Lu, Y., Label-Free Colorimetric Detection of Lead Ions with a Nanomolar Detection Limit and Tunable Dynamic Range by using Gold Nanoparticles and DNAzyme, *Advanced Materials,* **2008,** *20*, 3263-3267.

[256] Chen, Y.-Y.; Chang, H.-T.; Shiang, Y.-C.; Hung, Y.-L.; Chiang, C.-K.; Huang, C.-C., Colorimetric Assay for Lead Ions Based on the Leaching of Gold Nanoparticles, *Analytical Chemistry,* **2009,** *81*, 9433-9439.

[257] Gonzalez, M. G.; Liu, X.; Niessner, R.; Haisch, C., Strong Size-dependent Photoacoustic Effect on Gold Nanoparticles by Laser-induced Nanobubbles, *Applied Physics Letters,* **2010,** *96*, 174104.

[258] Schmid, T.; Panne, U.; Niessner, R.; Haisch, C., Optical Absorbance Measurements of Opaque Liquids by Pulsed Laser Photoacoustic Spectroscopy, *Analytical Chemistry,* **2009,** *81*, 2403-2409.

[259] González, M. G.; Liu, X.; Niessner, R.; Haisch, C., Lead Ion Detection in Turbid Media by Pulsed Photoacoustic Spectrometry Based on Dissolution of Gold Nanoparticles, *Sensors and Actuators B: Chemical,* **2010,** *150*, 770-773.

[260] Wu, Q.; Cao, H.; Luan, Q.; Zhang, J.; Wang, Z.; Warner, J. H.; A. R. Watt, A., Biomolecule-Assisted Synthesis of Water-Soluble Silver Nanoparticles and Their Biomedical Applications, *Inorganic Chemistry,* **2008,** *47*, 5882-5888.

[261] Wang, Y.; Yang, F.; Yang, X., Colorimetric Detection of Mercury(II) Ion Using Unmodified Silver Nanoparticles and Mercury-Specific Oligonucleotides, *ACS Applied Materials & Interfaces,* **2010,** *2*, 339-342.

[262] Kim, Y.-R.; Mahajan, R. K.; Kim, J. S.; Kim, H., Highly Sensitive Gold Nanoparticle-Based Colorimetric Sensing of Mercury(II) through Simple Ligand Exchange Reaction in Aqueous Media, *ACS Applied Materials & Interfaces,* **2009,** *2*, 292-295.

[263] Chai, F.; Wang, C.; Wang, T.; Li, L.; Su, Z., Colorimetric Detection of Pb^{2+} Using

Glutathione Functionalized Gold Nanoparticles, *ACS Applied Materials & Interfaces,* **2010,** *2*, 1466-1470.

[264] Kneipp, K.; Kneipp, H.; Itzkan, I.; Dasari, R. R.; Feld, M. S., Ultrasensitive Chemical Analysis by Raman Spectroscopy, *Chemical Reviews,* **1999,** *99*, 2957-2976.

[265] Moskovits, M., Surface-Enhanced Spectroscopy, *Reviews of Modern Physics,* **1985,** *57*, 783.

[266] Nie, S.; Emory, S. R., Probing Single Molecules and Single Nanoparticles by Surface-Enhanced Raman Scattering, *Science,* **1997,** *275*, 1102-1106.

[267] Camden, J. P.; Dieringer, J. A.; Wang, Y.; Masiello, D. J.; Marks, L. D.; Schatz, G. C.; Van Duyne, R. P., Probing the Structure of Single-Molecule Surface-Enhanced Raman Scattering Hot Spots, *Journal of the American Chemical Society,* **2008,** *130*, 12616-12617.

[268] Dieringer, J. A.; Lettan, R. B.; Scheidt, K. A.; Van Duyne, R. P., A Frequency Domain Existence Proof of Single-Molecule Surface-Enhanced Raman Spectroscopy, *Journal of the American Chemical Society,* **2007,** *129*, 16249-16256.

[269] Bell, S. E. J.; Sirimuthu, N. M. S., Surface-Enhanced Raman Spectroscopy (SERS) for Sub-Micromolar Detection of DNA/RNA Mononucleotides, *Journal of the American Chemical Society,* **2006,** *128*, 15580-15581.

[270] Tiwari, V. S.; Oleg, T.; Darbha, G. K.; Hardy, W.; Singh, J. P.; Ray, P. C., Non-resonance SERS Effects of Silver Colloids with Different Shapes, *Chemical Physics Letters,* **2007,** *446*, 77-82.

[271] Hutchison, J. A.; Centeno, S. P.; Odaka, H.; Fukumura, H.; Hofkens, J.; Uji-i, H., Subdiffraction Limited, Remote Excitation of Surface Enhanced Raman Scattering, *Nano Letters,* **2009,** *9*, 995-1001.

[272] Denissenko, M. F.; Pao, A.; Tang, M.-s.; Pfeifer, G. P., Preferential Formation of Benzo[a]pyrene Adducts at Lung Cancer Mutational Hotspots in P53, *Science,* **1996,** *274*, 430-432.

[273] Le Marchand, L.; Hankin, J. H.; Pierce, L. M.; Sinha, R.; Nerurkar, P. V.; Franke, A. A.; Wilkens, L. R.; Kolonel, L. N.; Donlon, T.; Seifried, A.; Custer, L. J.; Lum-Jones, A.; Chang, W., Well-done Red Meat, Metabolic Phenotypes and Colorectal Cancer in Hawaii, *Mutation Research/Fundamental and Molecular Mechanisms of Mutagenesis,* **2002,** *506-507*, 205-214.

[274] Volk, D. E.; Thiviyanathan, V.; Rice, J. S.; Luxon, B. A.; Shah, J. H.; Yagi, H.; Sayer, J. M.; Yeh, H. J. C.; Jerina, D. M.; Gorenstein, D. G., Solution Structure of a Cis-Opened (10*R*)-N^6-Deoxyadenosine Adduct of (9*S*,10*R*)-9,10-Epoxy-7,8,9,10-tetrahydrobenzo[*a*]pyrene in a DNA Duplex, *Biochemistry,* **2003,** *42*, 1410-1420.

[275] Mrozek, I.; Otto, A., SERS-A Long-range Effect ?, *Applied Physics A: Materials Science & Processing,* **1989,** *49*, 389-391.

[276] Shalaev, V. M., *Optical Nonlinearities of Fractal Composites: Optical Properties of Nanostructured Random Media*. Springer-Verlag: Berlin/Heidelberg, 2002; p 93-112, 218.

[277] Markel, V. A.; Shalaev, V. M.; Zhang, P.; Huynh, W.; Tay, L.; Haslett, T. L.; Moskovits, M., Near-field Optical Spectroscopy of Individual Surface-plasmon Modes in Colloid Clusters, *Physical Review B,* **1999,** *59*, 10903.

[278] Moskovits, M.; Jeong, D. H., Engineering Nanostructures for Giant Optical Fields, *Chemical Physics Letters,* **2004,** *397*, 91-95.

[279] Le Ru, E. C.; Meyer, M.; Etchegoin, P. G., Proof of Single-Molecule Sensitivity in Surface Enhanced Raman Scattering (SERS) by Means of a Two-Analyte Technique, *The Journal of Physical Chemistry B,* **2006,** *110*, 1944-1948.

[280] Doering, W. E.; Nie, S., Spectroscopic Tags Using Dye-Embedded Nanoparticles and Surface-Enhanced Raman Scattering, *Analytical Chemistry,* **2003,** *75*, 6171-6176.

[281] Mulvaney, S. P.; Musick, M. D.; Keating, C. D.; Natan, M. J., Glass-Coated, Analyte-Tagged Nanoparticles: A New Tagging System Based on Detection with Surface-Enhanced Raman Scattering, *Langmuir,* **2003,** *19*, 4784-4790.

[282] Lu, Y.; Yin, Y.; Li, Z.-Y.; Xia, Y., Synthesis and Self-Assembly of Au@SiO2 Core−Shell Colloids, *Nano Letters,* **2002,** *2*, 785-788.

[283] Liz-Marzán, L. M.; Giersig, M.; Mulvaney, P., Synthesis of Nanosized Gold−Silica Core−Shell Particles, *Langmuir,* **1996,** *12*, 4329-4335.

[284] Yin, Y.; Lu, Y.; Sun, Y.; Xia, Y., Silver Nanowires Can Be Directly Coated with Amorphous Silica To Generate Well-Controlled Coaxial Nanocables of Silver/Silica, *Nano Letters,* **2002,** *2*, 427-430.

[285] Schatz, G. C., Theoretical Studies of Surface Enhanced Raman Scattering, *Accounts of Chemical Research,* **1984,** *17*, 370-376.

[286] Otto, A.; Mrozek, I.; Grabhorn, H.; Akemann, W., Surface-Enhanced Raman Scattering, *Journal of Physics: Condensed Matter,* **1992,** *4*, 1143.

[287] Gong, J.-L.; Jiang, J.-H.; Yang, H.-F.; Shen, G.-L.; Yu, R.-Q.; Ozaki, Y., Novel Dye-embedded Core-shell Nanoparticles as Surface-Enhanced Raman Scattering Tags for Immunoassay, *Analytica Chimica Acta,* **2006,** *564*, 151-157.

[288] Sharaabi, Y.; Shegai, T.; Haran, G., Two-state Analysis of Single-molecule Raman Spectra of Crystal Violet, *Chemical Physics,* **2005,** *318*, 44-49.

[289] Schmid, T.; Helmbrecht, C.; Haisch, C.; Panne, U.; Niessner, R., On-line Monitoring of Opaque Liquids by Photoacoustic Spectroscopy, *Analytical and Bioanalytical Chemistry,* **2003,** *375*, 1130-1135.

[290] Mucic, R. C.; Storhoff, J. J.; Mirkin, C. A.; Letsinger, R. L., DNA-Directed Synthesis of Binary Nanoparticle Network Materials, *Journal of the American Chemical Society,* **1998,** *120*, 12674-12675.

[291] Leopold, N.; Lendl, B., A New Method for Fast Preparation of Highly Surface-Enhanced Raman Scattering (SERS) Active Silver Colloids at Room Temperature by Reduction of Silver Nitrate with Hydroxylamine Hydrochloride, *The Journal of Physical Chemistry B,* **2003,** *107*, 5723-5727.

[292] Wolter, A.; Niessner, R.; Seidel, M., Preparation and Characterization of Functional Poly(ethylene glycol) Surfaces for the Use of Antibody Microarrays, *Analytical Chemistry,* **2007,** *79*, 4529-4537.

[293] Link, S.; Wang, Z. L.; El-Sayed, M. A., Alloy Formation of Gold−Silver Nanoparticles and the Dependence of the Plasmon Absorption on Their Composition, *The Journal of Physical Chemistry B,* **1999,** *103*, 3529-3533.

[294] Johnson, P. B.; Christy, R. W., Optical Constants of the Noble Metals, *Physical Review B,* **1972,** *6*, 4370.